Muon spin spectroscopy and high magnetic field studies of novel superconductors and magnetic materials

Francesca R. Foronda
Brasenose College, University of Oxford

A thesis submitted for the Degree of
Doctor of Philosophy in Condensed Matter Physics

Trinity Term 2016

Abstract

Muon spin spectroscopy and high magnetic field studies of novel superconductors and magnetic materials

Francesca R. Foronda
Brasenose College, University of Oxford
Trinity Term 2016

A thesis submitted for the Degree of Doctor of Philosophy

This thesis investigates a number of novel magnetic materials and high temperature superconductors using high-field magnetometry and muon spin spectroscopy (μSR). The main measurement techniques are briefly described and a study of the dimer material [Cu(pyrazine)(glycine)]ClO_4 is presented to demonstrate the use of the proximity detector oscillator as a susceptometer in high magnetic fields.

μSR is a highly effective tool for probing magnetic order, spin freezing and spin dynamics. However, in some circumstances its performance may be impaired by the extent to which it perturbs the material under study. Using μSR, density functional theory and crystal field calculations, I identify an experimental situation in the family of candidate quantum spin ices $Pr_2B_2O_7$ (B = Sn, Zr, and Hf), in which the measured response is dominated by a muon-induced distortion of the local structure. This issue is also addressed in a study of the spin dynamics in the canonical spin ice $Ho_2Ti_2O_7$. Although computational work indicates a similar muon-induced effect in both $Ho_2Ti_2O_7$ and $Dy_2Ti_2O_7$, the μSR data is not dominated by this perturbation.

The remainder of this thesis is concerned with studying the superconducting properties of a number of Fe-based materials, including LiFeP which is found to have an enhanced superfluid stiffness in relation to its transition temperature. Also reported is the effect of structural disorder on the superconducting state in recently discovered $Sr_{0.3}(NH_2)_y(NH_3)_{1-y}Fe_2Se_2$. Pulsed magnetic field measurements are used to probe the temperature dependence of the upper critical field, giving a maximum value of $\mu_0 H_{c2}(0) \approx 33(2)$ T. I also investigate the effect of intercalating additional ammonia, via reversible adsorption and desorption in the related superconductor $Li_x[(NH_2)_y(NH_3)_{1-y}]_zFe_2Se_2$ ($z = 1, 2$). These reactions were carried out *in situ* on the muon beamline so that the superfluid stiffness could be measured using transverse-field μSR on a single sample.

Acknowledgements

I am indebted to my supervisors Stephen Blundell and Paul Goddard for their advice, encouragement and invaluable support throughout my time at Oxford. The work presented in this thesis has benefited greatly from a number of collaborations and in particular, I would like to thank Tom Lancaster, Andrew Boothroyd, Francis Pratt and Peter Baker for their guidance and contributions. These experiments would not have been possible without the high quality samples provided by Simon Clarke and his group, as well as Jamie Manson and Prabhakaran. I would also like to thank Saman Ghannadzadeh, Johannes Möller, Junjie Liu, Jack Wright, Franz Lang and all other members of the Quantum Matter group. I gratefully acknowledge the funding provided by Brasenose College and the IOP which has allowed me to attend two international conferences, and EPSRC for the provision of a studentship. Finally, my heartfelt thanks goes to Andy for his unfailing support and patience, and my parents for their constant encouragement throughout my time at university.

For my parents

List of publications

1. *Upper critical field of $NaFe_{1-x}Co_xAs$ superconductors* S. Ghannadzadeh, J. D. Wright, F. R. Foronda, S. J. Blundell, S. J. Clarke, and P. A. Goddard, Phys. Rev. B **89**, 054502, (2014)

2. *Local magnetism and spin correlations in the geometrically frustrated cluster magnet $LiZn_2Mo_3O_8$* J. P. Sheckelton, F. R. Foronda, LiDong Pan, C. Moir, R. D. McDonald, T. Lancaster, P. J. Baker, N. P. Armitage, T. Imai, S. J. Blundell, and T. M. McQueen, Phys. Rev. B **89**, 064407, (2014)

3. *Controlling Magnetic Order and Quantum Disorder in Molecule-Based Magnets* T. Lancaster, P. A. Goddard, S. J. Blundell, F. R. Foronda, S. Ghannadzadeh, J. S. Möller, P. J. Baker, F. L. Pratt, C. Baines, L. Huang, J. Wosnitza, R. D. McDonald, K. A. Modic, J. Singleton, C. V. Topping, T. A. W. Beale, F. Xiao, J. A. Schlueter, A. M. Barton, R. D. Cabrera, K. E. Carreiro, H. E. Tran, and J. L. Manson, Phys. Rev. Lett. **112**, 207201, (2014)

4. *Strontium Vanadium Oxide-Hydrides: "Square-Planar" Two-Electron Phases* F. D. Romero, A. Leach, J. S. Möller, F. R. Foronda, S. J. Blundell and M. A. Hayward, Angew. Chem.-Int. Ed. **53**, 7556, (2014)

5. *Anisotropic local modification of crystal field levels in Pr-based pyrochlores: a muon-induced effect modeled using density functional theory* F. R. Foronda, F. Lang, J. S. Möller, T. Lancaster, A. T. Boothroyd, F. L. Pratt, S. R. Giblin, D. Prabhakaran and S. J. Blundell, Phys. Rev. Lett. **114**, 017602, (2015)

6. *Soft Chemical Control of Superconductivity in Lithium Iron Selenide Hydroxides $Li_{1-x}Fe_x(OH)Fe_{1-y}Se$* H. Sun, D. N. Woodruff, S. J. Cassidy, G. M. Allcroft, S. J. Sedlmaier, A. L. Thompson, P. A. Bingham, S. D. Forder, S. Cartenet, N. Mary, S. Ramos, F. R. Foronda, B. H. Williams, X. Li, S. J. Blundell, and S. J. Clarke, Inorg. Chem. **54**, 1958, (2015)

7. *Robustness of superconductivity to structural disorder in $Sr_{0.3}(NH_2)_y(NH_3)_{1-y}$-$Fe_2Se_2$* F. R. Foronda, S. Ghannadzadeh, S. J. Sedlmaier, J. D. Wright, K. Burns, S. J. Cassidy, P. A. Goddard, T. Lancaster, S. J. Clarke, and S. J. Blundell, Phys. Rev. B **92**, 134517, (2015)

8. Antiferromagnetism in a Family of S=1 Square Lattice Coordination Polymers $NiX_2(pyz)_2$ (X = Cl, Br, I, NCS; pyz=Pyrazine) J. Liu, P. A. Goddard, J. Singleton, J. Brambleby, F. Foronda, J. S. Möller, Y. Kohama, S. Ghannadzadeh, A. Ardavan, S. J. Blundell, T. Lancaster, F. Xiao, R. C. Williams, F. L. Pratt, P. J. Baker, K. Wierschem, S. H. Lapidus, K. H. Stone, P. W. Stephens, J. Bendix, T. J. Woods, K. E. Carreiro, H. E. Tran, C. J. Villa and J. L. Manson, Inorg. Chem. **55**, 3515, (2016)

9. *Polarization memory in the nonpolar magnetic ground state of multiferroic* $CuFeO_2$ J. Beilsten-Edmands, S. J. Magorrian, F. R. Foronda, D. Prabhakaran, P. G. Radaelli, and R. D. Johnson, Phys. Rev. B, *awaiting publication*

10. *In situ muon-spin rotation study of superconductivity in ammonia-poor and ammonia-rich intercalated* $Li_x(NH_2)_y(NH_3)_{1-y}Fe_2Se_2$ $(z = 1, 2)$ F. R. Foronda, D. N. Woodruff, S. J. Cassidy, F. L. Pratt, P. J. Baker, T. Lancaster, S. J. Clarke, and S. J. Blundell, Phys. Rev. B, *submitted*

Table of Contents

Chapter 1

Introduction

There is much current interest in novel materials that show unusual magnetic ground states which cannot be described by semi-classical models. Exotic behaviour may result, for example, from complex crystal structures, magnetic frustration, or a close proximity to a superconducting ground state. Recent developments have included the discovery of frustrated materials that realise the spin ice ground state [1, 2], as well as new Fe-based compounds that exhibit high-T_c superconductivity [3].

This thesis is concerned with studying these new compounds using state-of-the-art techniques that extract magnetic information. One powerful technique is muon spin spectroscopy (μSR), which is especially suited for studying weak magnetic moments and slow dynamics. In these measurements, spin-polarised muons are implanted into the sample and used as a local probe of internal fields. Example applications include measuring an order parameter as a function of temperature, studying magnetic fluctuations, and mapping internal magnetic field distributions for the study of vortex lattice properties. Pulsed field systems are another effective tool as the ultra high magnetic fields that they produce can be used to push materials through their field-temperature phase diagrams and allow an estimate of exchange interactions in magnetic samples and critical fields in superconductors. Combining these techniques

with SQUID magnetometry allows a consistent picture of the underlying physics which gives rise to these new and exciting phenomena. In certain circumstances, it is also important to assess whether the probe in operation is disturbing the system under study and this issue will form the basis of another key result of this thesis. This will be addressed in chapter 3 in which I will demonstrate how a muon-induced perturbation can occur in a particular family of quantum spin ices.

Thesis outline

Chapter 2: Experimental techniques The techniques of muon spin spectroscopy, pulsed-field magnetometry and low-field susceptibility measurements are introduced. A study of the dimer material $[Cu(pyz)(gly)]ClO_4$ is used to demonstrate the application of the proximity detector dynamic oscillator in high magnetic fields.

Chapter 3: Pr-based pyrochlore oxides μSR is employed to investigate a family of candidate quantum spin ices. Using density-functional theory and crystal field calculations, it is shown how the observed behaviour results from a highly anisotropic distortion field induced by the implanted muon.

Chapter 4: Muon states in classical spin ice Spin dynamics in $Ho_2Ti_2O_7$ are investigated using μSR and compared to those observed in $Dy_2Ti_2O_7$. Computational work indicates a muon-induced distortion of the crystal field levels that is similar to that found in the Pr-based pyrochlores. In this case, the muon perturbation does not appear to alter the measured response of the μSR technique.

Chapter 5: Fe-based superconductors A combination of pulsed-field magnetometry, μSR and low field susceptibility measurements are used to explore the superconducting properties of several Fe-based high-T_c superconductors. Studies discussed include the role of ammonia in Li-intercalated FeSe, and the effect of structural disorder on superconductivity in the recently discovered Sr-intercalated FeSe.

Chapter 6: Conclusion An overview of the key results obtained in this thesis.

Chapter 2

Experimental Methods

This chapter details the two main measurement techniques used in this thesis, that is: microscopic measurements in the form of muon spin rotation/relaxation (μSR), and bulk measurements in the form of pulsed-field magnetometry. The μSR experiments described here were carried out the ISIS muon facility, UK and the Swiss muon facility at the Paul Scherrer Institute, Switzerland (PSI). Pulsed field measurements were conducted in-house at the Nicholas Kurti Magnetic Field Laboratory, Oxford (NKMFL).

2.1 Muon Spin Spectroscopy

2.1.1 Basic principles

Muon spin rotation/relaxation (μSR) is a technique that utilises muons as extremely sensitive local magnetometers [4, 5]. In contrast to other techniques such as neutrons and x-rays, μSR does not involve any scattering. Instead, an ensemble of spin-polarised muons are implanted into the material where they remain until they decay. An analysis of the decay positrons allows one to measure the time-evolution of

the muon polarisation from which one can infer the spatial distribution and dynamics of the local moments. In principle, both positive and negative muons may be used, although for most condensed matter research, and for the purpose of this thesis, it is the positive muon that is of interest. This is due to the positive muon being attracted to areas of negative charge such as regions of high electron density. By contrast, the negative muon is attracted to the atomic nuclei, thus rendering it less sensitive to the physical properties of interest (namely magnetism and superconductivity).

	e	μ	p
Charge	e	e	e
Spin	1/2	1/2	1/2
Mass	m_e	207 m_e	1836 m_e
$\gamma/2\pi$(MHzT^{-1})	28025	135.5	42.58
Magnetic moment	657 μ_p	3.18 μ_p	μ_p
Lifetime	$> 4.6 \times 10^{26}$ yr	2.197 μs	$> 2.1 \times 10^{29}$ yr

Table 2.1: Properties of the electron, muon and proton, including their gyromagnetic ratios γ.

μSR offers several unique capabilities as a measurement probe owing to the properties of the muon itself (listed in Table 2.1). Firstly, its large gyromagnetic ratio enables measurements of fields down to 10^{-5} T, making it highly suitable for sensing moments on the atomic scale. This is advantageous for systems with weak or randomly ordered moments for which there is often no other measurement technique available. It can also be a complementary technique to other measurements because of its unique time-window. With a lifetime of 2.19μs, the muon is capable of measuring magnetic fluctuation rates in the range of 10^4 to 10^{12} Hz, bridging the gap between those observed by NMR and neutron scattering.

2.1.2 Muon production

μSR requires low-energy spin-polarised muons that are produced in a synchrotron or cyclotron via a two-stage pion decay. Firstly, pions are produced by high-energy proton collisions, usually with a graphite target;

$$\begin{aligned} p + p &\rightarrow \pi^+ + p + n, \\ p + n &\rightarrow \pi^+ + n + n, \\ p + p &\rightarrow \pi^- + p, \end{aligned} \tag{2.1}$$

and these pions decay into muons and muon-neutrinos;

$$\pi^+ \rightarrow \mu^+ + \nu_\mu. \tag{2.2}$$

Conservation of angular and linear momentum and parity violation ensures that the muons are spin polarised as follows: consider a pion with spin 0 decaying from rest in the target; the decay is a two-body process thus the muon and neutrino must have equal and opposite momentum/spin and, as the neutrino has negative helicity, it follows that the muon spin must also be anti-parallel to its own momentum. The muons described here are termed *surface muons*, as they are produced close to the surface of the target and typically have energies of $\approx 4\,\mathrm{MeV}$ [6]. In some cases the pions escape the target and decay in flight, producing so-called *decay muons* of higher energies and a reduced polarisation. Normally, such particles would pass straight through a typical size sample and do not contribute to the measured data. However, there are cases in which decay muons are needed to increase the muon momentum, such as in high-pressure measurements for which higher energies are required to penetrate the walls of the pressure cell and reach the bulk of the sample.

A series of steering and quadropole magnets focus the muons into a high intensity

beam which maintains 100% spin polarisation. The beam is bent in some magnetic field B around a given radius $r = p/(qB)$, where q is charge and p is momentum, such that only particles with a particular momentum (or p/q) reach the sample. Any other contaminate particles, including positrons from early muon decay, are filtered off by a *Wien velocity filter*, which utilises crossed magnetic B and electric E fields to select particles of a certain velocity. In this system, all charged particles that have a velocity $v \neq E/B$ will experience a Lorentz force and be diverted off course. With the momentum already selected, the fields may be calibrated such that their ratio $E/B = v_\mu$ selects particles of mass m_μ, thus ensuring that only muons are filtered through.

Both continuous wave and pulsed beams may be produced using the processes described above. Muons in continuous wave sources, such as that at PSI, are delivered to the sample one at a time. A clock is triggered with the arrival of a single muon and stops with its decay and detection of an emitted positron, an *event*. This technique allows for a better time resolution and detection of larger magnetic fields compared to pulsed-sources. However, the measurement window is limited by the muon lifetime as long-lived particles can lead to ambiguity if a muon arrives at a sample before its predecessor has had enough time to decay. Thus consecutive muon events that occur over a certain number of muon lifetimes must be rejected, making continuous beams unsuitable for studying slow relaxation rates [4, 5]. Pulsed sources, such as that found at the ISIS facility, use beams containing widely separated bunches of muons and each event is calculated with respect to the arrival of the pulse, allowing one to measure comparatively long-lived particles. A lower background is achieved as the detectors remain active only after the detection of a pulse thus reducing the ratio of detected background to signal events during a series of runs. Pulsed sources are limited by the finite width of the pulse which is usually on the order of 70 ns.

2.1.3 Muon interactions and decay

In the first 0.1–1 ns following implantation the muons will partake in ionisation events with host atoms and scattering with electrons until the energies are reduced to a few keV. Crucially, these processes are Coulombic in nature so the polarisation of the particles remain virtually intact. An implanted muon may also produce vacancies in the lattice during thermalisation. However, as this can only occur above a threshold energy only a small fraction of the initial muon trajectory is affected and the muon will typically propagate another $\sim 1\,\mu$m to settle in interstitial sites of high electron densities and remain well separated from any induced defects [4, 6]. In one scenario, a muon and electron may enter a bound hydrogen-like final state called *muonium*, which will eventually lose all of its energy through inelastic collisions with the host atoms.

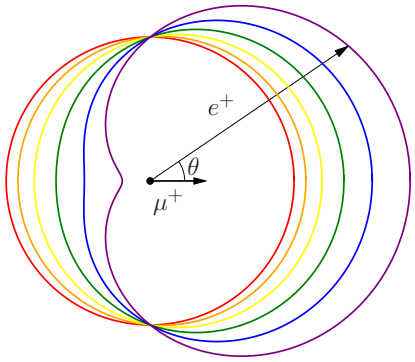

Figure 2.1: Angular distribution of emitted positrons from muon decay (shown for different positron energies). The black horizontal arrow denotes the direction of the muon spin. Larger energies result in a more anisotropic distribution.

The muon will decay into a positron, electron-neutrino and muon anti-neutrino

$$\mu^+ \rightarrow e^+ + \nu_e + \overline{\nu}_\mu. \tag{2.3}$$

Like pion decay, this process involves the weak interaction and therefore parity vio-

lation which results in the positrons being emitted preferentially along the direction of the muon spin. The angular distribution of emitted positrons with respect to the muon spin at time of decay is given by

$$N(\theta) = N_0(1 + \beta \cos\theta), \tag{2.4}$$

where $\beta = 1$ for the maximum possible positron energy (52.8 MeV) and $\beta = 1/3$ when averaged over all possible energies [7]. Thus, by observing a substantially large number of decay events, the time-dependence of the spin-polarisation of an ensemble of muons may be deduced.

2.1.4 Muon precession and relaxation

The quantity of interest in a μSR experiment is the time-dependent muon polarisation. Consider a muon initially polarised along the z-axis in a magnetic field B . Its spin will precess around B with Larmor frequency $\omega = \gamma_\mu B$, where $\gamma_\mu = 2\pi \times 135.5\,\mathrm{MHz\,T^{-1}}$ is the muon gyromagnetic ratio. Note how ω depends on the magnitude of B, and not its direction with respect to the muon polarization which only affects the amplitude of the frequencies. This makes μSR a powerful technique for both single and polycrystalline samples. The time evolution of its z-component of polarization $P_z(t)$ is then given by

$$P_z(t) = \cos^2\theta + \sin^2\theta \cos\omega t, \tag{2.5}$$

where θ is the angle between B and the z-axis (see Fig.2.2). Taking the powder average yields

$$P_z(t) = \frac{1}{3} + \frac{2}{3}\cos(\gamma_\mu B t), \tag{2.6}$$

where the 1/3 denotes the fraction of spins that are parallel to the initial muon polarisation and therefore do not precess (this is the origin of the '1/3-tail' often

observed in ordered polycrystalline samples).

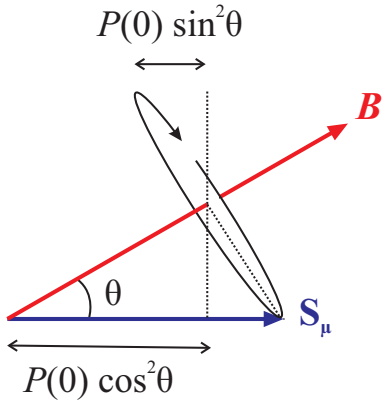

Figure 2.2: Larmor precession of muon polarisation around a local field B.

An arrangement of scintillation detectors are placed around the sample space to track the direction of emitted positrons. There are two possible geometrical configurations for these detectors; longitudinal and transverse, as shown in Fig. 2.3. The former is used for zero-field (ZF) and longitudinal-field (LF) measurements (muon spin relaxation) whilst the latter is used for transverse-field (TF, or muon spin rotation). A more detailed discussion of these types of measurements and their applications will be addressed in the following sections, although for the purpose of this discussion one needs only to consider the LF arrangement. This involves placing one bank of detectors behind the sample (the forward detector) and the other to intersect the muon beam in between the sample and the entry window (the backward detector). The polarisation is measured directly by observing the relative counts of the forward and backward detectors via the time-dependent asymmetry function

$$A(t) = \frac{N_{\mathrm{B}}(t) - \alpha N_{\mathrm{F}}(t)}{N_{\mathrm{B}}(t) + \alpha N_{\mathrm{F}}(t)}, \tag{2.7}$$

where N_{B} and N_{F} denote the number of counts in the forward and backward detectors, respectively. The constant α is experimentally determined to account for any difference in detector efficiency. Note how without the normalising denominator, $A(t)$

would reflect the radioactive nature of the muons as an exponential decay curve. It is the asymmetry spectrum that carries information on the internal field distribution. Oscillations in that spectrum will dephase with any spatial or time-dependent variations in the local field, which is observed as a relaxation of the ensemble spin polarisation. In a μSR experiment, one interprets the data by fitting the asymmetry to a proposed model for the internal field distribution of the sample using a least-squares fitting routine. For this project this was done using the WIMDA (Windows Muon Data Analysis) package [8]. There are many different functions that are used to describe a wide range of physical scenarios that may be studied with μSR, each with their own approximations. The following sections will discuss some of the cases relevant to the research presented in this thesis.

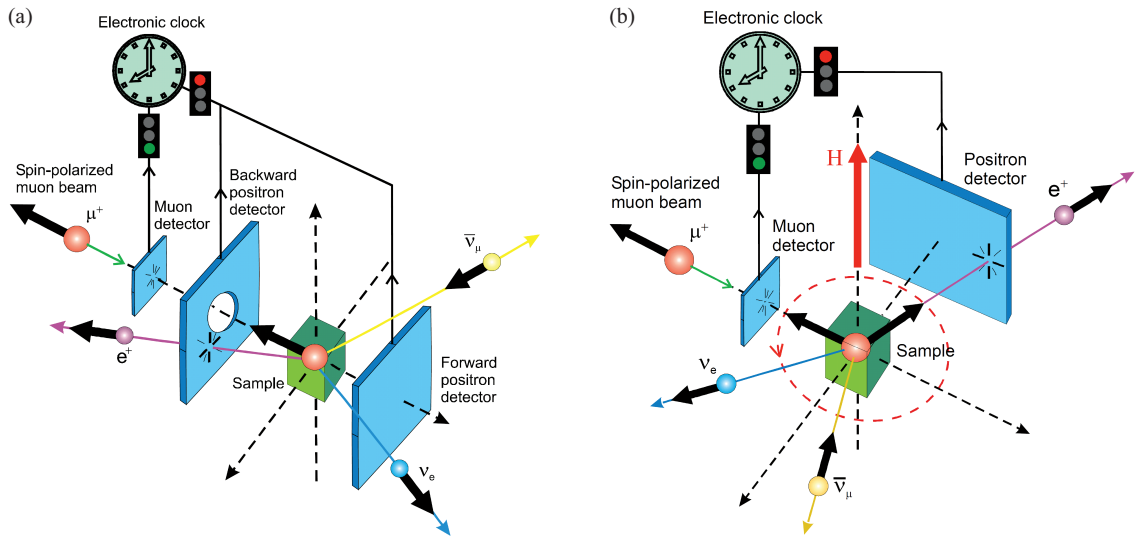

Figure 2.3: Experimental setup in a (a) ZF/ LF geometry and (b) TF configuration (modified from [9]).

2.1.5 Zero-field and longitudinal μSR

Weak internal magnetism may be be studied using ZF μSR. This is the simplest setup in which the local B originates from intrinsic magnetic (or nuclear) moments near

the muon site. If long-range magnetic order is present, a significant number of muons will stop in sites of equivalent local fields and this results in a coherent precession of muon spins which manifests as a cosinusoidal asymmetry function. Typically, the maximum value of $A(t)$ is $\sim 25\%$ which results from the intrinsic asymmetry of the muon decay and the finite solid angle subtended by the detectors.

If the local field has an inhomogeneous distribution and thus varies from site to site, the signal is damped (relaxed) as muons oscillating at different frequencies dephase over time. In the ordered case, there may be a slight variation in field at each muon site which will result in weakly damped oscillations. Another common example is one that arises from nuclear moments, in which the variation between muon sites is so large that no oscillations are observed. Instead, the asymmetry may be described using a Gaussian Kubo-Toyabe relaxation function $G_{\mathrm{KB}}(\Delta, t)$ [10, 11].

$$G_{\mathrm{KB}}(\Delta, t) = \frac{1}{3} + \frac{2}{3}\exp(-\Delta^2 t^2/2)(1 - \Delta^2 t^2). \tag{2.8}$$

This is observed as an initially Gaussian depolarisation which recovers to a constant long-time '1/3 tail' as shown in Fig.2.4(a) (note that is not 1/3 of the total asymmetry, as mentioned earlier, but 1/3 of its normalised value). This model is based on the central limit theorem; that is, in a statistically disordered system the magnetic field sensed by the muon at any given point would take a random value and this may be approximated by a normal distribution of width Δ/γ_μ about the mean (in this case zero). Note that this distribution is appropriate for concentrated moments. Dilute distributions are better modelled by a Lorentzian function, giving rise to the Lorentzian Kubo-Toyabe function, as first predicted by Walstedt and Walker [12].

So far, all of these examples have involved static moments. Another cause of damping is from a time-dependent field distribution that arises from either fluctuating moments or muon diffusion (muon hopping) and this manifests as an exponential time

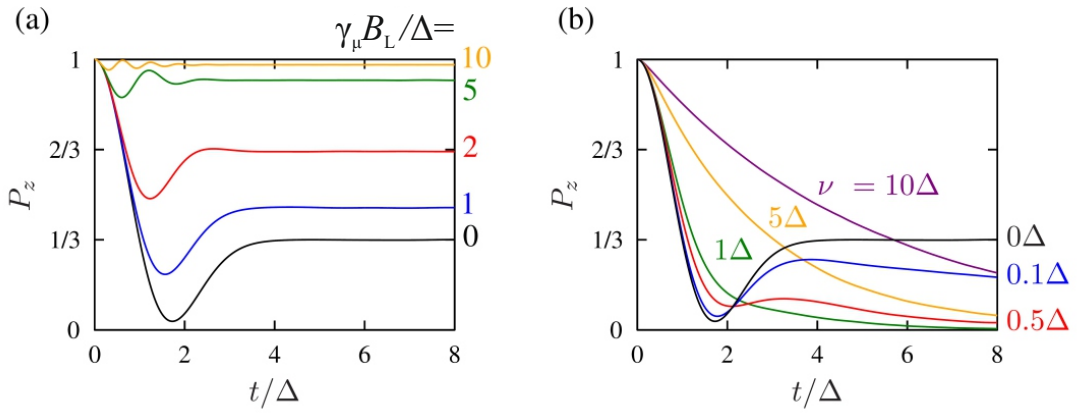

Figure 2.4: The Gaussian Kubo-Toyabe function in (a) applied longitudinal field B_L and (b) the dynamic case in ZF for a range of fluctuation rates ν. Black curves correspond to the static Zero-field Kubo-Toyabe function of Eq. 2.8. The quantities are given in units of the field width Δ. It can be seen that $\nu \gg \Delta$ results in the fast fluctuation limit for which the relaxation takes the form of an exponential decay curve (modified from [13]).

relaxation [4]. The effects of muon hopping on the measured relaxation are shown in Fig˙ 2.4(b) for a range of fluctuation (or hopping) rates ν. In the case of $\nu = 0$, the relaxation takes the form of the zero-field Kubo-Toyabe curve described by Eq. 2.8. If the dynamics are comparatively slow ($\nu < \Delta$), then this is observed as a relaxation in the 1/3 tail at late times, and the form of the tail may be approximated by

$$P_z(\nu, t) = \frac{1}{3}\exp(-\frac{2}{3}\nu t). \tag{2.9}$$

If the dynamics are fast ($\nu \gg \Delta$), the asymmetry is dominated by the exponential relaxation and, rather counter-intuitively, the relaxation rate decreases as the fluctuation or hopping rate increases. In this case, the relaxation is well represented by a simple exponential

$$P_z(t) = e^{-\lambda t}, \tag{2.10}$$

in which the relaxation rate is given by $\lambda = 2\Delta^2/\nu$.

Of course, these are simplified examples and often the spectra display a range of

both static and dynamic phenomena. One of the ways of distinguishing between these is to use LF μSR, in which a magnetic field B_{L} is applied in the initial direction of muon polarisation [4]. Initially, the muons precess in both applied and internal fields, but with increasing B_{L} the vector sum of the local and applied field becomes increasingly aligned until the muons are completely decoupled from the intrinsic moments (the applied field pins the muon spin along its initial direction). The polarisation is restored, which in the case of a Kubo-Toyabe relaxation, for example, means a recovery of the 1/3 tail to its maximum value (see Fig. 2.4a). Since static moments decouple in much lower fields, a combination of ZF and LF μSR can be used to infer the origin of the relaxation.

2.1.6 Transverse-field μSR

In TF μSR (also known as transverse-field muon spin rotation), the detectors are placed around the sample and the field is applied perpendicular to the initial muon spin. In this case, the ensemble spin rotates around the applied field B_{TF} and on implantation, any variation in the local field distribution is observed as an envelope in $A(t)$. A typical relaxation function has the form;

$$A(t) = A_0 \cos(\omega t) f(t), \tag{2.11}$$

where A_0 is the initial asymmetry, $\omega = \gamma_\mu B_{\mathrm{loc}}$ is the angular frequency of the oscillations which are dependent on the local transverse field B_{loc}, and $f(t)$ is a function describing the relaxing envelope.

One of the principal applications of TF μSR is for studying type-II superconductors. These systems form vortex lattices when cooled to their Shubnikov state in an applied field, and the magnetic field distribution inside the vortex lattice can be mapped out using μSR. Depending on the superconducting penetration depth, the lo-

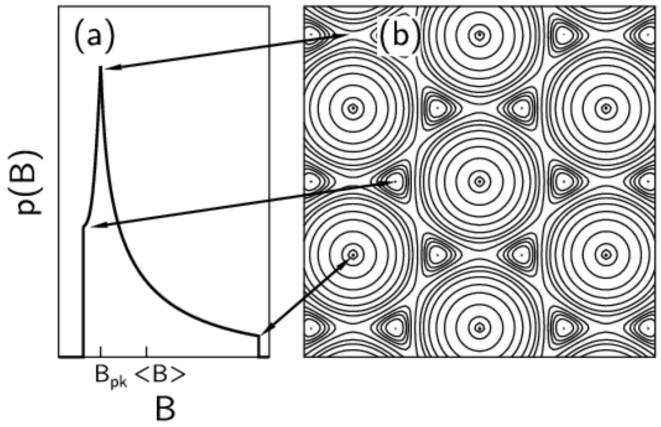

Figure 2.5: (a) The field distribution $P(B)$ with mean field $\langle B \rangle$ in an ideal type-II superconductor as measured by an ensemble of muons. The vortex lattice with contours of B is shown in (b). The arrows indicate muon sites that contribute to the extreme parts of the field distribution; the maximum and minimum fields at the vortex cores and furthest from the cores, respectively, and the most probable value $B_{\rm pk}$ at intermediate sites (figure taken from [4]).

cal field measured by each muon can range from zero in the superconducting regions to $B_{\rm TF}$ in the normal vortex cores. Muons will settle in any set of crystallographically-equivalent sites but as the vortex lattice is, in general, incommensurate with the crystal lattice and of a significantly larger scale, the full range of field distribution is sampled. It is broadened slightly by nuclear spin contributions, as well as any disorder in the vortex lattice, for example due to pinning. A typical field distribution is shown schematically in Fig. 2.5. In these instances TF μSR can be used to extract the penetration depth and its temperature dependence [4].

2.1.7 Experimental considerations: background terms

Samples are usually wrapped in silver foil packets and placed on a silver backing plate. The sample thickness and surface area are maximised to ensure that most muons will stop in its bulk, with few being captured by the backing plate. Silver is often used because it is very weakly diamagnetic, has very small nuclear moments ($\sim -0.1\mu_{\rm N}$) and does not superconduct under normal conditions, thus it does not induce any

appreciable effect on the precession or depolarisation of the muon spins. In some cases, a haematite mask (Fe_2O_3) may be used to remove an unwanted background signal as its large, randomly oriented magnetic fields ensures that any muons implanted into the material would depolarise too rapidly to contribute to measure asymmetry. Thin samples may require a 'degrader' (usually some sheets of silver foil) which is placed in front of the sample to slow down muons and ensure that they stop in bulk of the sample.

For smaller samples a 'fly-past' holder may be used to further increase the signal-to-background ratio. This consists of a pair of prongs that allow the sample to be suspended in the beam such that any muons missing the sample ideally pass straight through. In continuous muon sources, this is detected by a veto counter and any subsequent decay event is discounted. In a pulsed source, the muons pass through a hole in the backward detector bank and collected at the end of a flypast tank where the decay positrons are not detected.

To account for the small number of muons that do stop in the sample holder or walls of the cryostat, a background term, A_{bg}, is often included in the relaxation function. This adds a temperature-independent baseline to the spectra. However, the background can sometimes vary slightly over the course of an experiment, for example due to varying applied or stray fields which alter the path of incoming muons and decay positrons. In these cases, the quasi-static background may be modelled by the phenomenological term $A_{\mathrm{bg}}e^{-\lambda_{\mathrm{bg}}t}$, which is allowed to vary slightly between experimental runs. The background relaxation rate λ_{bg} is usually small ($\sim 0.01\,\mu$s) compared to that of the material of interest and therefore normally disregarded.

2.1.8 The spectrometers

The experiments presented in this thesis involved several different instruments, including the MuSR and EMU spectrometers at ISIS, and GPS, LTF, and HAL-9500 at PSI. As described earlier, a pulsed source such as ISIS provides a longer time window (around 30 μs as opposed to 10 μs at PSI) that is better suited to slower dynamics (down to 0.03 MHz compared to 0.1 MHz). However, due to a greater number of muons arriving at any given time, it is also more susceptible to the electronic deadtime that is experienced by each detector after the detection of a positron, usually lasting around 10 ns. To minimise these effects, the detectors at ISIS are highly segmented into individual banks which can be regrouped into several different configurations depending on the type of measurement. For example, the MuSR detectors consists of 64 scintillator segments that are usually grouped into forward and backward banks for longitudinal configuration, or 8 individual groups for TF mode. The latter is accessed by rotating the instrument through 90° with respect to the beamline. Available sample environments include TF fields of up to 0.25 T and variable-temperature cryostats which allow temperatures down to 40 mK. The EMU spectrometer consist of 96 detectors and is optimised for ZF or LF measurements in fields of up to 0.45 T and temperatures down to 50 mK.

The General Purpose Spectrometer (GPS) at PSI consists of 6 positron detectors; with respect to the muon beam, these are the forward, backward, up, down, right, and (more recently) left. In addition, a forward veto detector is used to reject muons that have not stopped in the sample. Available sample environments include fields of up to 0.6 T (applied parallel to the beam) at temperatures down to 1.8 K, and TF measurements can be made via a 'spin rotator'. The spin rotator is a beamline device consisting of mutually perpendicular electrical and magnetic fields that rotate the muon spin upwards by 50° (used as a separator to filter out certain velocities

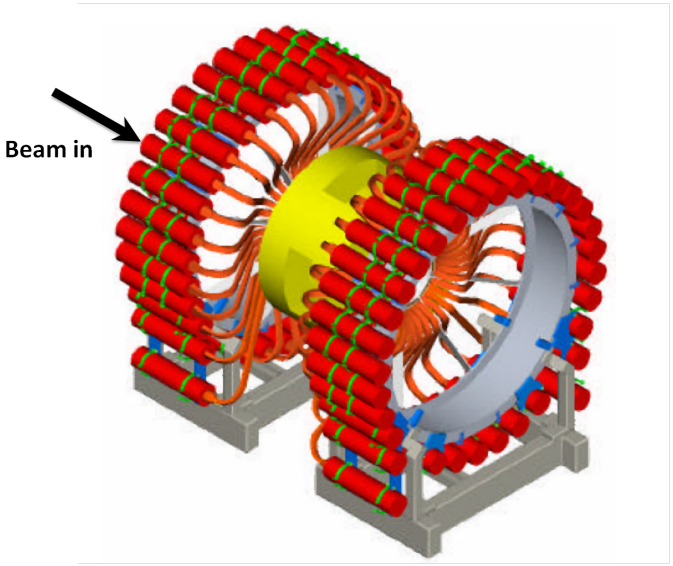

Figure 2.6: Schemtic of the MuSR detector banks at ISIS, from [14]. 64 scintillator tubes are arranged in two circular arrays.

in longitudinal mode). The instrument may be used simultaneously with the Low Temperature Facility spectrometer (LTF), with which it shares a beamline. This is a 4-detector spectrometer optimised for low temperature measurements (11 mK–10 K) in fields of up to 3 T. The new high-transverse field instrument HAL-9500 will be addressed in detail in chapter 3.

In summary, it can be seen that μSR has a wide range of applications in condensed matter physics. However, until now we have assumed that the muon is an innocent probe in all of these processes. A crucial question for these experiments is to what extent, if any, the presence of an implanted muon might perturb its local environment and if it does, whether the measured response reflects the nature of such distortions as well as the intrinsic magnetic behaviour. This is one of the main questions which will be addressed in this thesis in the context of frustrated magnetic materials.

2.2 Pulsed-field magnetometry

2.2.1 Basic principles

The previous section was concerned with microscopic measurements of magnetic properties using μSR. This section will now discuss a bulk technique; high-field magnetometry. Magnetic fields may be generated by either direct-current (DC) or pulsed-field electromagnets. DC systems provide continuous fields using either resistive or superconducting solenoids, or a combination of the two (hybrid systems) [15]. However, magnetic fields of the order of 40 T and above can only be achieved using pulsed-field magnets that consist of resistive wires, usually made from some highly conductive copper alloy, which are energised with short pulses of extremely high currents. These systems offer higher fields at lower operational cost, although they are limited by their generally smaller bore size, amount of resistive heating and, as with all electromagnets, the stress exerted by the Lorentz-force (proportional to the square of the magnetic field strength, and often several GPa [16]). There are also magnets capable of producing even higher fields, in excess of 1000 T using destructive single-turn coils, although these will not be discussed in this thesis.

The measurements presented in this thesis were taken at the NKMFL using magnet HJ45, capable of producing pulsed fields in excess of 45 T, currently the highest available in the UK for condensed matter experiments [16]. The magnet consists of a hardened copper coil with a bore of 1.5 cm and is strengthened with epoxy resin impregnated with Zylon fibre. The system is powdered by a 32 mF, 7kV capacitor bank that is subdivided into quarters and the system is connected in series to a high voltage thyristor. Initially insulating, the thyristor acts as a fast-acting, high current switch that, once triggered, turns conducting and remains in this state as long as the applied voltage is not reversed. During each measurement, the capacitors are charged to a desired voltage at which point the thyristor is triggered by a laser, closing the

circuit to allow current to flow through the magnet and inducing a field. A diode and a 'crow-bar' resistor is placed in parallel with the capacitor banks and magnet to prevent the system, which is essentially an underdamped LCR circuit, to resonate past the first half-oscillation. The pulse-width $\sqrt{LC}/2\pi$ may be adjusted by changing the number of capacitors used to supply the current and hence capacitance C (see Fig. 2.7). This is useful for when the sample is sensitive to resistive heating effects from eddy currents, which are more apparent with higher $\mathrm{d}B/\mathrm{d}t$. By changing the number of capacitor banks used for each run, $\mathrm{d}B/\mathrm{d}t$ may be reduced from 18 to $9\,\mathrm{kTs}^{-1}$.

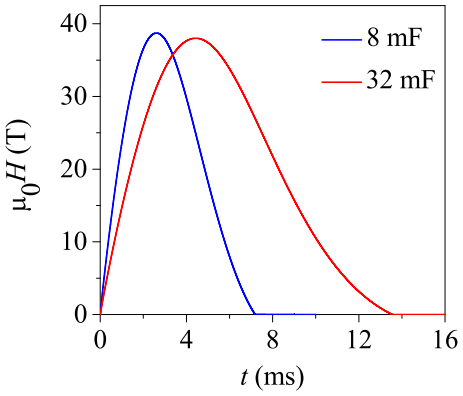

Figure 2.7: Typical time profile of pulsed magnetic field. The pulse length is lengthened with increased capacitance of the energy supply system.

The pulsed-field work in this project has involved several different measurement probes, which will be described in detail in the following sections. In each case, the probe is fitted with a set of pick-up coils, a heater, and a thermometer. The sample is mounted in a pick-up coil on the tip of the probe which is then inserted into a ^{3}He jacket with a non-metallic tip. This is lowered into a ^{4}He cryostat that positions the coil in the centre of the magnet bore [see Fig. 2.8]. The magnet itself is immersed in a liquid nitrogen bath, separated from the cryostat by a vacuum layer, to dissipate the resistive heat generated in the magnet from each current pulse (for example a 32 mF,

45 T pulse requires up to one hour of cooling time in between pulses). Reducing the pressure of the ^{3}He/^{4}He baths allows for base temperatures of around 300 mK.

2.2.2 The Magnetisation probe

Under an applied field H, a magnetised sample will have a time-dependent magnetisation M proportional to the induction B given by $B = \mu_0(H + M)$. This is measured with a compensated coil magnetometer consisting of three coils; a 1500-turn gradiometer, a single-turn compensation coil and a 10-turn 'B-dot coil'. In this set-up, the sample is mounted in an ampoule made from polychlorotriuoroethylene [17] which can be moved in and out of the gradiometer coil in between each measurement. During a field pulse, a voltage will be induced across the coil

$$V \propto \frac{\mathrm{d}H}{\mathrm{d}t} + \frac{\mathrm{d}M}{\mathrm{d}t}, \tag{2.12}$$

where the first and second components relate to that produced by the applied field and magnetised sample, respectively. The gradiometer is designed such that $\frac{\mathrm{d}H}{\mathrm{d}t}$ is minimised; this is done by using two concentric pick-up coils of 50 gauge high-purity copper wire which are connected in series and wound in opposite directions (1000 turns in one direction and 500 turns in the other) [18]. The purpose of this configuration is to reduce the induced voltage produced by any field with a near-uniform spatial distribution in the region probed by the pick-up coils, thus ensuring that the signal resulting from the applied field is suppressed whilst maintaining that produced by sample. The compensation coil signal is then used with a predetermined weight to subtract the remaining $\frac{\mathrm{d}H}{\mathrm{d}t}$. This is calibrated using 10 T pulse performed on an empty coil; the signals are amplified and added/subtracted such that the combined gradiometer and compensation signals give zero voltage. Any additional background is omitted by repeating each measurement (i.e. of equivalent temperature and field)

with an empty gradiometer coil and subtracting this from the corresponding sample data. Thus the signal becomes

$$V \propto \frac{\mathrm{d}M}{\mathrm{d}B} \times \frac{\mathrm{d}B}{\mathrm{d}t}, \tag{2.13}$$

where $\frac{\mathrm{d}B}{\mathrm{d}t}$ may be calculated by the voltage induced in the B-dot coil, given by $V = -NA\frac{\mathrm{d}B}{\mathrm{d}t}$ (where N = 10 is the number of turns of area A). The magnetisation $M(B)$ is found by dividing V by $\frac{\mathrm{d}B}{\mathrm{d}t}$ and integrating with respect to B. The large $\frac{\mathrm{d}B}{\mathrm{d}t}$ makes this technique highly sensitive to small changes in $M(B)$ and thus is highly suited for mapping out magnetic phase transitions.

2.2.3 The PDO probe

Basic principles

Most radio frequency (RF) contactless conductivity techniques utilise an LCR circuit in which either the capacitance or inductance of the circuit is coupled to the sample. Changes in its physical properties, such as magnetic, dielectric or electronic properties, cause a shift in the resonance frequency of the tank circuit. Thus, by measuring the changes in resonance frequency one may directly probe the physical response of the material. One advantage of RF techniques is their high sensitivities (due to high quality factors), which have recorded signals down to 1 part in 10^9 [19]. Their contactless nature makes them suitable for materials with poor surfaces or highly reactive samples that cannot be exposed to atmosphere (such as in the case of the Fe-based superconductors, as demonstrated in Chapter 5). Moreover, they provide a high speed data acquisition rate that is required for pulsed-field experiments (pulse lengths typically up to tens of ms) at frequencies of $\sim 10\,\mathrm{MHz}$, and hence sample response rates of $\sim 0.1\,\mu\mathrm{s}$ may be digitised directly [20].

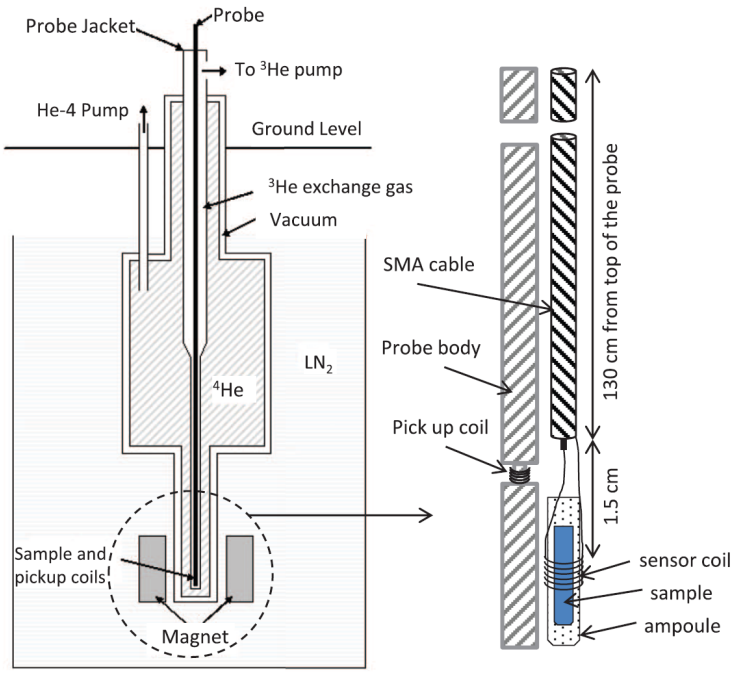

Figure 2.8: Diagram of the cryostat and PDO probe design (taken from [20]).

The PDO probe utilises a relatively new RF circuit, the Proximity Detector Oscillator (PDO), based on the widely available proximity detector chip that is used in modern metal detectors (first reported by Altarawneh *et al.* [21]). The set-up involves placing a single crystal (or ampoule filled with sample, in the case of polycrystalline samples) in a small sensor coil which is inductively coupled to the PDO with a coaxial cable. A typical coil of diameter $\sim 1\,\mathrm{mm}$ consists of 5–10 turns of copper wire of minimum diameter $25\,\mu\mathrm{m}$. One advantage of this system is that it requires very little space within the cryostat itself as the PDO components are placed on top of the probe, far away from the sample space, making it highly suitable for use in pulsed-field systems, pressure cells, and in conjunction with angle rotators where there is limited probe/sample space available. The PDO is also capable of operating across a wide range of temperatures and inductances with a broad dynamic frequency range that is insensitive to bias change (and hence voltages that may be induced by large $\frac{\mathrm{d}B}{\mathrm{d}t}$ in pulsed-fields) [21]. To ensure maximum coupling, the coil is made to match the

size and shape of individual sample as closely as possible and it is the changes in the resonator filling factor (the ratio of the volume of the sample penetrated by the RF field to the total volume of the sensor coil) that allows one to probe the material's transport properties. In metals, the filling factor is determined by the skin depth, and in superconductors it is representative of penetration depth, thus any changes of the filling factor and hence the PDO resonance frequency can be used to observe magnetic or superconducting phase transitions.

Recently, it has been found that in insulating materials,the PDO circuit response is dominated by magnetic susceptibility [20, 22]. The next section will present a brief description of this technique, which will be used in Chapter 5. A more detailed explanation may be found in Ghannadzadeh *et al.* [20, 22].

Experimental set-up

A schematic of the PDO probe circuitry is shown in Fig. 2.9 [21, 20]. The PDO operates as a negative resistor that compensates for any loss in the tank circuit to maintain oscillations in current. The sensor coil, with inductance L_0, is inductively coupled to pins 3 and 7 of the circuit and the load impedance (R_{3-7}) measured across 3 and 7 is compared to that measured across pins 2 and 4 (R_{2-4}). When the circuit experiences an extra inductive load such as that sensed from a metal object, the change in R_{3-7} with respect to R_{2-4} will modify the current drawn from pin 1, which in turn modifies the metal detector read-out signal. In the PDO probe setup, terminals 2 and 4 are short-circuited to establish a constant resonance in the circuit (it will oscillate only if $|R_{3-7}|>R_{2-4}$), and R_2 and C_3 are included to ensure a stable operating voltage. The capacitors C_1 and C_2 are used to tune the resonance frequency ω and this is read out across the coupling capacitor C_4. Recall that the PDO technique relies on detecting changes in the penetration depth λ, which therefore must be smaller than the sample radius. As the frequency and penetration depth are

inversely related via $\lambda = \sqrt{\frac{2\rho}{\omega\mu_r\mu_0}}$ (where ρ is the sample resistivity) the PDO remains sensitive to small samples if ω is maximised, and thereby λ is minimised [21, 20].

For this set-up, the PDO circuit is coupled to the sensor coil using a coax cable such that it is electrically isolated from the probe jacket and placed outside of the cryostat. It is connected by an SMA cable to a separate box containing the capacitor C_4 and a 9 V battery to power the tank circuit. To remove high-frequency noise, the output signal is amplified and passed through a two stage mixing and filtering process and recorded using a fast data-acquisition card. A fast Fourier transform is used to extract the shift in resonance frequency, which is correlated with the applied field to give the field-dependent behaviour.

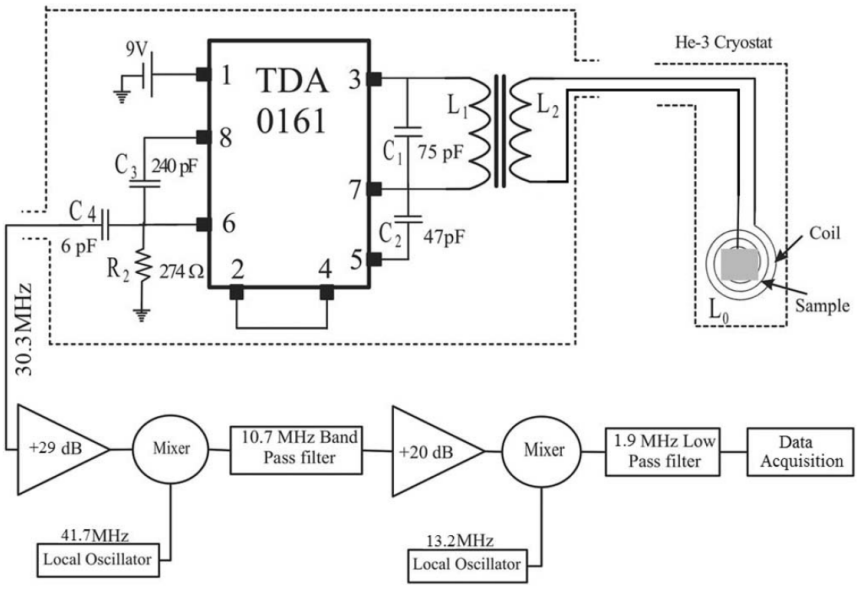

Figure 2.9: Schematic diagram of the PDO probe circuitry, taken from [20]. The sensor coil with inductance L_0 is coupled to the PDO chip via inductances L_1 and L_2.

For our measurements, The resonance frequency was tuned to $\omega \approx 30\,\text{MHz}$. As the probe forms an LCR circuit, this is given by

$$\omega = \frac{1}{\sqrt{L_{\text{eff}}C}}, \tag{2.14}$$

where C is the total capacitance of the circuit and L_{eff} includes contributions from L_0, L_1,L_2, the sensor coil, and the coaxial cable [20]. A change in magnetisation of the sample will modify the coil inductance and the relative change in resonance frequency is calculated by differentiating Eq. 2.14. Assuming that C is fixed, this gives

$$\left|\frac{\Delta\omega}{\omega}\right| = \left|\frac{\Delta L_{\text{eff}}}{2L_{\text{eff}}C}\right|. \tag{2.15}$$

By applying circuit theory to Fig. 2.9, and after some differentiation and substitutions, one can obtain a direct relationship between $\Delta\omega$, λ and the samples magnetic permeability μ_{r} (see Ghannadzadeh *et al.* [20]);

$$\Delta\omega = 2a\mu_{\text{r}}(r-\lambda)\Delta\lambda + a(2r-\lambda)\lambda\Delta\mu_{\text{r}} - b\Delta R_0. \tag{2.16}$$

Here, R_0 is the coaxial resistance, r is the sample radius, a and b are positive constant functions of R_0, ω, C, inductances $L_{0,1,2}$ and coil dimensions. As mentioned earlier, in metals (superconductors) the skin (penetration) depth is small ($r, R \gg \lambda$) such that all terms containing λ drop out and the PDO signal becomes dominated by changes in the skin/penetration depth $\Delta\lambda$;

$$\begin{aligned} \Delta\omega &= -a'\Delta\lambda - b\Delta R_0, \\ a' &= afL_{empty}, \end{aligned} \tag{2.17}$$

where $f = r^2/R^2$ is the coil filling factor and L_{empty} is the empty coil inductance. For insulators, the RF field penetrates the whole of the sample volume ($\Delta\lambda = 0, \lambda = r$) and the PDO behaves as a susceptometer. By substituting the susceptibility $\chi = \mu_{\text{r}} - 1$, Eq.2.16 becomes

$$\Delta\omega = -a'\Delta\chi - b\Delta R_0. \tag{2.18}$$

To isolate χ, the background $\Delta_{\text{bg}} = -b\Delta R_0$ is measured with an identical empty

coil and subtracted from the sample measurements. Setting $\Delta\chi = \chi(H) - \chi_0$ with constant χ_0 gives the dynamic susceptibility;

$$\chi(H) = \frac{1}{a'}(\Delta\omega_{\mathrm{bg}} - \Delta\omega_{\mathrm{sample}}) + \chi_0. \tag{2.19}$$

2.3 Example: [Cu(pyz)(gly)]ClO_4

To illustrate the use of the PDO as a susceptometer, I shall now describe in brief some experiments that were carried out in order to study the H–T phase diagram of the dimer [Cu(pyz)(gly)]ClO_4, the results of which were published as part of collaborative work between Oxford, Durham, Warwick and Los Alamos National Laboratory [23]. This study illustrates one popular avenue of research in magnetism which is geared towards gaining control of and understanding chemical building blocks in order to achieve desirable magnetic behaviour [24]. In this context, coordination polymers such as these have generated a lot of interest in recent years due to their low dimensionality which makes them easier to treat theoretically than other three-dimensional materials. Applying a magnetic field to these and other dimerised systems has led to novel long-range magnetic phases. In this case, I shall show how an applied magnetic field will drive the system from a quantum disordered ground state via a quantum critical point into a magnetic phase reminiscent of the Bose-Einstein condensation (BEC) of magnons [25, 26].

2.3.1 Material characterisation

Coordination polymers are self-organising materials consisting of arrays of metal ions that are linked together via molecular ligands. The structure of [Cu(pyz)(gly)]ClO_4 (space group $P2_1/n$) is based on a lattice of alternating Cu^{2+} dimers shown in Fig. 2.10. The dimers are formed by two $S = 1/2$ Cu^{2+} ions that are coupled via

a pyrazine (pyz) ligand and tethered together with glycine (gly) bridges. This forms a quasi-two-dimensional structure with non-coordinating ClO_4^- lying in between.

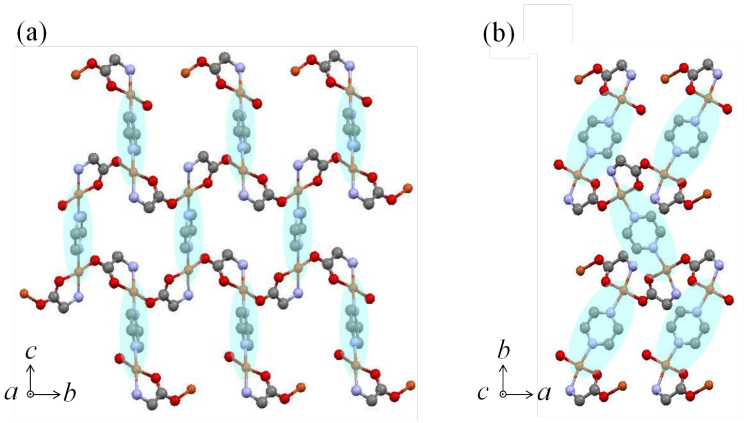

Figure 2.10: Cu-(gly)-Cu dimers (shaded) viewed along the a-axis (a) and c-axis (b) in [Cu(pyz)(gly)]ClO_4 (ClO_4 ions and H atoms omitted for clarity). Brown spheres are Cu atoms, red spheres are oxygen atoms, purple spheres are nitrogen and grey spheres are carbon.

Sample growth was done by J. L. Manson and students. Static magnetic susceptibility and heat capacity measurements were carried out by L. Huang and J. Wosnitza and are shown in Fig. 2.11 with a magnetic field applied along the c-axis. The susceptibility data are well described by the Bleaney-Bowers model [27] which gives the susceptibility of a system of isolated antiferromagnetically coupled dimers. ZF μSR measurements on a polycrystalline sample were performed by T. Lancaster, J.S. Möller, P. J. Baker, F. L. Pratt, and S. J. Blundell using the HiFi spectrometer at ISIS, RAL. These data do not show any signature of magnetic order or any detectable relaxation due to fluctuating electronic moments, but instead show typical relaxation due to disordered nuclear moments down to 32 mK [23]. These findings suggest that the spins interact via the Hamiltonian described by

$$\mathcal{H} = J_0 \sum_i \boldsymbol{S}_{1,i} \cdot \boldsymbol{S}_{2,i} + \sum_{\langle mnij \rangle} J_{mnij} \boldsymbol{S}_{m,i} \cdot \boldsymbol{S}_{n,j} - g\mu_B H \sum_{\langle ni \rangle} S^z_{m,i}, \tag{2.20}$$

where H is the applied magnetic field, $J_0 = 7.5(1)$ K is the antiferromagnetic in-

tradimer exchange coupling, and i, j are dimers occupying the XY plane, with magnetic sites m, $n = 1, 2$ [25]. The first two terms represent the intra-dimer and inter-dimer exchange couplings, respectively, and the third is the Zeeman splitting term. If J_{mnij} are weak compared to J_0, then the system forms a network of $S = 0$ spin singlets, and the groundstate remains quantum disordered down to absolute zero in the absence of an applied field.

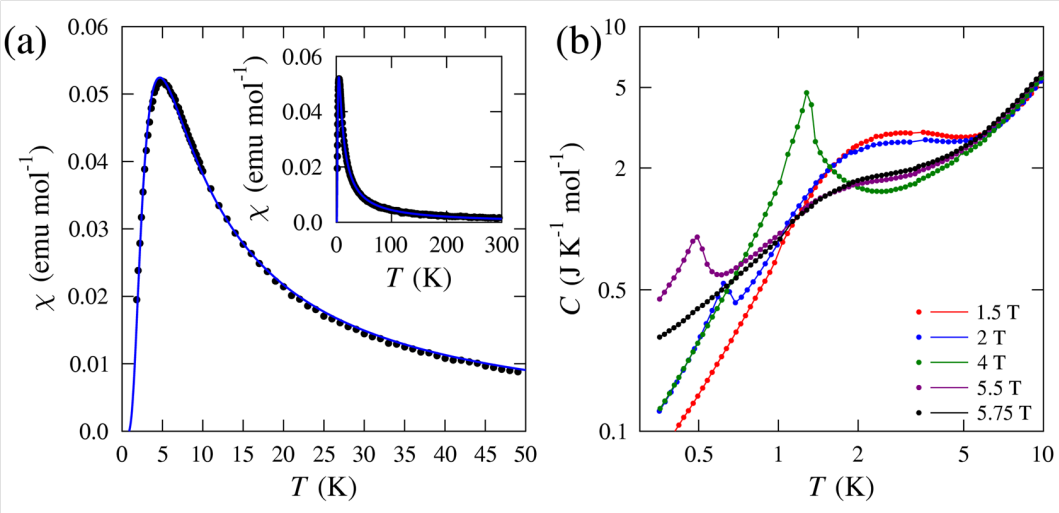

Figure 2.11: (a) Static magnetic susceptibility data for [Cu(pyz)(gly)]ClO_4 measured in a field of 5 mT applied along the c-axis. A fit is shown to the Bleaney-Bowers model of non-interacting dimers (see text). (b) Heat capacity measurements showing magnetic transitions in various magnetic fields strength applied along c.

2.3.2 Dynamic susceptibility measurements

Our sample was a single crystal mounted with the field H applied in two different orientations. These were confirmed by x-ray diffraction to be close to the normal to the (122) and (110) crystal planes, the latter being parallel to the a–b plane that contains the dimers. When compared with μSR and heat capacity data, previous pulsed-field measurements by colleagues at Los Alamos National Laboratory were found to be affected by an unknown amount of heating of the sample due to the magnetocaloric effect, in which the sample temperature changes in a varying magnetic field. This

was brought about by a large dB/dt generated during the short magnetic pulse, whose time scale lends a degree of adiabaticity to the measurement, which resulted in a difference between the measured and actual sample temperature that cannot be easily corrected.

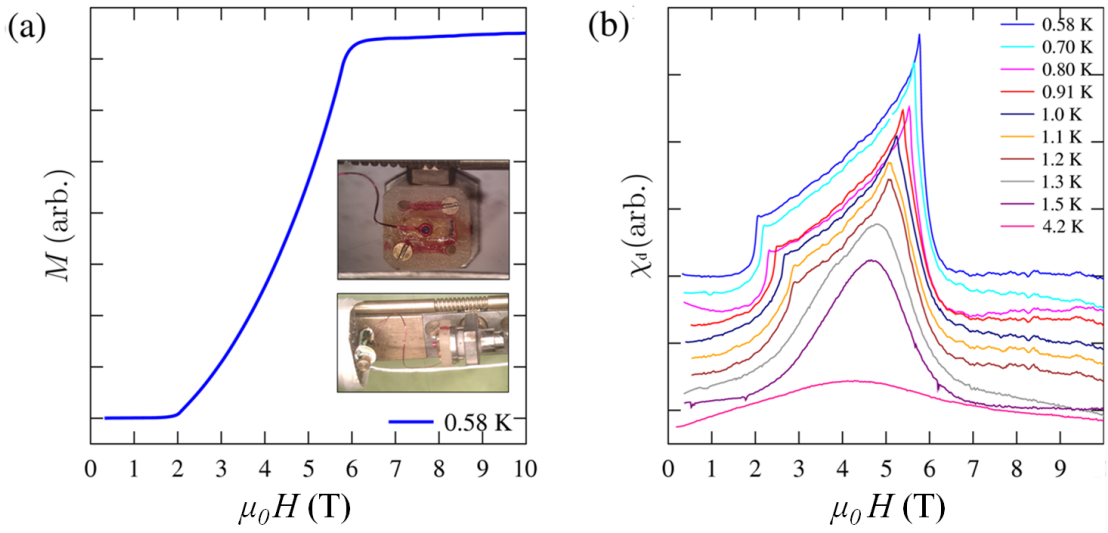

Figure 2.12: Magnetisation at 0.58 K (a) and dynamic susceptibility χ_d (b) for [Cu(pyz)(gly)]ClO_4 with the applied field H normal to (110) at various temperatures measured using the PDO technique. Kinks in χ indicate the magnetic phase transitions (data are offset for clarity and with background subtracted). Inset to (a) shows the sample mounted on the double-axis rotator at the end of the probe.

To resolve these issues, we have repeated the measurements using the PDO described in section 2.2.3 inside an Oxford Instruments 16 T DC superconducting magnet [1]. These measurements were performed by myself with the assistance of S. Ghannadzadeh and P. A. Goddard. The pick-up coil consisted of 8 turns of 75 μm-thick Cu wire, with a diameter of 0.8 mm and was placed on a custom-designed double-axis rotator to allow measurements in the two different orientations. Example dynamic susceptibility $\chi_d = dM/dH$ data and the resulting magnetisation integral is shown in Fig. 2.12. The background signal was measured using an empty coil in both ori-

[1] Additional analysis of the heat capacity and measurements of the magnetocaloric effect on this material has shown that the pulsed magnetic field measurements on this and related materials approach the adiabatic limit, while the DC-field susceptometery experiments described above are isothermal.

entations and subtracted from the data. Sharp features in χ_d indicate a magnetic transition into a long range ordered (LRO) phase which, when measured over the full temperature range, results in the phase diagram shown in Fig. 2.13(a). This transition is also observed in heat capacity measurements on a single crystal, which show sharp peaks in scans across the temperature range $0.4 < T < 1.4\,\mathrm{K}$ (see Fig. 2.11b), and in TF μSR measurements on a polycrystalline sample. The latter is observed as rapid rise in relaxation [23], similar to that observed for field-induced transitions in other molecular magnets of this kind [28]. Note that the phase diagram is plotted in units of $g\mu_B\mu_0 H_c$ as phase boundaries for different measurements showed some variation due to dependence on crystal orientation, which reflects the g-factor anisotropy. The g-factor in case of the dynamic susceptibility measurements for the field applied normal to (110) was measured by electron spin resonance and found to be $g^{(110)} = 2.18$ [23]. Scaling the value of $g\mu_B\mu_0 H_c$ such that all boundaries coincided allowed an estimate of g for the rest of the measurements. These were $g^{(122)} = 2.15$ for dynamic susceptibility with applied field normal to (122), $g^{\mu SR} = 2.20$ for μSR and $g^{HC} = 2.30$ for heat capacity.

2.3.3 Discussion

This behaviour can be explained by considering a singlet-triplet energy level system for a spin-1/2 dimer with antiferromagnetic exchange. In zero field, the system is spin-gapped with a singlet $S = 0$ ground state and a triply degenerate $S = 1$ excited state. At temperatures well below the intradimer separation, J_0, the ground state is a quantum-disordered paramagnet formed from a sea of singlets [29, 30]. If a field H_z is applied, for example along z, this splits the excited state into triplets via the Zeeman effect and consequently reduces the spin gap of the lowest $S^z = 1$ excited state (see 2.13b). However, in a system such as this, the weak inter-dimer interactions allow the triplet states to behave as delocalised quasi-particles which are able to hop from

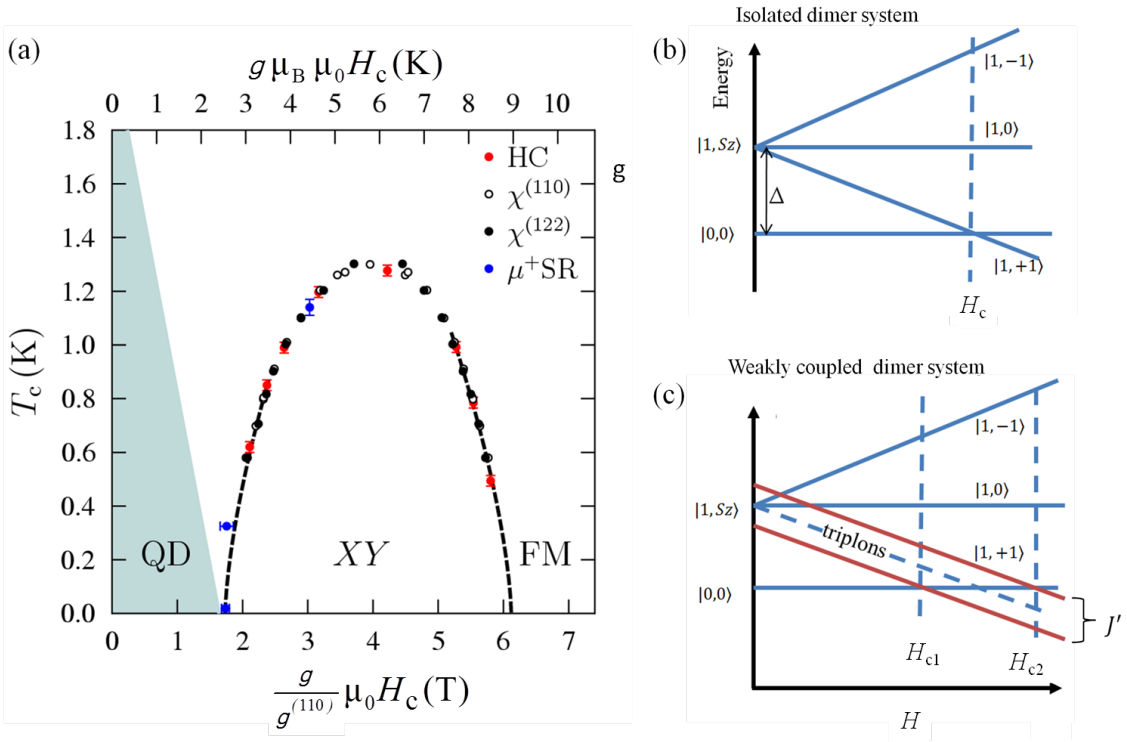

Figure 2.13: (a) The H–T phase diagram of [Cu(pyz)(gly)]ClO$_4$ showing results from dynamic susceptibility measurements (solid and empty black circles), heat capacity (red circles) and μSR (blue circles). The dashed lines indicate fits to $T = (H - H_{c1})^{\phi}$ and $T = (H_{c2} - H)^{\phi}$, which map a long-range ordered phase (LRO) flanked by a quantum disordered state (QD) and ferromagnetic regime (FM). Quantum critical points are observed at $g\mu_B\mu_0H_c = 2.5(1)$ K and 9.0(2) K. The fitted exponent $\phi = 2/3$ agrees with that predicted by the BEC of magnons model. (b) Schematic energy level diagram for a system of isolated spin-1/2 dimers showing Zeeman splitting of the $S_z = 1$ triplet state. (c) The equivalent energy levels for the case of weakly coupled dimers, as in the case of [Cu(pyz)(gly)]ClO$_4$, with energy bandwidth J'.

one dimer to another and form a dispersive energy band, as shown in 2.13(c). For fields $H_{c1} < H < H_{c2}$ the triplet and ground states overlap and the system enters into an XY-ordered antiferromagnetic long-range ordered phase at low temperatures. In this regime, further increasing the field cants the spins in the z-direction, which is observed as a sudden increase of magnetisation until saturation at H_{c2}, at which the system enters a z-polarised ferromagnetic phase. Evidence for this can be seen in the magnetisation data at temperatures $T \ll J_0$, which show zero magnetisation below H_{c1} and a steady increase in M as the field is increased above H_{c1} (in the XY phase) before reaching saturation at H_{c2} (see Fig. 2.12a).

Dimer systems such as these are often described as an approximate realisation of a Bose-Einstein condensate [30, 26]. In this analogy there is an exact mapping between hard-core bosons and $S = 1/2$ spins: interacting "S=1/2" spin systems can then be treated as gases of bosons with hard-core repulsion. The singlet groundstate ($S = 0$) of each dimer in the spin picture is interpreted as the absence of a hardcore boson, and the lowest triplet excited state ($S = 1$, $S_z = 1$) is interpreted as the presence of a hardcore boson, that is, a triplon. Note that the hard-core constraint is included to account for each dimer accommodating a maximum of one triplon at a time. Thus at $H < H_{c1}$ the system represents a vacuum of triplons. The spin-gap is closed in applied fields of $H_{c1} < H < H_{c2}$, which enables the formation of triplons, and a linear increase in H causes a linear increase in the boson density. Therefore the magnetic field in the spin picture plays the role of a chemical potential in a traditional BEC. One way of verifying the BEC state in these dimerised systems is via the critical exponent of the phase boundaries [31]. Specifically, we expect $T_c \propto (H - H_{c1})^{\phi}$ and $T_c \propto (H_{c2} - H)^{\phi}$ with $\phi = 2/d$ (d being the dimensionality of the system) near the quantum critical points H_{c1} and H_{c2}, respectively [25]. We find that the LRO boundary fits well to this power law with $\alpha = 2/3$ which supports this model for a 3D BEC.

2.3.4 Conclusion

To summarise, in this section I have demonstrated the use of the PDO as a susceptometer in DC fields for probing the H–T phase diagram of the spin-1/2 dimer material [Cu(pyz)(gly)]ClO_4 . By combining these data with heat capacity and μSR measurements, I have shown how the quantum disordered ground state may be tuned via an applied field through a quantum critical point H_{c1} to an XY antiferromagnetic phase. Upon further increase of field to $H > H_{c2}$, the system enters a ferromagnetic phase as it is fully polarised by the applied field. Fits of the phase boundary close to the quantum critical points return exponent values of 2/3, as expected for a BEC of magnons.

2.4 Low-field magnetic susceptibility

Samples may be characterised prior to μSR or pulsed-field measurements using low-field susceptibility measurements. The static molar susceptibility is given by

$$\chi(H) = \frac{m_{\mathrm{N}}}{m}\frac{\mu}{H}, \tag{2.21}$$

where μ is the magnetic moment, m is the mass of the sample and m_{N} is its molar mass. The behaviour of χ can provide information on the nature of the magnetic interactions, the size of the average magnetic moment, and the critical temperature of any phase transitions. For the studies presented in this thesis, the susceptibility measurements were performed using a Quantum Design Magnetic Property system (MPMS) [32].

The MPMS utilises a DC superconducting magnet that provides a field of up to 7 T and sample temperatures in the range $1.8\,\mathrm{K} \leq \mathrm{T} \leq 400\,\mathrm{K}$, which are adjusted by a variable temperature insert and heater. Samples are mounted inside a gel cap-

sule using Apiezon N grease, and placed in the centre of a drinking straw. This is mounted in the MPMS with the straw inserted coaxially inside a magnetometer coil. The magnetometer coil itself consists of four loops of superconducting wire with the outer loops wound in the opposite direction to the central two loops so that the magnetometer is insensitive to linear gradients of the external field [33]. The coil is coupled to a Superconducting QUantum Interference Device (SQUID) which consists of a superconducting current loop containing two Josephson junctions and whose critical current is proportional to the flux passing through the loop.

When a sample is moved through the detection coils, its magnetic moment induces a current that is proportional to the total flux passing through each loop and, since the detection coils and SQUID form a closed superconducting circuit, any change in flux from a moving sample will produce a change in the persistent current of the SQUID. A measurement of the SQUID output voltage is then used to calculate the magnetic moment of the sample at various temperatures and fields. The voltage takes the form of a $\sin z/z$ curve, where z is the sample position within the detection coils. The most accurate results are obtained for samples that produce a dipolar field distribution, thus samples that are sufficiently smaller than the detection coils but large enough to produce a good signal are desired.

Chapter 3

Pr-based Pyrochlore Oxides

3.1 Introduction: Frustrated systems

Frustration occurs when a system possesses competing interactions whose energies cannot be minimised simultaneously. It is ubiquitous in the sciences, from protein folding to the structure of liquid crystals, but in condensed matter it is mostly observed in the context of magnetic materials. Frustration may be either the result of site disorder in the system, producing a 'random' type of frustration that is observed in spin glasses, or it may arise in an ordered material whose lattice imposes particular constraints on the interacting spins [34]. This chapter will address the latter case which is known as geometrical frustration.

Geometrically frustrated systems normally have a high symmetry with competing interactions resulting in highly degenerate groundstates. Consider the simplest example; Fig. 3.1(a) shows a set of spins with antiferromagnetic interactions arranged on the vertices of a triangle. The energy is minimised when nearest-neighbour spins are aligned antiparallel to each other. This is possible with the first two spins, but the third is left frustrated as it cannot simultaneously satisfy all of its local interactions. Its two possible orientations, up and down, give the same energy and as this holds

for each spin in the system, it follows that the ground state is six-fold degenerate.

A three-dimensional case is also shown in Fig. 3.1 for a set of ferromagnetic spins arranged on the corners of a tetrahedron. This time, the spins are not collinear but oriented along the easy axis such that each spin must point in or out towards the centre of the unit. With ferromagnetic coupling, the lowest energy configuration occurs with the 'two-in, two-out' arrangement as illustrated in Fig. 3.1(b), which results in a three-fold degenerate ground state. If this frozen-in disorder remains down to near-zero temperatures, the system is said to have residual entropy. This property is common to all frustrated systems and was key in the identification of the first frustrated system: crystalline ice.

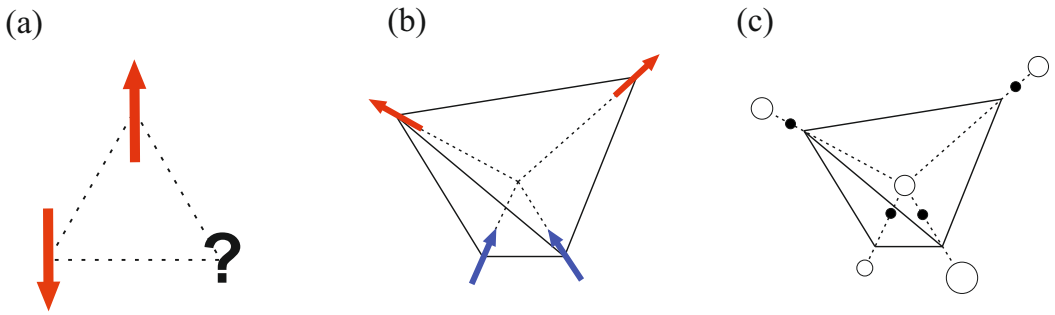

Figure 3.1: Geometric frustration in (a) a 2D triangular lattice of antiferromagnetic spins. The spin denoted with a '?' cannot simultaneously satisfy all of its local interactions. (b) Frustration in 3D for a tetrahedral arrangement of ferromagnetic spins in the 'two-in, two-out' configuration. (c) The equivalent arrangement of protons (black circles) that are covalently bonded to oxygen ions (white circles) in crystalline ice.

The residual entropy in ice was originally measured by Giauque *et al.* in 1933 [35, 36] and later explained by Pauling, who postulated that it was the result of the intrinsic disorder of the protons in the H_2O molecules [37] (a theory originally proposed by Bernal and Fowler [38] and later confirmed by neutron diffraction experiments). To visualise this, one must consider the oxygen ions in the cubic phase of ice, which form tetragonal units as shown in Fig. 3.1(c) in which each oxygen ion is linked to four hydrogen ions. To maintain the H_2O structure, two of the surrounding

hydrogen protons must reside close to the oxygen ion and form covalent bonds, and two sit further away to form covalent bonds with neighbouring oxygen ions. We can see that these conditions, termed 'ice-rules', are equivalent to the 'two-in, two-out' configuration seen earlier in the tetragonal arrangement of spins, where the position of the protons with respect to the tetrahedron correspond to the orientation of the spins. The real magnetic analogue of this proton disorder was first observed in crystals of $Ho_2Ti_2O_7$ [1, 2], which led to the discovery of a new type of frustrated material called spin-ice. In 2008, it was found that fundamental excitations of the spin-ice ground state resembled magnetic monopoles [39], which has since generated a huge interest in the broad family of cubic pyrochlore oxides [40].

In general, the term 'pyrochlore' is used to describe a compound with formula $A_2B_2O_7$, whose A and B ions reside on interlocking lattices of corner-sharing tetrahedra. When either the A or B ions (or both) are magnetic, there is geometric frustration, often giving rise to new and exotic magnetic phenomena such as the magnetic 'monopoles'. Part of this thesis will address the classical spin ices, $Dy_2Ti_2O_7$ and $Ho_2Ti_2O_7$, as well as other pyrochlore oxides. The main technique used in these studies is μSR, whose local nature and extreme sensitivity makes it highly suitable for measuring weak disordered moments. However, as with any measurement techniques, one must also consider the possibility of the probe, in this case the implanted muon, not being a completely passive or 'innocent'. There exist some scenarios in which the muon may perturb its local environment to such a degree that the measured response no longer reflects the intrinsic properties of the system under study. This issue will be addressed in the following section in the context of Pr-based pyrochlore oxides.

3.2 Previous studies

The work described in this section was initially motivated by the possibility of exploring a new type of *quantum spin ice*. In the classical spin ices, Ising-like spins are constrained by the crystal field (CF) to point along the local $\langle 111 \rangle$ axes, which remain static down to near-zero temperatures. By contrast, the magnetic moments in quantum spin ice do not freeze out at low T. Candidate spin liquids include the pyrochlores $Tb_2Ti_2O_7$ [41] and $Yb_2Ti_2O_7$ [42]. Recently, it has been suggested that quantum spin ice [43] may be realised by replacing the A ion by a lanthanide with fewer f electrons and a smaller magnetic moment, such as Pr^{3+} [44, 45]. As the $4f$ wave function is spatially extended, it has a greater overlap with the oxygen $2p$ orbitals and the weaker moment leads to a weaker magnetic dipolar interaction (proportional to the square of the moment size) between nearest-neighbour sites. The result is a reduced Ising barrier that allows tunnelling between different ice configurations, converting the material from a spin ice to a quantum spin liquid. Like its classical counterpart, the most notable feature of this new state is that it is predicted to host unconventional excitations. These are linearly dispersive magnetic excitations (magnetic photons), which offer the possibility of constructing a real lattice analogue of quantum electromagnetism [46, 47].

The compound $Pr_2Ir_2O_7$ has been identified as a highly correlated metallic spin liquid [48, 49] and a previous μSR investigation by MacLaughlin *et al.* found behaviour that was interpreted as being induced by the muon electric field [50, 51], although the extent of the role of screening by the conduction electrons was not clear. In this section, I will demonstrate that this effect can also be found in the insulating compounds $Pr_2B_2O_7$ (B = Sn, Zr, and Hf), which are also candidate quantum spin ice systems. In these systems, the intrinsic magnetic behaviour is that of a quantum spin ice originating from the magnetic moments of Pr^{3+} ($4f^2$) ions. However, the

ground state doublet of this non-Kramers ion due to the high symmetry of the Pr^{3+} site is particularly susceptible to modification by the implanted muon (in contrast, a Kramers ion must have a doublet ground state, whatever the site, and this doublet cannot be split by any perturbation that does not break time-reversal symmetry). By using density-functional-theory (DFT) and crystal-field (CF) calculations, I shall demonstrate that the observed behaviour results from a highly anisotropic distortion field induced by the implanted muon on the crystal lattice.

3.3 The Experiment

3.3.1 Experimental methods

This Chapter is based on work published in Ref. [52]. Samples were grown by D. Prabhakaran, who also performed low-field susceptibility measurements. All data analysis was performed by myself. Samples were synthesised using standard solid-state reactions and confirmed by x-ray diffraction to be single phase. The μSR measurements and relevant analysis were performed by myself, with the assistance of F. Lang, J. S. Möller, T. Lancaster, F. L. Pratt and S. J. Blundell. LF and ZF μSR measurements were carried out mainly using the EMU spectrometer at the ISIS muon facility, Rutherford Appleton Laboratory. An additional set were carried out on the GPS spectrometer at the Swiss Muon Source, PSI. Data were taken in the temperature range 0.05–280 K using a ^{3}He cryostat and ^{3}He–^{4}He dilution refrigerator. The polycrystalline samples were wrapped in 12.5 μm silver foil and, for the GPS measurements, mounted on silver backing plates. A 'fly-past' holder was used for the EMU experiments to minimise statistical noise and background.

High-field magnetisation measurements were performed by myself using the magnetisation probe at NKMFL as described in Chapter 2. Single crystal x-ray diffraction

measurements were performed by myself using a SuperNova (Rigaku Oxford Diffraction) spectrometer, which showed that no detectable impurity phases were present down to the percent level. Crystal field (CF) calculations were performed by A. T. Boothroyd, density-functional-theory (DFT) calculations were done by F. Lang.

3.3.2 ZF and LF μSR

Representative raw spectra from μSR measurements taken in zero applied field at 1.5 K and 40 K are shown in Fig. 3.2. There were no muon oscillations observed in the forward-backward asymmetry across the whole temperature range in any of the compounds, which would have otherwise indicated some long-range order. Instead, the data fit to the product of a Kubo-Toyabe function and a weakly-relaxing exponential, with an additional background component;

$$A(\Delta, \lambda, t) = A_{\mathrm{rel}} G_{\mathrm{KB}}(\Delta, t) e^{-\lambda t} + A_{\mathrm{bg}} e^{-\lambda_{\mathrm{base}} t}, \tag{3.1}$$

where A_{rel} and A_{bg} refer to the signal and background contributions, respectively. The function G_{KB} is the Gaussian Kubo-Toyabe described by Eq. 2.8 with an exponential term that takes into account some slow dynamics of the magnetic moments. The background contribution corresponds to muons stopping in the silver foil and sample holder. Initially, all parameters were allowed to vary. The fits were then refined by fixing the baseline asymmetry A_{bg} and its relaxation rate λ_{base} at their average values. This fit function can be used across the entire temperature range studied and the temperature dependencies of the static width Δ and dynamic relaxation rate λ are shown in Fig. 3.3. A longitudinal field was applied to help separate the static and dynamic contributions in the system and example spectra are shown in Fig. 3.4.

A missing fraction is observed in all of the samples (the initial asymmetry is lower than expected at ~ 0.2) and this can be interpreted as muonium formation. In

this phenomenon, there is a strong spin-exchange between the muon and a captured electron. As the electron is unpolarised it randomises the spin orientation of the muon, resulting in a rapid depolarisation of the muon spin. If this process is too fast to measure, it manifests as a missing fraction in the total asymmetry. Note that this effect is not seen in sufficiently large longitudinal fields, as the applied field aligns the static electron spins and decouples the muon from its environment. Hence, we observe a recovery of the initial asymmetry with increasing LF field (see Fig. 3.4). It is uncertain why there is some negative curvature in the asymmetry at early times, which might relate to some small fraction of muons experiencing a hyperfine coupling. The samples were remeasured at the Swiss Muon Facility, PSI to further investigate this as the continuous muon source offers a better resolution for measuring fast relaxation rates, and the small, missing fraction was still observed in the data. In the subsequent discussion, we will focus on the majority fraction.

3.3.3 Discussion

No magnetic transition can be seen throughout the measured temperature range; both relaxation rates evolve smoothly, increasing steadily as the samples are cooled, and the increase in Δ can be interpreted as magnetic moments that grow with decreasing temperature. The two parameters Δ and λ roughly track each other (see inset to Fig. 3.3), suggesting that the dynamics are related to these growing moments. The background term also displays some weak dynamics, although the relaxation is small ($\sim 0.01\,\mu\mathrm{s}^{-1}$) and temperature independent, as expected from a silver background. This can occur if the assumed field distribution does not fully describe the real physical distribution (for example due to some defects in the sample) as sensed by the muon. Thus some relaxation that should be attributed to the sample may manifest in the background fitting component. For these data, a Gaussian distribution is used and the fit worsens with a Lorentzian Kubo-Toyabe. In any case, there will always be some

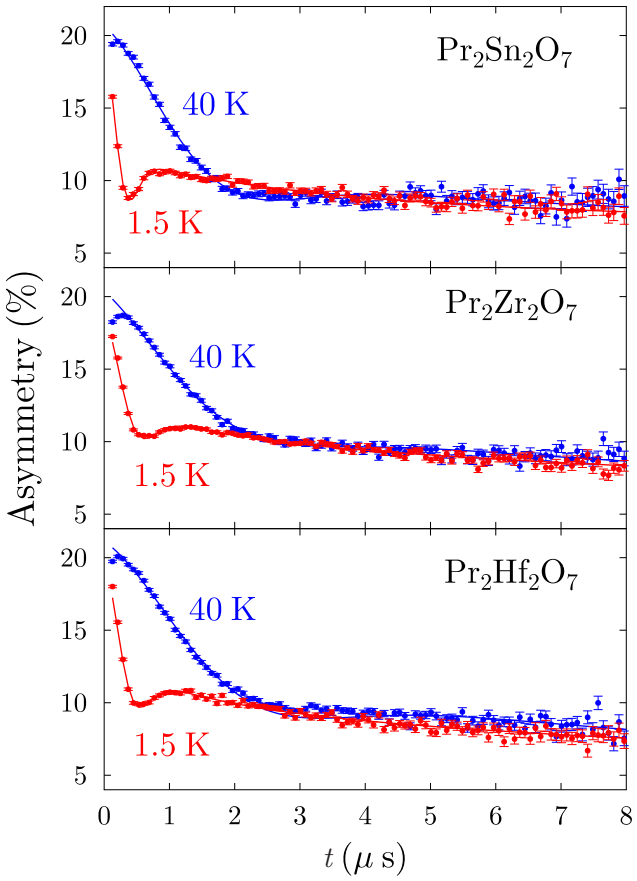

Figure 3.2: ZF μSR spectra at 1.5 K and 40 K. Fits are to a weakly relaxing Kubo-Toyabe function given by Eq. 3.1

discrepancies as the Gaussian function assumes a continuous distribution of fields, whereas in a μSR measurement the values are discrete due to the muons occupying particular crystallographic sites.

The Gaussian lineshape implies that the data are dominated by nuclear moments. However, the values of the rms field width $B_{\rm rms} = \Delta/\gamma_\mu$ extrapolated to zero temperature (see Table 3.1) are found to be an order of magnitude larger than expected from ^{141}Pr nuclear moments [50, 51] and are larger for smaller lattice constants a. In these quantum spin ice systems, one does not expect any static electronic moments at any temperature. Nuclear moments are expected to give a small temperature-independent Δ, but the observed behaviour in Fig. 3.3 is both strongly temperature

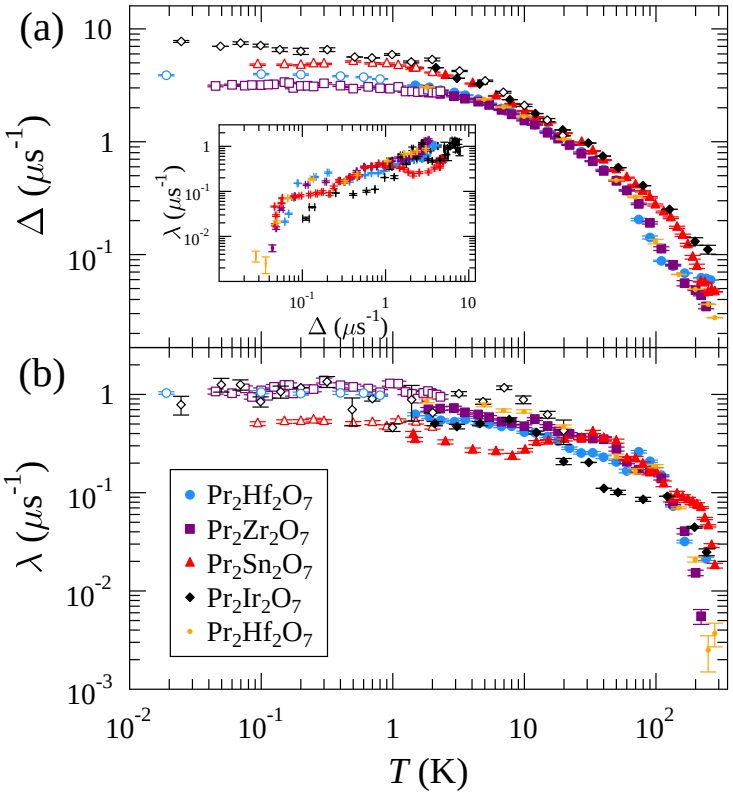

Figure 3.3: Temperature dependences of (a) Δ and (b) λ in the Pr-based pyrochlores extracted from ZF μSR measurements (helium cryostat, filled symbols; dilution fridge, open symbols). The two data sets for $Pr_2Hf_2O_7$ were taken with the same sample but in separate experiments to check reproducibility. The insert shows the correlation between the Δ and λ. The data for $Pr_2Ir_2O_7$ are taken from Ref. [50].

dependent, and at low temperatures, very large. A likely explanation comes via a hyperfine enhancement of the Pr nuclear moments (as proposed for $Pr_2Ir_2O_7$ [50, 51] and discussed in more detail below), but this mechanism requires a non-magnetic (singlet) ground state. In the pyrochlore structure, the Pr^{3+} ($4f^2$) ground state is a well isolated non-Kramers doublet (confirmed in $Pr_2Sn_2O_7$ and $Pr_2Zr_2O_7$ by neutron spectroscopy [53, 54]), however this could be split by the distortion introduced by the muon. A muon-induced perturbation of the CF has been suggested previously in Pr-based intermetallics [55, 56], although in those cases the ground state is already a singlet due to lower symmetry and the effect is only on the excited CF levels. Since the data in the insulating pyrochlores look very similar to those in metallic $Pr_2Ir_2O_7$,

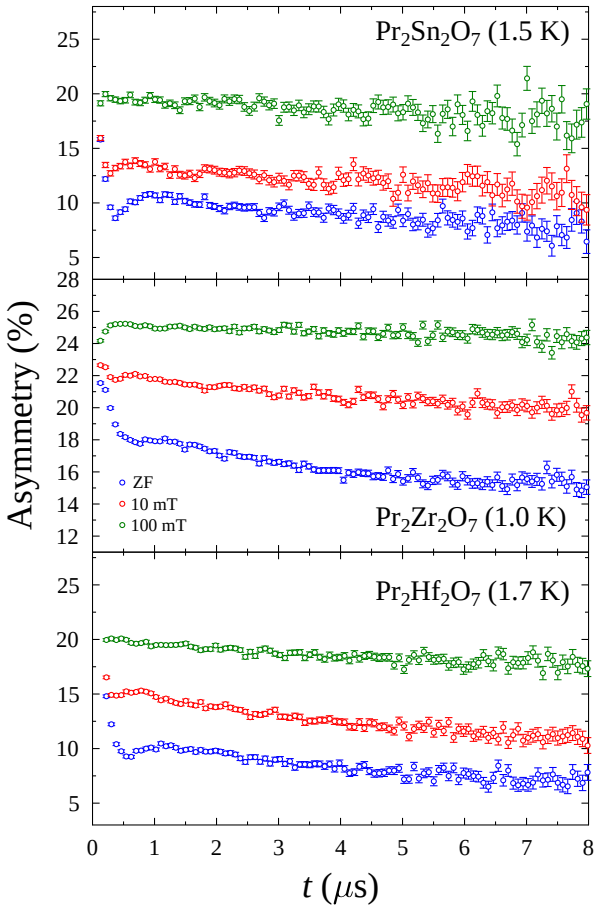

Figure 3.4: Sample μSR spectra taken in a longitudinal field of 100 mT (green points), 10 mT (red points) and in zero-field (blue points). $Pr_2Sn_2O_7$ and $Pr_2Hf_2O_7$ data were taken in the He cryostat at 1.5 K and and 1.7 K, respectively, and $Pr_2Zr_2O_7$ data taken in the dilution fridge at 1.0 K.

we conclude that this mechanism is not very sensitive to conduction-electron screening effects. In fact, the carrier density in $Pr_2Ir_2O_7$ is found to be rather low (estimated to be $2.6 \times 10^{20}\,\mathrm{cm}^{-3}$, i.e. ≈ 0.02 conduction electrons per Pr, from Hall effect measurements [48]). Moreover, $Pr_2Ir_2O_7$ is believed to have a Fermi node at the Γ point [57], so that conduction electrons can only screen effectively at very long wavelengths. However, $Pr_2Ir_2O_7$ has the largest B_{rms} in Table 3.1, which as explained below is related to the smallest doublet splitting and distortion, hence screening effects may play some role.

Although there has been previous evidence for a muon-induced effect in Pr-

containing systems with a non-Kramers doublet [50], the nature of the effects has not been explored in detail. To address this issue, DFT calculations have been used to determine the muon location and assess the effect of the muon on the local crystal structure and the CF of nearby Pr ions. Note this thesis will not cover a detailed account of density-functional theory. For a comprehensive introduction to DFT see Ref. [58].

Compound	Zr	Hf	Sn	Ir
a (Å)	10.7386(2)	10.7177(2)	10.6055(2)	10.3940(4)
B_{rms} (mT)	3.76(6)	4.4(1)	5.65(5)	8.9(4)
ϵ_1 (meV)	3.1(5)	2.1(7)	6(1)	0.5(1)
ϵ_2 (meV)	0.6(1)	0.3(2)	0.6(1)	0.1(1)

Table 3.1: Lattice constants a (extracted from single crystal x-ray diffraction at 300 K), rms field width B_{rms}, and fitted energy gaps ϵ_i (see later) for $Pr_2B_2O_7$ (B = Zr, Hf, Sn and Ir). $Pr_2Ir_2O_7$ data are taken from Refs.[48, 50].

3.3.4 DFT calculations and CF levels

DFT calculations were conducted with the plane-wave *QUANTUM ESPRESSO* [59] program utilising the generalised gradient approximation exchange-correlation functional [60]. Ions were modelled using ultrasoft pseudopotentials and the muon was modelled by a norm-conserving hydrogen pseudopotential. This technique is known to give reliable results for muon sites in condensed matter systems [61, 62, 63]. Two different Pr pseudopotentials were used, with the $4f$ electrons either in valence or in the core. The resulting muon stopping sites and bulk lattice parameters were found to agree in both cases, probably due to the muon forming an OH type bond (see below) making it insensitive to the modelling of the Pr $4f$ electronic configuration. Hence, a Pr pseudopotential with the $4f$ electrons in the core, which is less computationally demanding, was employed for the calculations described below. The calculations were performed for $Pr_2Sn_2O_7$ in a supercell consisting of a single conventional unit cell con-

taining 88 atoms, and with the total energy converging to at least 1×10^{-6} Ry/atom (where Ry is the Rydberg constant). A convergence test yielded the suitable wave function and charge density cutoffs of 50 and 300 Ry, respectively, on a $2 \times 2 \times 2$ Monkhorst-Pack k-space grid, which were then used in all subsequent calculations. The calculated atomic positions and lattice parameter of the unperturbed bulk were within 2% of the experimental values reported in Ref. [64]. Part of this discrepancy stems from the fact that DFT calculations are limited by a small supercell of unit cells that is used to model a real infinite bulk system, and so under these conditions we believe 2% indicates a good level of agreement with experimental observations. A muon was introduced on a grid of low-symmetry positions and the system was allowed to relax until all forces were below 10^{-3} Ry/a.u. and the change in energy between iterations was less than 10^{-4} Ry. The calculations presented here focus solely on the diamagnetic muon state, for which the unit cell has a total charge of +1. The final relaxed positions were found to be the same in spin-polarised and non-polarised calculations.

Fract. Coords.	x	y	z	WP
$Pr_2Sn_2O_7$	-0.0125	0.0471	0.2028	96g
$Pr_2Zr_2O_7$	-0.0115	0.0465	0.2035	96g

Table 3.2: Fractional coordinates of the muon sites and their Wyckoff positions (WP) calculated by DFT. Unit cells are taken to be the experimentally measured cubic ones (lattice parameters $a_{\mathrm{Sn}} = 10.6$ Å and $a_{\mathrm{Zr}} = 10.69$ Å). The origin of the unit cell was chosen such that the fractional coordinates for the different atoms were Sn/Zr:(0, 0, 0), Pr:(1/2, 1/2, 1/2), and for the two oxygen sites O2:(3/8, 3/8, 3/8), O1:(x, 1/8, 1/8), where $x_{\mathrm{sn}} = 0.33148(5)$ for Sn, and $x_{\mathrm{Zr}} = 0.335$ for Zr. For more details, see Ref. [65]

Three potential stopping sites were identified. However, as two of these required configurations that were ~ 0.45 and ~ 0.9 eV higher in energy than that of the lowest state we conclude that the latter is the most plausible stopping site in our real system. In this scenario, the muon forms a OH type bond of length ≈ 1 Å. It is bonded to an

O^{2-} ion, which also bonds to two Pr ions, labelled Pr1 and Pr3 in Fig. 3.5 (the Pr ions in Fig. 3.5 are numbered in order of separation from the muon, with Pr1 being the closest). The implanted muon results in an anisotropic distortion of the crystal lattice as follows. The muon pulls an O^{2-} away from the ion Pr3, resulting in a greatly extended Pr3-O bond. The Pr1-O bond is only slightly changed in length, but is bent round, resulting in an anisotropic distribution of O^{2-} ions around Pr1. As shown below, the largest change in the CF ground state is found for Pr3, but note that the environment around the ions labelled Pr2, Pr2′, Pr4, and Pr4′ is more gently modified.

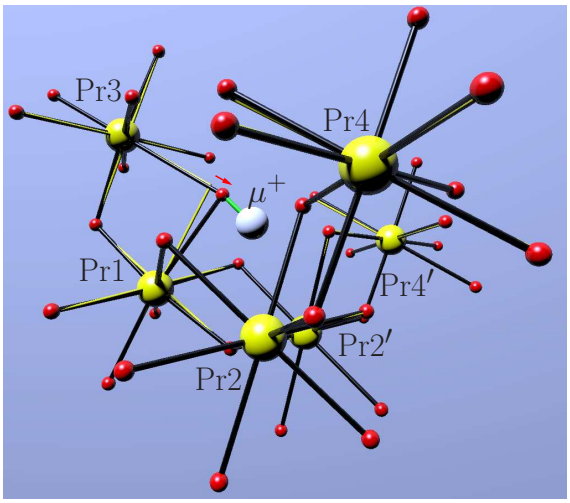

Figure 3.5: Muon stopping site (white sphere) and atomic positions in $Pr_2Sn_2O_7$ as calculated by DFT. Oxygen sites are shown in red, Pr ions are shown in yellow, and bonds are shown as solid black lines. Bonds of the unperturbed lattice (yellow lines) are included for comparison. Pr ions are numbered in order of separation from μ with Pr1 being the closest. The pair Pr2 and Pr2′ is equidistant from the muon, as are Pr4 and Pr4′.

The relative distortion of a PrO_8 unit may be quantified as the rms of the differences in Pr-O bond lengths between the perturbed and unperturbed lattice and these are listed in Table 3.3 for each of the nearest sites in $Pr_2Sn_2O_7$. The CF levels for all nearby PrO_8 environments were calculated by taking into account the spatial arrangement of the eight nearest-neighbour oxygen anions around each Pr ion. The

electrostatic field due to the muon itself was also included initially, but it was found to make little difference, and so was neglected for the calculations described here. The calculations utilised a point-charge model, with effective charges on the O1 and O2 sites chosen to reproduce the measured CF spectrum [53]. For each Pr site, the muon-induced distortion splits the non-Kramers ground state doublet into two singlets (see Fig. 3.6). These calculations show that the most perturbed Pr ion is not that nearest to the muon (there are three closer Pr ions that are significantly less perturbed), reflecting the highly anisotropic nature of the induced distortion field. Thus we conclude that the muon is surrounded by a number of close Pr ions in which the CF splitting varies considerably.

Pr atom	1	$2, 2'$	3	$4, 4'$
Pr–μ separation (Å)	2.7	3.2	4.1	4.7
Relative contribution	0.45	1.0	0.05	0.10
Distortion of PrO_8 unit (Å)	0.23	0.07	0.56	0.09
ϵ (meV)	4.8	1.3	11.4	4.0

Table 3.3: Parameters derived from DFT calculations of muon-induced lattice perturbations in $Pr_2Sn_2O_7$ including the relative coupling of the dipole-dipole interaction between the muon and each Pr moment (assuming a r^{-3} dependence and the induced moment $\propto \epsilon^{-1}$). Values are shown for the four nearest-neighbour Pr ions.

3.3.5 Nuclear hyperfine enhancement

I now turn to the hyperfine enhancement of the Pr nuclear spins caused by these altered CF levels. One can model the system as a two-state one (see Bleaney [66]) in which the non-Kramers doublet is split into two singlets $|G\rangle$ and $|E\rangle$ by a small energy ϵ. For such a system involving a nucleus with spin $\boldsymbol{I}$ the Hamiltonian takes the form

$$\mathcal{H} = \mathcal{H}_{\mathrm{X}} + g_J \mu_{\mathrm{B}} (\boldsymbol{B} \cdot \boldsymbol{J}) + A_J (\boldsymbol{J} \cdot \boldsymbol{I}) - g_I \mu_{\mathrm{B}} (\boldsymbol{B} \cdot \boldsymbol{I}). \tag{3.2}$$

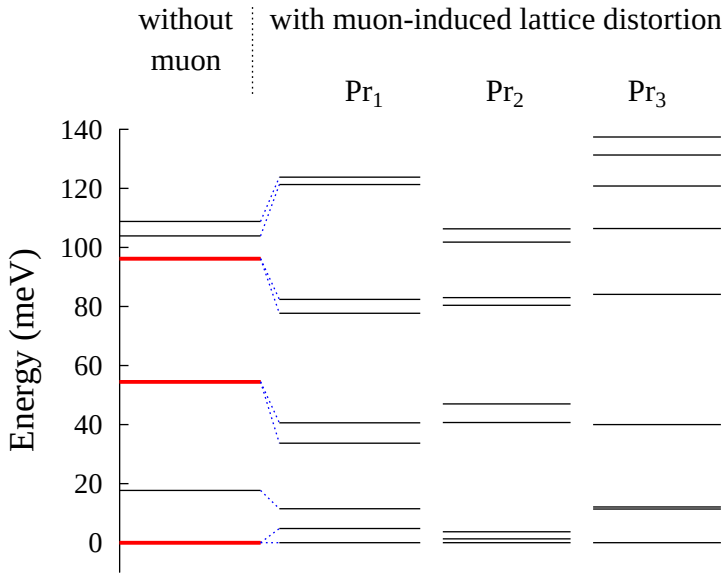

Figure 3.6: Calculated CF levels of Pr^{3+} with and without muon-induced lattice distortion in $Pr_2Sn_2O_7$. Energies are calculated for the three Pr^{3+} sites with varying degrees of distortion (see Table 3.3) as determined by DFT calculations. Bold red lines indicate doublets; plain black lines are singlets.

Here, the field $\boldsymbol{B}$ is applied along the z direction and $\mathcal{H}_X$ denotes the interaction with the CF which causes the splitting of the groundstate doublet. There is an electronic matrix element $\alpha = \langle E| \hat{J}_z |G\rangle$, where $\hat{J}_z$ is the electronic angular momentum. This model allows an estimate of the magnetic moment $m = k_\mathrm{B}T \left(\frac{\partial \ln Z}{\partial B}\right)_T$ where Z is the partition function, and yields

$$m = g_I \mu_\mathrm{B} I_z + g_J \mu_\mathrm{B} \alpha \sin\theta \tanh\left(\frac{\epsilon}{2\cos\theta k_\mathrm{B} T}\right), \tag{3.3}$$

where $\tan\theta = 2\alpha(g_I\mu_\mathrm{B}B_z + A_J I_z)/\epsilon$. In zero-field μSR we take $B_z = 0$ and hence the magnetic moment is reduced to

$$m = m_0 + \frac{\eta}{\tilde{\epsilon}} \tanh\left(\frac{\tilde{\epsilon}}{k_\mathrm{B}T}\right), \tag{3.4}$$

where $m_0 = g_I \mu_B I_z$, $\eta = g_J \mu_B \alpha^2 A_J I_z$, and $\tilde{\epsilon} = \sqrt{(\epsilon/2)^2 + (\alpha A_J I_z)^2}$ (where $\alpha^2 \leq J^2$). Taking $\Delta \propto m$ with $A_J/h = 1.093\,\mathrm{GHz}$ [66] and $I_z = \frac{5}{2}$ allows an estimate of the upper bound of ϵ. The muon is coupled to many neighbouring moments by the dipole-dipole interaction, which is proportional to r^{-3} (the relative contribution of this coupling for each site is listed in Table 3.3, assuming a r^{-3} dependence and the induced moment $\propto \epsilon^{-1}$). For simplicity, we choose a model in which there are dominant contributions to Δ from two nearby moments, which act in quadrature. We note that Eq. 3.4 implies that (neglecting the m_0 component and for $\epsilon \gg \alpha^2 A_J I_Z$) the enhanced moment is approximately inversely proportional to ϵ at low temperature, and therefore we expect the response to be dominated by nearby sites with small splittings.

We now turn to the zero-field muon data and its behaviour with respect to this two-component model. The data are fitted using the function

$$\Delta(T) = \sqrt{\left(\Delta_{01} + \frac{\beta_1}{\tilde{\epsilon_1}} \tanh\left(\frac{\tilde{\epsilon_1}}{k_B T}\right)\right)^2 + \left(\Delta_{02} + \frac{\beta_2}{\tilde{\epsilon_2}} \tanh\left(\frac{\tilde{\epsilon_2}}{k_B T}\right)\right)^2}, \tag{3.5}$$

where the free parameters Δ_{01}, Δ_{02} and β_1, β_2 correspond to scaled values of m_0 and η, respectively, and the fitted values of $\tilde{\epsilon_1}$, $\tilde{\epsilon_2}$ may be used to estimate the splittings of the non-Kramers doublet. The field widths for all compounds are found to fit well to this two-component model (see Fig. 3.7) and the extracted values of ϵ_1 and ϵ_2 are listed in Table 3.1. Note that these values are within the same order of magnitude as the estimated splittings for the nearest neighbour sites Pr1, and Pr2 or Pr2′ for $Pr_2Sn_2O_7$. Given the sensitivity of the calculations to the precise distortion field, the restriction to two components, together with the limitations of the point-charge model of the CF, we believe this agreement is well within the inherent uncertainties.

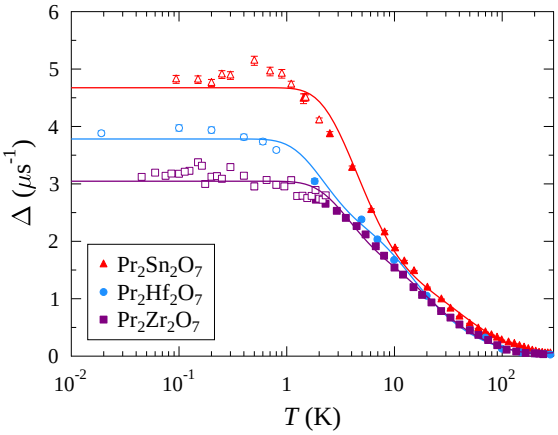

Figure 3.7: Static relaxation rate Δ from ZF μSR fitted with the Bleaney model described in the text (Eq. 3.5). The symbols are the same as in Fig. 3.3.

3.4 Conclusion

In conclusion, the observations of this section show that, in certain circumstances, μSR experiments can measure a response that is dominated by the local distortion resulting from the implanted probe rather than the intrinsic behaviour of the sample. The particular case of $Pr_2B_2O_7$ is unusual since the effect relies on a splitting of a non-Kramers doublet in high symmetry Pr^{3+}. This mechanism would be inoperable in systems in which the ground state degeneracy was protected from such perturbations, such as in $Dy_2Ti_2O_7$, where a similar anisotropic distortion field will nevertheless be induced but will only serve to modify the excited CF levels and will not split the Kramers doublet ground state. This work implies that in any oxide there will always be an anisotropic distortion field around the implanted muon (which I have shown can be modelled using DFT) and its effect should always be considered. In magnetically ordered materials these distortions will have minimal effect because the coupling of the muon to the local magnetic field dominates. If frustration or low dimensionality leads to a less robust ground state then particular care is needed, and especially in the case of high-symmetry non-Kramers doublet ground states, which are most susceptible to these muon-induced effects.

3.5 Further work: TF μSR

We have now seen that in the case of Pr-based pyrochlores the implanted muon is coupled to a range of nearby Pr moments whose CF values have a range of perturbations and hence splittings. To further explore the role of CF splitting in masking the intrinsic behaviour of these systems, single crystals of $Pr_2Sn_2O_7$ and polycrystalline samples of $Pr_2Zr_2O_7$ were measured using the new HAL-9500 spectrometer at the Swiss Muon Facility, PSI. This high-field instrument is optimised for TF measurements via a 'spin-rotator', used to rotate the muon spin direction by 90°, and provides a means to study a previously inaccessible range of the B–T phase diagram with μSR. Available sample environments include a dilution refrigerator for temperatures in the range 0.02–20 K, a He flow cryostat (3–300 K) and a high-homogeneity/short length superconducting magnet providing fields of up to 9.5 T [67, 68].

The aim of the experiment was to use high fields to further perturb the low-lying energy states of different nearest-neighbour ions. As described previously, the maximum CF splittings of the lowest energy levels in these compounds are of the order of 20 meV, with many well below this value. Thus, it was expected that the available fields would be large enough to induce a substantial mixing of states that is observable via the transverse field linewidth measured as a function of field. However, as one of the first experiments performed on this spectrometer, there are still some unresolved features in the data and thus a more detailed understanding of the instrument response is needed for a complete interpretation. Nevertheless, I will present our current understanding of these results in the following section.

Observations

As many pyrochlore oxides require extremely high temperatures, and in some cases pressures, to achieve high-quality single crystals, only polycrystalline samples were

initially available for study. Following the μSR experiments described previously, we have improved growth methods to synthesise high-quality single crystals which were confirmed by x-ray diffraction to be single-phase. The samples were placed in packets of 50 μm thick Ag foil and mounted onto a silver sample holder with GE varnish for TF measurements in fields of up to $B_{\rm app} = 8$ T in the temperature range 2–100 K. The $Pr_2Sn_2O_7$ crystals, which were octahedra of the order of several mm, were mounted on the foil in a mosaic using Apiezon grease and aligned by eye such that the octahedral faces lay flat against the sample mount (i.e. the muon beam was parallel to (111) axis). This was done to ensure that the spins were magnetised along a particular axis throughout the sample, resulting in a better resolved lineshape. Single crystals of $Pr_2Zr_2O_7$ were mounted in the same way. However, the sample size was not sufficient to produce a strong enough signal, hence the original polycrystalline sample was used instead. Example Fourier spectra in the frequency (i.e. field) domain are shown in Fig. 3.8 and Fig. 3.9 for various applied fields at 5 K, with the spectra plotted against the field shift $B = B_{\rm tot} - B_{\rm app}$.

Two distinct peaks are observed in all data sets, including a narrow peak centred close to B=0, whose linewidth $\sigma_{\rm bg}$ and peak position $B_{\rm bg}$ is temperature and field independent. We attribute this to the silver background contribution from the sample cell, and it is larger in the case of $Pr_2Sn_2O_7$ due to the smaller sample size. The data were initially fit to a sum of two Gaussians, but improved slightly with an asymmetric function;

$$\begin{aligned}
&\text{if } B < B_{\rm pk}, \\
&A_{\rm tot}(B) = A_{\rm sa} \exp\left(\frac{-(B-B_{\rm pk})^2}{2{\sigma_1}^2}\right) + A_{\rm bg} \exp\left(\frac{-(B-B_{\rm bg})^2}{2{\sigma_{bg}}^2}\right) \\
&\text{if } B > B_{\rm pk}, \\
&A_{\rm tot}(B) = A_{\rm sa} \exp\left(\frac{-(B-B_{\rm pk})^2}{2{\sigma_2}^2}\right) + A_{\rm bg} \exp\left(\frac{-(B-B_{\rm bg})^2}{2{\sigma_{bg}}^2}\right),
\end{aligned} \tag{3.6}$$

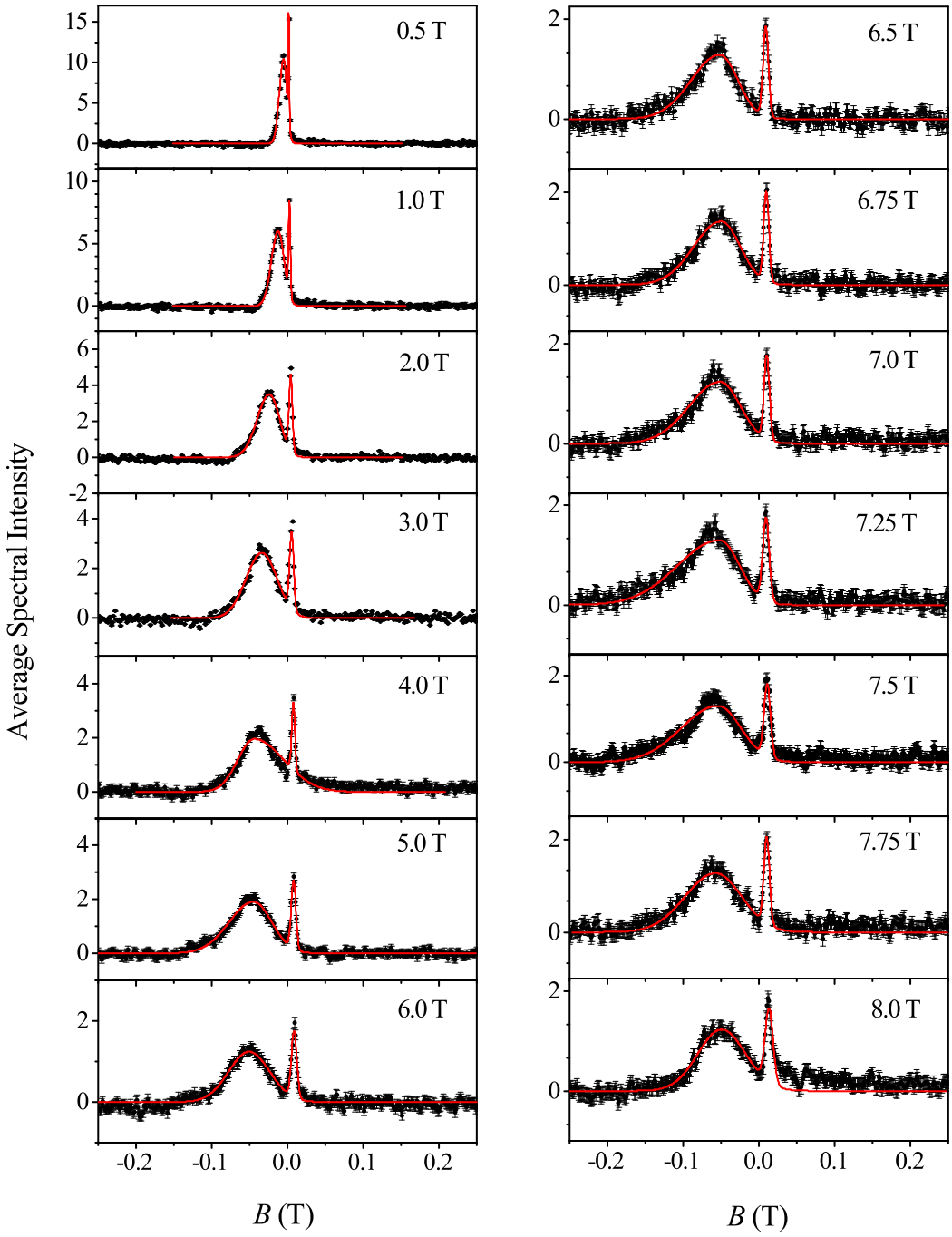

Figure 3.8: Fourier spectra of $Pr_2Sn_2O_7$ measured at 5 K. The amplitude is plotted against the shift in measured field. Fits (red line) are to Eq. 3.6. Due to the smaller sample volume, a higher silver peak is observed compared to that of the Zr data.

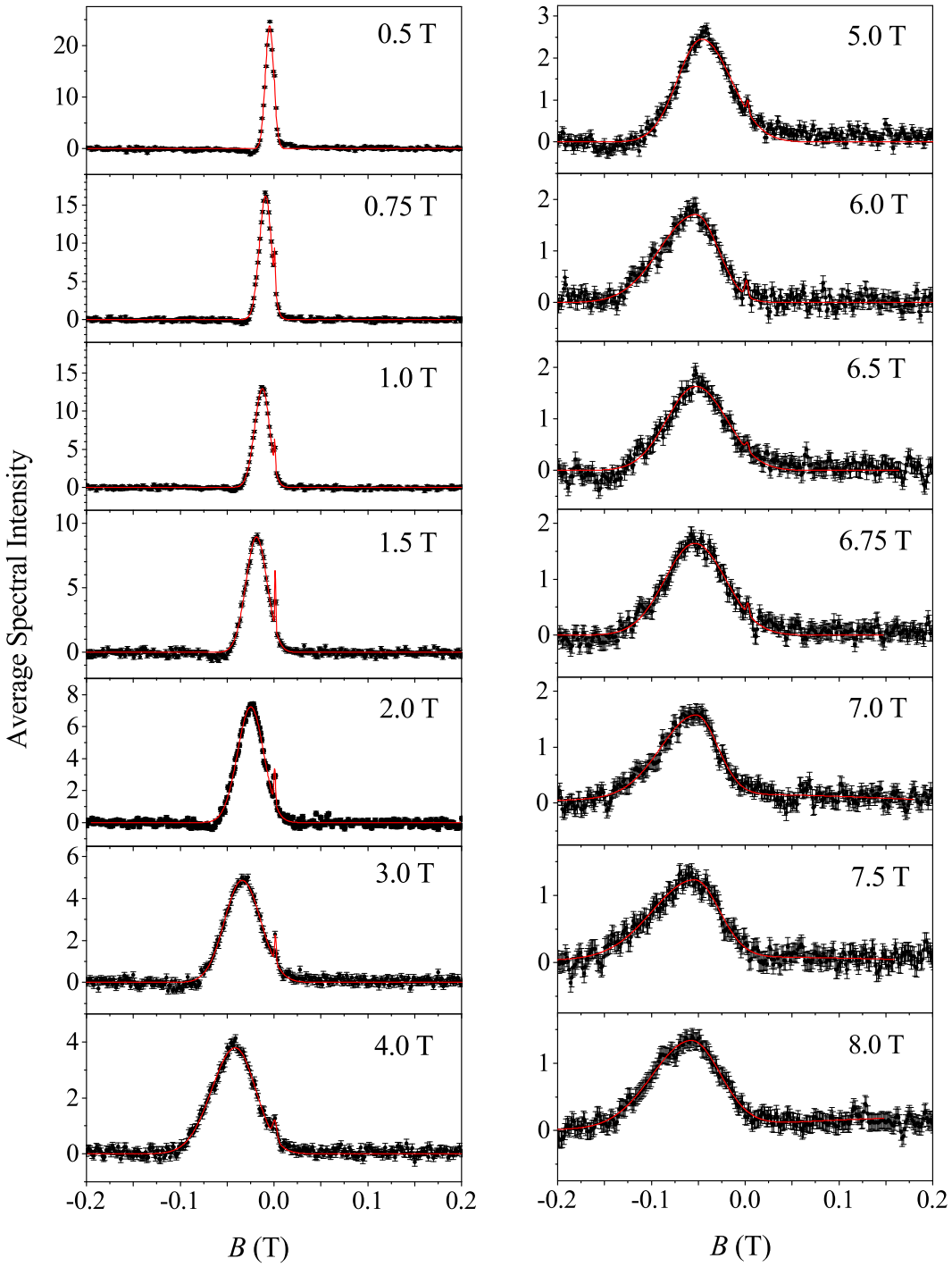

Figure 3.9: Fourier spectra of $Pr_2Zr_2O_7$ at 5 K. Fits (red line) are to Eq. 3.6. The smaller, narrow peak indicates a weak silver background from the silver sample holder.

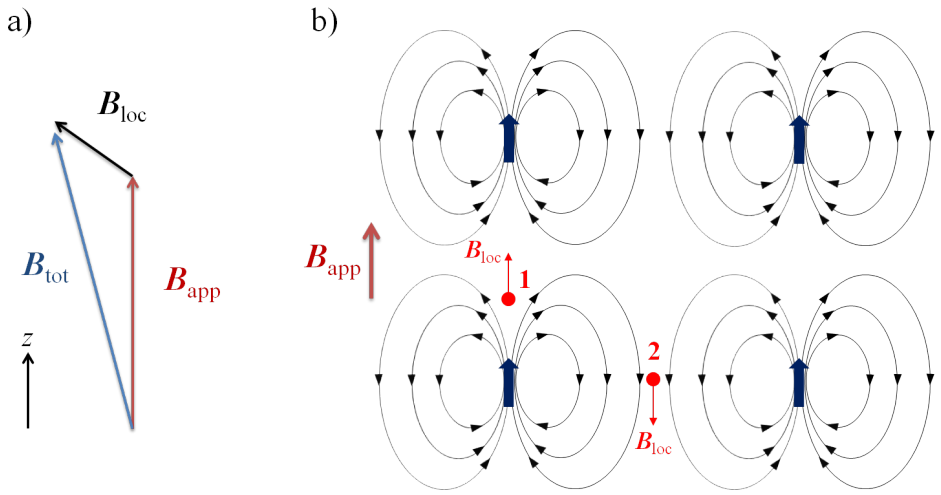

Figure 3.10: a) The total field measured by the muon is a summation of the local field B_{loc} and applied field B_{app}. b) Dipolar fields of a grid of spins aligned ferromagnetically. The direction of B_{loc} with respect to B_{app} varies depending on the muon site. Two possible sites, 1 and 2, are shown with a positive and negative contribution, respectively.

where A_{sa} and A_{bg} are the amplitudes corresponding to the sample and background contributions, respectively. The model assumes an asymmetric Gaussian distribution of fields within the sample only, with an average field B_{pk} and field widths σ_1 and σ_2. The asymmetry parameter is calculated as $A = \frac{\sigma_1 - \sigma_2}{\sigma_1 + \sigma_2}$ and its temperature dependence, along with other parameters is shown in Fig. 3.11. Both samples show a significant amount of broadening in the field width. Whilst the raw data (Fig. 3.8 and Fig. 3.9) do suggest some degree of asymmetry in the local field distribution, the fitted asymmetry parameter does not show any field-dependence (Fig. 3.11), and it is unclear at present whether this feature is of sample or instrument origin.

There is a negative shift in average field B_{pk} and its magnitude increases with increasing field. To interpret this, one must first consider the effect of large B_{app} on the local moments. The total field measured by the muon is a summation of the local

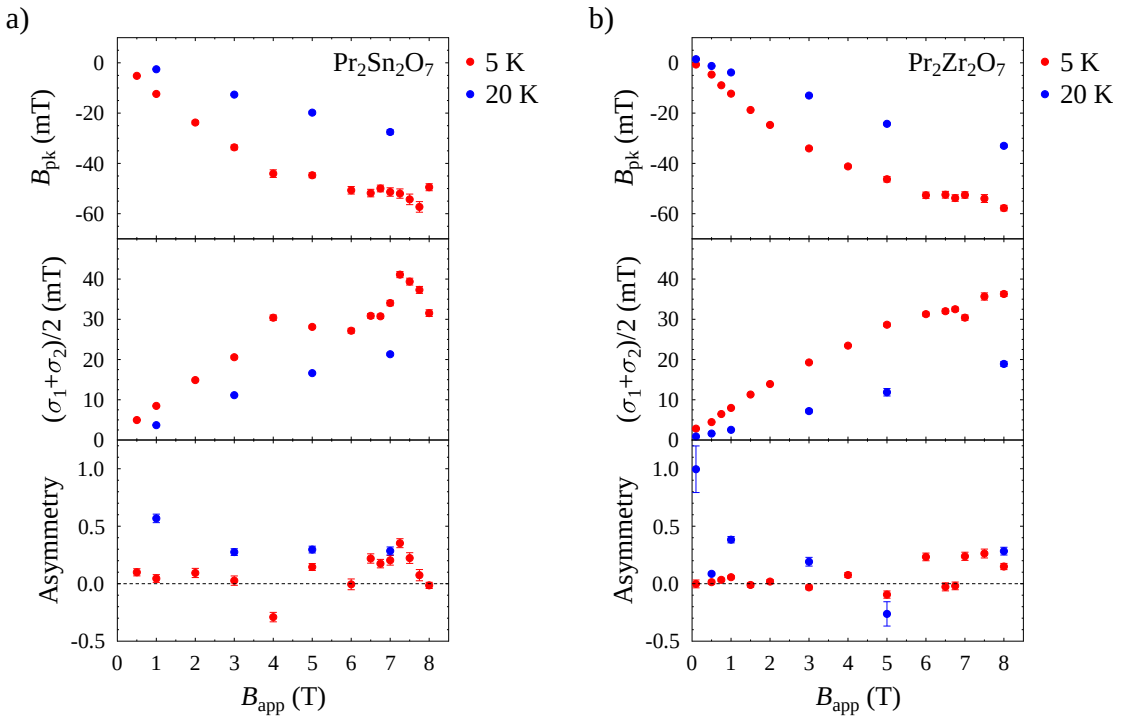

Figure 3.11: Field-dependence of the average field shift B_{pk}, calculated average field width $(\sigma_1+\sigma_2)/2$ and asymmetry parameter from fits of a) $Pr_2Sn_2O_7$ and b) $Pr_2Zr_2O_7$ at 5 K (red cirles) and 20 K (blue circles). The fitting function is described by Eq. 3.6.

and applied field and its magnitude is given by

$$\begin{aligned} |\mathbf{B}_{\mathrm{tot}}| &= \sqrt{(B_{\mathrm{app}} + B^{\parallel}_{\mathrm{loc}})^2 + (B^{\perp}_{\mathrm{loc}})^2} \\ &= B_{\mathrm{app}} \left[\left(1 + \frac{B^{\parallel}_{\mathrm{loc}}}{B_{\mathrm{app}}} \right)^2 + \left(\frac{B^{\perp}_{\mathrm{loc}}}{B_{\mathrm{app}}} \right)^2 \right]^{\frac{1}{2}} \\ &= B_{\mathrm{app}} \left[1 + \frac{2B^{\parallel}_{\mathrm{loc}}}{B_{\mathrm{app}}} + \left(\frac{B^{\parallel}_{\mathrm{loc}}}{B_{\mathrm{app}}} \right)^2 + \left(\frac{B^{\perp}_{\mathrm{loc}}}{B_{\mathrm{app}}} \right)^2 \right]^{\frac{1}{2}}, \end{aligned} \tag{3.7}$$

where $B^{\parallel}_{\mathrm{loc}}$ and $B^{\perp}_{\mathrm{loc}}$ are the parallel and perpendicular components of the local internal

field with respect to B_{app}. A series expansion gives

$$\begin{aligned} |\mathbf{B}_{\text{tot}}| &\approx B_{\text{app}} \left[1 + \frac{1}{2} \left(\frac{2B_{\text{loc}}^{\parallel}}{B_{\text{app}}} + \left(\frac{B_{\text{loc}}^{\parallel}}{B_{\text{app}}} \right)^2 + \left(\frac{B_{\text{loc}}^{\perp}}{B_{\text{app}}} \right)^2 \right) + ... \right] \\ &\approx B_{\text{app}} + B_{\text{loc}}^{\parallel} + \frac{{B_{\text{loc}}^{\parallel}}^2}{B_{\text{app}}} + \frac{{B_{\text{loc}}^{\perp}}^2}{B_{\text{app}}} + ... \end{aligned} \tag{3.8}$$

which for $B_{\text{app}} \gg B_{\text{loc}}$ gives $|\mathbf{B}_{\text{tot}}| \approx B_{\text{app}} + B_{\text{loc}}^{\parallel}$. Thus we see that the field shift B is a measurement of the parallel component of the local field. With the moments aligned parallel to B_{app}, any muons close to the dipoles along a direction parallel to the applied field would detect a positive contribution to the total field. Those lying in a direction perpendicular to B_{app} would detect a negative shift. This is illustrated by the schematic in Fig. 3.10(b) for a simple ferromagnet. Therefore, a negative B_{pk} indicates that most of the muon sites experience a dipolar field that has a component antiparallel to B_{app}. Due to the spin ice ground state and multiplicity of crystallographically, but not magnetically equivalent, muon sites (DFT calculations indicate 96 equivalent muon implantation sites per conventional unit cell), we expect a range of $B_{\text{loc}}^{\parallel}$ and hence a broad peak in field distribution, as observed.

We expect B_{pk} to scale with the average magnetisation along B_{app}, and hence exhibit the same behaviour as the measured low-field magnetisation shown in Fig. 3.12. These measurements show a linear trend at 20 K which becomes non-linear on cooling to 2 K (see Fig. 3.12a-b). Moreover, neither compound reaches saturation in fields of up to 7 T. In fact, pulsed-field measurements of a single crystal of $Pr_2Sn_2O_7$ (see Fig. 3.13) carried out using the technique described in section. 2.2.2 indicated that saturation would require an applied field of well over 40 T, which is beyond the scope of what is currently available at NKMFL. All of these measurements are consistent with the behaviour of B_{pk} in the μSR data.

Powder averaging may account for some of the broadening in $Pr_2Zr_2O_7$, although

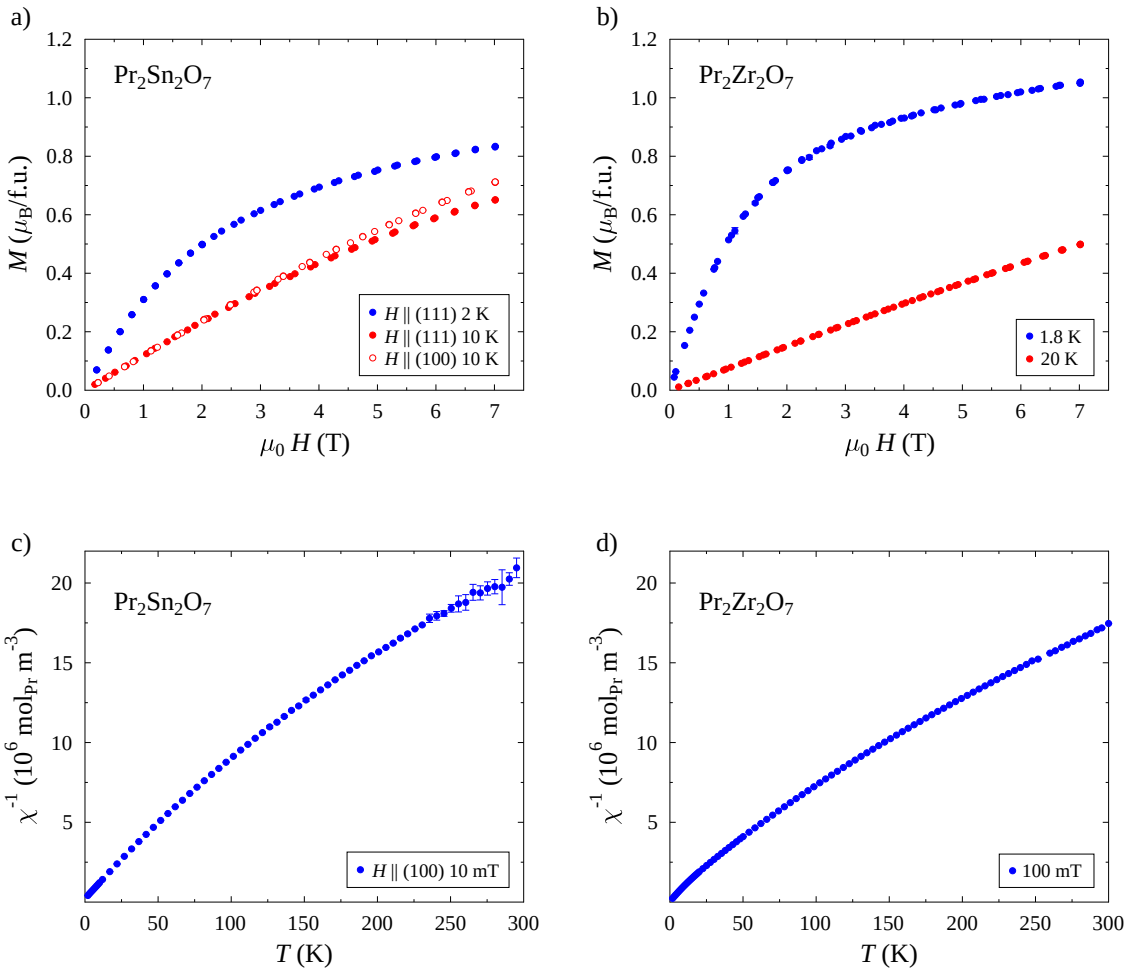

Figure 3.12: Low-field magnetisation (per formula unit) of a) single crystal $Pr_2Sn_2O_7$ in an applied field $H \parallel$ (111) at 2 K (filled blue circles), and at 10 K with $H \parallel$ (111) (filled red circles) and $H \parallel$ (100) (empty red circles). b) Magnetisation of polycrystalline $Pr_2Zr_2O_7$ at 1.8 K (blue circles) and 20 K (red circles). Inverse DC susceptibility of c) $Pr_2Sn_2O_7$ in a field of 10 mT applied parallel to (100) and d) $Pr_2Zr_2O_7$ in 100 mT.

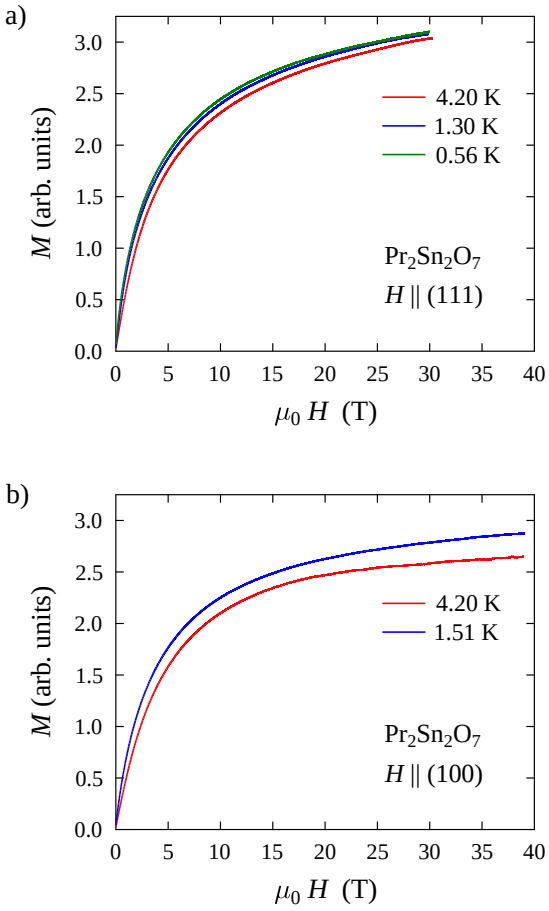

Figure 3.13: Magnetisation of single crystal $Pr_2Sn_2O_7$ measured in pulsed magnetic fields applied parallel to a) the (100) and b) the (111) crystallographic directions. The saturation field exceeds those available at the NKMFL.

the observation that the field width is slightly higher in single crystal $Pr_2Sn_2O_7$ suggests that the majority broadening comes from other effects, such as the Ising-like nature of the spins mentioned previously, as well and the fact that each muon is coupled to several Pr^{3+} moments. Due to the novelty of the instrument, one of the difficulties in interpreting these data is that there has been little published work to date for comparison, and so it would be useful to repeat these measurements on another system such as a simple ferromagnet. A detailed understanding of the instrument response is crucial for differentiating between a true sample response and an instrumental artefact. For example, the focussing of the muon beam as a function of field can lead to a change of beam spot size as field increases and hence a different ratio of sample to background. Furthermore, in high field there may be issues relating to the demagnetising fields from the sample residing in the silver sample holder which can cause additional relaxation, thus it is important to have a large total sample area to minimise these effects. In the previous section I have demonstrated how DFT calculations were successful in identifying the muon implantation site in these pyrochlore oxides. Our next step would be to calculate the corresponding internal dipolar fields, taking in account the muon-induced distortion, to compare with these muon measurements and clarify this interpretation of the dipolar fields.

Chapter 4

Muon States in Classical Spin Ice

4.1 Introduction

Spin ice is the name given to a family of ferromagnetic pyrochlores whose spins exhibit a highly degenerate and short-range ordered ground state down to zero temperature. Although there has been an extensive search for new spin ices, very few have been found to date, including the titanates $A_2Ti_2O_7$ [1] and stannates $A_2Sn_2O_7$ [69] ($A =$ Ho, Dy). Their frustration results from the interplay between crystal fields, magnetic exchange and dipolar interactions, which produce two key effects. Firstly, a strong single-ion anisotropy is produced by the local crystal field (CF) at the rare-earth sites that occupy the corners of the pyrochlores, which constrains the Ho^{3+} and Dy^{3+} ions to lie along the local $\langle 111 \rangle$ axes. Secondly, an effective ferromagnetic coupling arises from long-range dipolar interactions that dominate over antiferromagnetic nearest-neighbour exchange. These mechanisms are well described by the dipolar spin-ice model [70, 71] and the result is a '2-in, 2-out' spin configuration setting in at $T < 1\,\mathrm{K}$ that is analogous to the proton arrangement in water ice.

There have been extensive neutron scattering experiments down to 50 mK to determine the spin-spin correlations in the frozen regime (it is characterised by extremely

short correlation lengths that are comparable to the size of the tetrahedra) [71, 72, 73], as well as magnetisation studies that map out the field-dependent behaviour along the three cubic symmetry directions [74, 75, 76], all of which agree well with the dipolar spin ice model. Spin ice does not involve a fixed phase transition, but rather a continuous slowing down of spin fluctuations via a two-stage freezing process. The ground state of Ho^{3+} and Dy^{3+} is known to be an almost pure CF doublet which is separated from the first excited state by $> 200\,\mathrm{K}$ in zero field [77, 78, 79, 80, 81]. Take a single tetrahedra; there exists a range of possible spin configurations each with a certain energy cost, including a 'three-in, three-out', all-in/all-out or the familiar 'two-in, two-out' arrangement. At very high T, a whole range of CF levels are accessible and the system exhibits a combination of many different spin configurations. Upon cooling, the development of energy barriers limit the possible CF level transitions and spin arrangements. Just above $\approx 16\,\mathrm{K}$ the system exhibits thermal spin relaxation involving transitions to/from the lowest lying excited doublet. As it cools, it crosses into a quantum tunnelling relaxation regime (the slow-fluctuation regime), in which the system tunnels between two degenerate states in the ground state doublet. At these temperatures, the system is populated by a finite density of magnetic monopoles in which some spins are arranged into a 'three-in, one-out' (and vice versa) configuration. The excitations persist down to $\approx 1\,\mathrm{K}$ below which the spins settle into a frozen groundstate [77, 78, 82]. Note that in regime most tetrahedra occupy the 'two-in, two-out' configuration, although there may be some tetrahedra where the local spin ice rules are broken. The key difference is that the spins are now frozen out into what is essentially a short-range ordered ground state, as observed in the time scale of most measurement techniques. The spin ice state can be disrupted either by heating, or by applying an external magnetic field to induce individual spin flips.

Any substantial spin dynamics below 1 K have been mostly discounted with neutron scattering measurements down to 50 mK by Ehlers *et al.* [82] (although their

neutron spin echo measurements on $Ho_2Ti_2O_7$ do suggest that a small proportion of spins remain dynamic at frequencies that lie out of the experimental time window at $> 10^{12}$ Hz) and with bulk measurements below ~ 7 K [83, 84]. However, this only rules out dynamics within the time domains of neutron and ac-susceptibility measurements, which have characteristic times of 10^{-9}–10^{-14} s and 10^{0}–10^{-4} s, respectively. μSR offers another time scale that bridges the gap between the two techniques, although for $Ho_2Ti_2O_7$ there have been some contrasting findings. A study by Harris *et al.* on a single crystal of $Ho_2Ti_2O_7$ showed an almost identical asymmetry spectra in ZF at 4 K and 40 mK; that is, a loss of $\sim 1/3$ of the $t = 0$ asymmetry to the instrumental dead time, which the authors attribute to a very high, mostly static field of the Ho^{3+} moments, and an exponential decay in long-time asymmetry, which suggests some weak dynamics that persist into the spin-ice regime [85]. In contrast, a later study by Dunsiger *et al.* on similar single crystals reported a complete depolarisation of the muon beam at early times in a weak longitudinal field (3 mT) at low T, and this was attributed to rapid Ho^{3+} spin fluctuations rather than static local fields [86].

In this section I will present a μSR study on the dynamic spin processes in $Ho_2Ti_2O_7$ that has been motivated by another μSR study on polycrystalline $Dy_2Ti_2O_7$ by Lago and co-workers [79]. In agreement with other work, their data show that at high T ($T > 70$ K) in a small LF of 5 mT (used to decouple the nuclear moments without perturbing the electronic spins) there is a fast relaxation that increases upon cooling. This corresponds to the slowing down of thermally-activated fluctuations until the beam is almost completely depolarised within $t < 1\,\mu$s at $T \approx 60$ K. Interestingly, the $t = 0$ asymmetry recovers again, but to 1/3 of its original value (as measured at high T) when further cooled below 40 K and the observed relaxation rate is seen to decrease with T before levelling off at 12 K. The authors interpret this as a combination of the slowing down of the electronic fluctuations and the development of a local dipolar field, which is static in the μSR time window [79]. The

observed relaxation, which is not exponential in form, is assumed to correspond to a relaxing '1/3-tail' of a Kubo-Toyabe-like function in which only the LF components are resolved (the static transverse component being too large and thus lost in the instrumental dead time). Moreover, the study reveals some electronic fluctuations with a characteristic time of $\sim 10^{-6}$ s that persist well into the spin-ice regime. This is attributed to a hyperfine coupling with the Dy nuclear moments, whose thermal fluctuations at low T induces a slight 'wobbling of the electronic spin' about the $\langle 111 \rangle$ axes. The purpose of the experiment described in this chapter was to examine whether similar behaviour is observed for $Ho_2Ti_2O_7$ for which the rare earth ion is a non-Kramers ion (rather than a Kramers as is the case for $Dy_2Ti_2O_7$).

4.2 Experimental methods

The μSR experiments reported here were performed by myself, T. Lancaster, F. Lang and S. J. Blundell. Measurements were carried out on the GPS and LTF spectrometers at the Paul Scherrer Institute, Switzerland. All data analysis was performed by myself. The sample was prepared by D. Prabhakaran. A single crystal was grown using the floating zone technique and the resulting single crystal rod was sliced into thin discs. For the LTF measurements, two discs were fixed onto a silver backing plate with a small amount of vacuum grease and covered with silver foil. For the GPS experiment a single disc was fixed directly to a fly-past holder using kevlar tape to minimise background. Crystal field calculations were performed by A. T. Boothroyd.

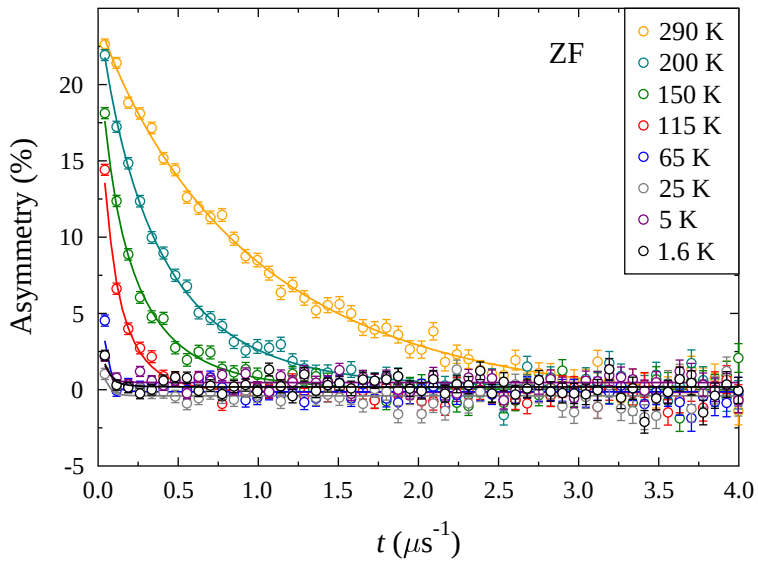

Figure 4.1: Example μSR spectra of $Ho_2Ti_2O_7$ in zero field. Fits are to a stretched exponential described by Eq. 4.1. As the system is cooled, the relaxation increases with more asymmetry being lost in the instrumental deadtime.

4.3 The Experiment

4.3.1 Observations

The ZF data show a relaxation that increases on cooling as expected (see Fig. 4.1), which signals a slowing down of spin fluctuations from room temperature down to the spin-ice ground state. On cooling, full beam polarisation is lost at a similar temperature ($\approx 50\,\mathrm{K}$) to $Dy_2Ti_2O_7$. However, unlike that of the Dy compound, the initial asymmetry does not recover upon further cooling but remains flat down to base temperature. Note that the LTF data ($T < 1\,\mathrm{K}$) include an extra, non-relaxing term from background contributions which results in a non-zero baseline (see Fig. 4.2).

The data are fit to a power exponential function;

$$A(t) = A_{\mathrm{rel}}\exp(-\lambda t)^{\beta} + A_{\mathrm{bg}}, \tag{4.1}$$

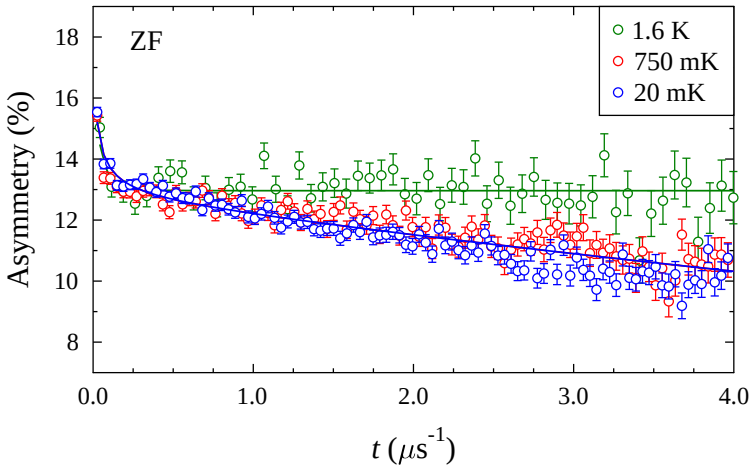

Figure 4.2: Example ZF spectra in the spin ice regime at 750 mK and 20 mK (LTF data). GPS data measured at 1.6 K (green circles) are shown with an added LTF baseline of 12.8% for direct comparison. Fits are to Eq. 4.1 (see text).

where $A_{\rm rel}$ is the initial relaxing asymmetry and $A_{\rm bg}$ is the background term due to a fraction of muons that stop in the sample surroundings. A more accurate estimate of the relaxation rate (which would have otherwise been affected by the large missing fraction) was achieved by fixing the total initial asymmetry at its maximum value. For the high T points (GPS data), fitting the spectra at 290 K gave $A_{\rm rel} + A_{\rm bg} = 25.2\%$, which was kept fixed for all subsequent fits. Note that for the GPS data, there is almost no baseline (as the experiment could be run in flypast mode) and all of the polarisation is lost in the electronic dead time upon cooling, in agreement with previous studies of $Dy_2Ti_2O_7$ at high T [79] and $Ho_2Ti_2O_7$ [86]. At low T (LTF data), the total initial asymmetry was fixed at 26.9%, which was the fitted value in a LF of 2.5 T at 750 mK (i.e. when the full asymmetry was recovered). For these data, the background term included a weakly relaxing exponential $A_{\rm bg}e^{\lambda_{\rm bg}}$ to account for the higher silver background from the cryostat tail and sample holder, with fixed values $A_{\rm bg} = 12.8(1)\%$ and $\lambda_{\rm bg} = 0.0543(9)$ (averaged from all low-T fits).

The thermal behaviour of the relaxation rate λ and the exponent β is shown in Fig. 4.5 (note the log scale). At high T, β is close to 0.9 and upon cooling to 50 K,

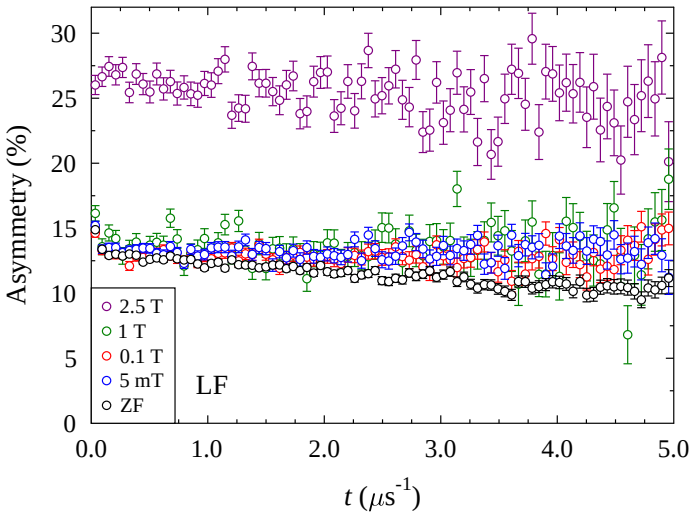

Figure 4.3: Example μSR spectra of $Ho_2Ti_2O_7$ in longitudinal fields measured at 750 mK on the LTF spectrometer. A field of more than 1 T is required to recover the full asymmetry.

it decreases steadily to 0.63. Over the same T range, λ increases more rapidly from $\sim 1\,\mu s^{-1}$ to $\sim 100\,\mu s^{-1}$. The data become difficult to fit at $T \leq 50\,K$ due to the rapid muon depolarisation that occurs at $t \ll 1\,\mu s$, hence λ appears to flatten out with large error bars (on a linear scale). A LF of up to 2.5 T was applied at 750 mK (see Fig. 4.3) and the sample was also measured in a TF of 50 mK at $5 < T < 280\,K$ (see Fig. 4.4). At high T, we observe clear oscillations from the applied transverse field, with significant damping from internal spin dynamics. The relaxation increases upon cooling until the TF signal essentially disappears at $\approx 5\,K$. At these temperatures the muons are strongly coupled to the local moments which have effectively frozen in the time scale of the experiment. This is consistent with our ZF observations and in contrast to the findings by Bramwell *et al.* who observed a clear TF signal down to 100 mK [87]. In the present data, one could argue that there are still some weak oscillations visible at 5 K, although we attribute this to a small fraction of muons stopping in the silver prongs of the sample holder. Thus the data suggest that any previously observed oscillations in spin ice were likely due to stray muons stopping in

silver cryostat or sample holder and not the sample itself.

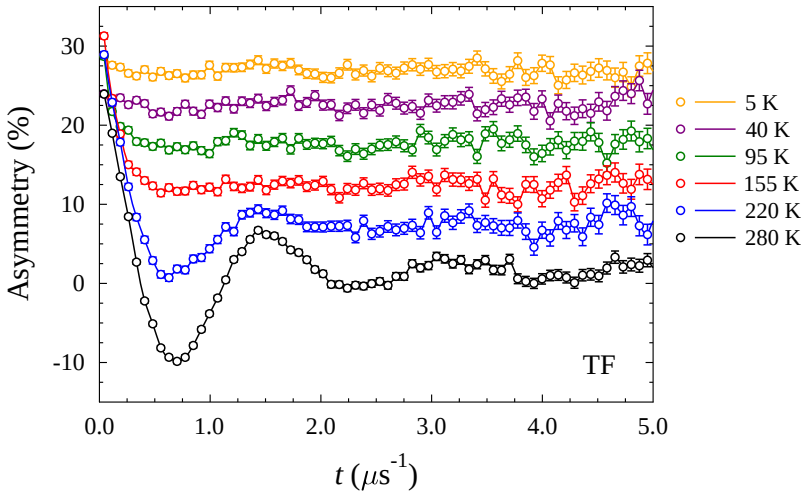

Figure 4.4: Muon asymmetry in transverse applied field of 5 mT measured on the GPS spectrometer. Data are offset for clarity. Lines are guide to the eye only.

4.3.2 Discussion

The most apparent difference between this and the previously measured $Dy_2Ti_2O_7$ is that there is no recovery of the $t = 0$ asymmetry upon further cooling, which rules out any quasi-static spin dynamics within the time frame of the experiment. The only dynamics observed are too fast to be measured directly and thus manifest in the missing asymmetry at early times. The temperature dependence of β suggests that there is a range of relaxation rates probed by the muons, for example due to a range of implantation sites that are crystallographically but not magnetically equivalent, as in the case of the Pr-based pyrochlores. Fig. 4.2 shows ZF spectra measured at 750 mK and 20 mK on the LTF spectrometer, and GPS spectra measured at 1.6 K (an LTF baseline was added to the latter for direct comparison). A noticeable increase in relaxation is observed in the LTF data, although it is unclear whether this behaviour is intrinsic to sample or purely an artefact of the instrument. The relaxation may have reappeared as a result of cooling into the frozen regime, although there are no

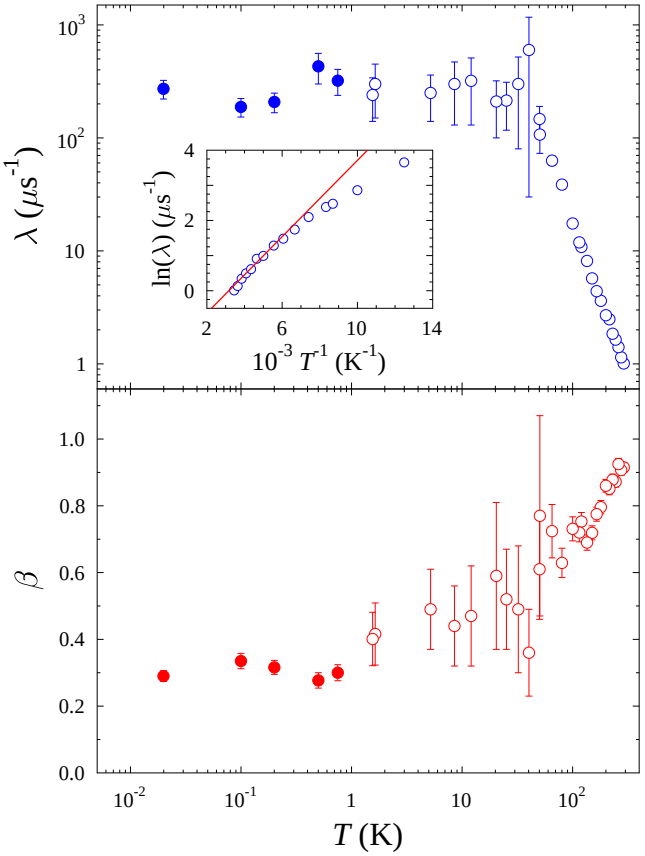

Figure 4.5: Temperature dependence of exponent β and relaxation rate λ from fits of ZF μSR. White circles, GPS data; filled circles, LTF data. Inset shows high-T behaviour of λ. The linear fit gives a measure of the activation energy (see text).

intermediate temperature measurements to confirm this. Alternatively, given that the relaxation is larger than expected from regular silver background (an exponential background term was included in the fitting function to account for this) and that the Ho^{3+} moments are relatively large ($10.6\mu_B$), the relaxation is likely to be from stray fields picked up by muons in the sample holder or cryostat walls. The GPS measurements would have been less susceptible to these effects as they were performed on a 'fly-past' holder.

For high T, the thermally activated fluctuation regime, the relaxation rate is fit to an exponential $\lambda \propto e^{E_a/k_B T}$ (see Fig. 4.5 inset) in which E_a/k_B corresponds to the

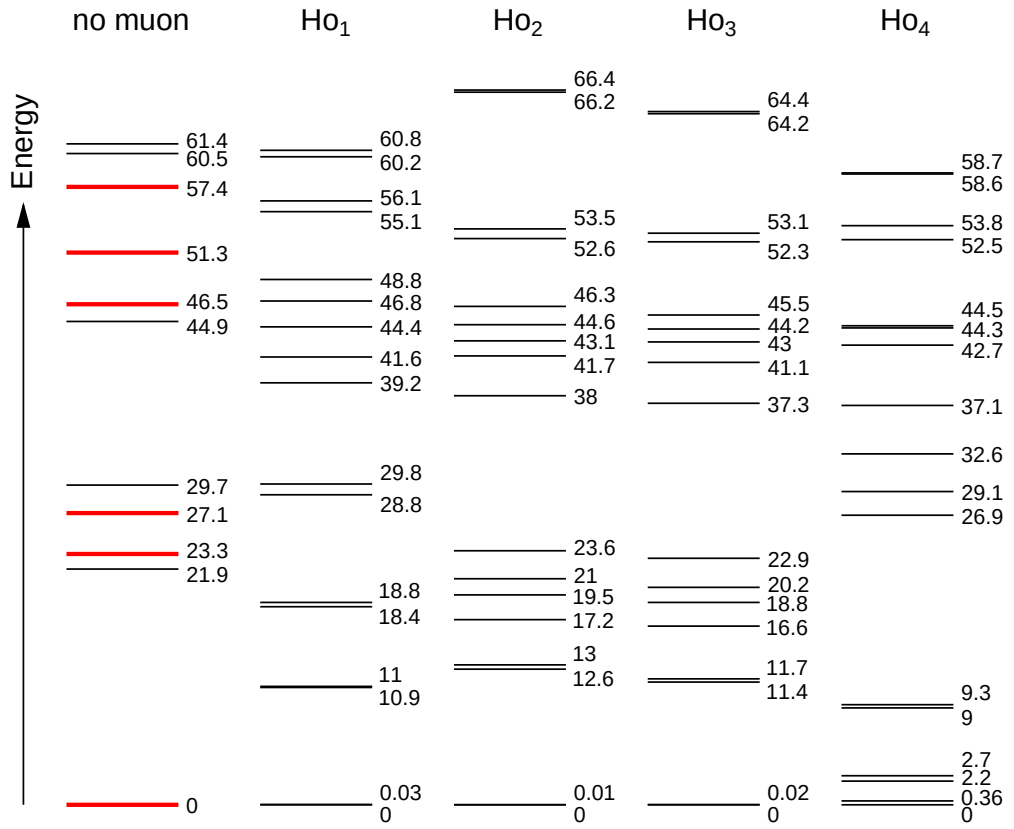

Figure 4.6: Calculated CF levels of Ho^{3+} in $Ho_2Ti_2O_7$ with and without muon-induced distortion (calculated using DFT, see section 3.3.4). These crystal field states determine the size and anisotropy of the Ho^{3+} magnetic moment. Bold red lines indicate doublets, plain black lines are singlets.

energy gap between the ground state and first excited CF level. This gave an activation energy of $E_a/k_B = 540(10)\,\mathrm{K}$ $(46.6(9)\,\mathrm{meV})$ for $T > 180\,\mathrm{K}$. A deviation from the linear trend shown for $\ln\lambda$ vs T^{-1} for decreasing T signals a change in relaxation channels as the higher energy levels become inaccessible with cooling. Note that E_a is the energy of the crystal field level that mediates the spin relaxation process. These measurements show that at high T, the energies are of the order $\sim 10\,\mathrm{meV}$, that is, much larger that the measured values of λ, which correspond to a Zeeman energies of $\leq 1\,\mu\mathrm{eV}$. This implies that relaxation mechanism is likely some kind of Orbach process [88] in which the small energy to flip the muon spin (and relax it) stems from the difference between the larger energies of two crystal field transitions. To compare

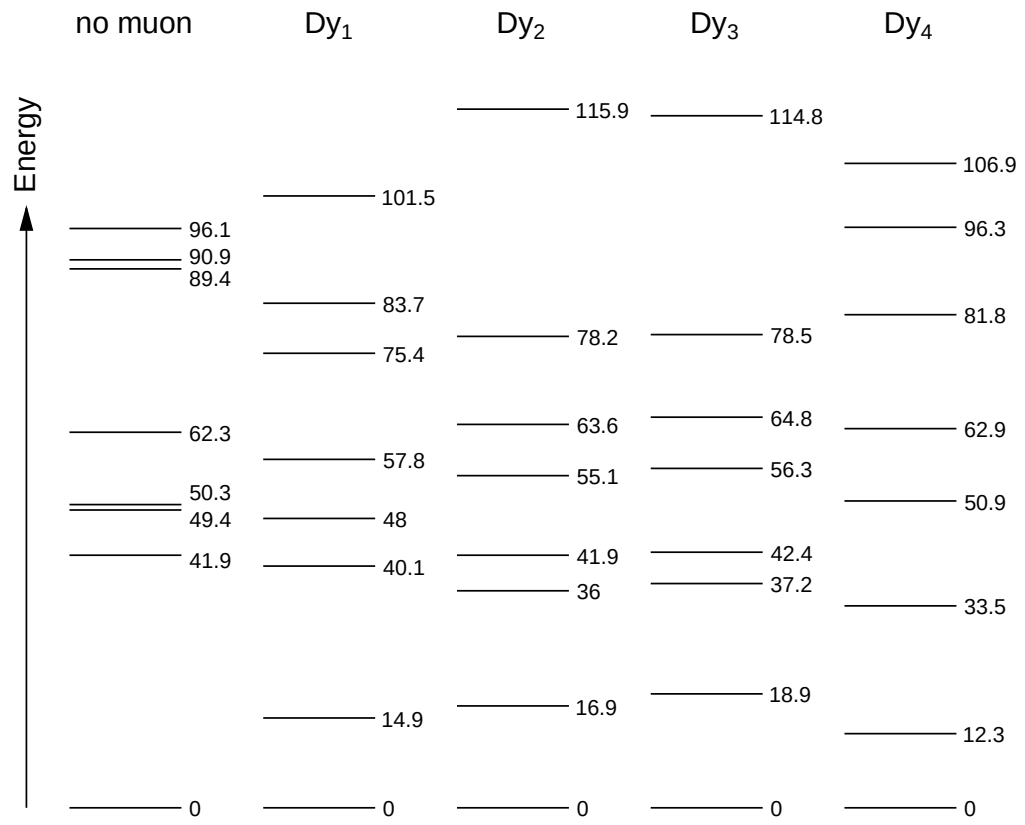

Figure 4.7: The calculated CF levels of Dy^{3+} in $Dy_2Ti_2O_7$ with and without muon-induced distortion as determined by DFT.

these with theoretically calculated CF levels, one must also consider any possible muon perturbations, particularly as the groundstate in Ho^{3+} is a non-Kramers doublet and therefore highly susceptible to these effects. Thus we employ the usual DFT method described in section 3.3.4 to identify the muon stopping sites. The muon site in this case is found to be essentially identical to that calculated for $Pr_2Sn_2O_7$, and consequently produces a similar distortion of the crystal lattice due to the muon electric field. As in the case of the Pr-based pyrochlore oxides, this results in an alteration of the CF levels in the neighbouring Ho ions. These have been calculated for the four nearest Ho^{3+} ions and are shown in Fig. 4.6. The calculations were also performed for the case of $Dy_2Ti_2O_7$ and are shown in Fig. 4.7. In both compounds, the effective activation energy (the energy difference between the first excited state and the ground

state) of all four nearest neighbour ions decreased significantly with the introduction of a muon. In the case of Ho^{3+} the energy gap was reduced from 21.9 meV, which was already under half of that observed in μSR measurements, to as little as ≈ 0.1 meV due to the splitting of the ground state doublet. In Dy^{3+}, the difference is less pronounced as the energy gap is reduced from 41.9 meV to 12.3–18.9 mV for various ions. To compare with μSR, the data from Lago *et al.* in Ref. [79] were reanalysed using Eq. 4.1 for consistency (as in the Ho case, the initial total asymmetry was fixed at its maximum value of 28.23 %, as measured at high T) and the results are shown in Fig. 4.8. Fitting $\ln\lambda$ vs T^{-1} at $T > 180$ K (Fig. 4.8 inset) gave $E_a/k_B = 46.5(1.7)$ meV. (Note that the original paper gave a value of 18.1 meV (210 K) although it was later found to contain an error in $\ln\lambda$).

One complication arises in that each muon is coupled to a range of ions, whose CF levels span a range of energy gaps as demonstrated by the DFT and subsequent CF calculations. However, We see that in the case of Dy^{3+}, the measured activation energy is in agreement with that calculated for the unperturbed case, which implies that the muons are dominated by ions that are situated further away from the implantation site, and whose crystal environments are largely unaffected by the muon electric field. In contrast, the observed activation energy in the case of Ho^{3+} is of a similar scale to that expected from Dy^{3+}, but almost twice as that calculated for unperturbed Ho^{3+}. This may simply highlight a high-T bias in these measurements, particularly as the fits for the activation energy assumes a 2-level system. In reality this is true only at low T, and as T increases the systems gains access to additional excited states which results in the curvature that is observed in the graph of $\ln\lambda$ against T^{-1}. Therefore the reason we do not observe the smaller energy level splittings is likely due to a combination of the large far away spins dominating the signal, and the fact that these measurements are insensitive to smaller scale splittings. To summarise, previous studies have shown how the low-temperature regime of spin ice

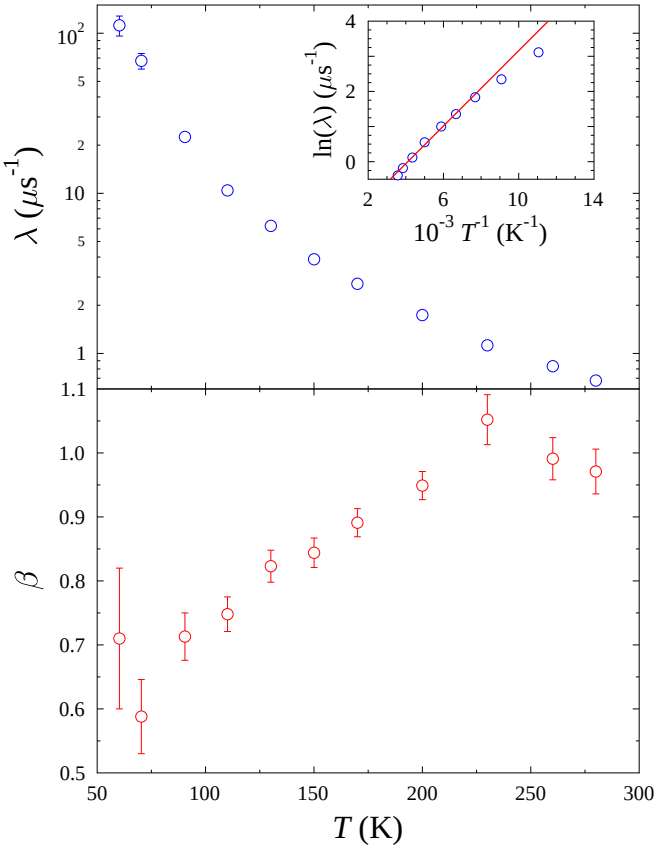

Figure 4.8: Temperature dependence of exponent β and relaxation rate λ in $Dy_2Ti_2O_7$. Data are refitted from ZF measurements in Ref. [79]. Inset shows high-T behaviour of λ. The linear fit gives a measure of the activation energy (see text).

is dominated by monopole physics with an energy barrier of the order $\approx 1\,\mathrm{K}$ (5.64 K for $Dy_2Ti_2O_7$ and 8.52 K for $Ho_2Ti_2O_7$ according to Debye-Huckel theory [89]). In this study we see that as the temperature increases to $T > 40\,\mathrm{K}$, the system gains access to the higher crystal field states, thus altering the size and anisotropy of the Ho^{3+}/Dy^{3+} magnetic moments. A subject for future work would be to obtain a full quantitative agreement between the crystal-field energy levels and the observed $\lambda(T)$ and β(T), however this may involve a more detailed calculation of all the excited state crystal field functions and allowed transitions between them, which is beyond the scope of this thesis.

4.4 Conclusion

In conclusion, I have demonstrated that unlike $Dy_2Ti_2O_7$, there appears to be no residual electronic fluctuations in the frozen regime of $Ho_2Ti_2O_7$ as measured in the time frame of μSR. I have also presented a first attempt to systematically relate the ZF relaxation rate in both compounds to the calculated crystal field levels after muon implantation, which through DFT calculations are shown to be altered in a similar way to that seen in previous pyrochlore oxides due to the muon electric field. The data show an effective activation energy that increases with temperature, which demonstrates that the system can access more excited crystal field levels with higher T. One surprising result is that the relaxation of the muons is not dominated by the nearest neighbour Ho^{3+} and Dy^{3+} ions, but by those further away which experience less perturbation from the implanted muon. This may be due to the large moments of Ho^{3+}/Dy^{3+} which allows the muons to couple strongly to those further away and therefore allowing those unaffected by the muon implantation to dominate the signal. Lastly, we see that the nuclear spin mechanism that was so dominant in the Pr pyrochlores does not appear to operate in the spin ices, even for the case of the non-Kramers ion Ho^{3+}.

Chapter 5

Fe-based Superconductors

5.1 Introduction

In 1911, H. R. Onnes was able to show how electrical resistance in pure mercury disappeared completely below 4.2 K thus demonstrating superconductivity for the first time. Two decades later, W. Meissner and R. Ochsenfeld introduced another intrinsic property of the superconducting state called the Meissner effect, in which a material will expel any external magnetic field when cooled below T_c [90, 91]. Some superconductors (type-I) are found to exhibit the complete Meissner effect below a critical field, above which the superconducting state is destroyed. Another type of superconductor (type-II) was experientially identified by L.V. Shubnikov in 1936 [92, 93] when he observed an intermediate phase, the 'mixed state', characterised by two different critical fields H_{c1} and H_{c2}. These materials differ to type-I superconductors in that there is only a partial Meissner effect in the mixed state and superconductivity is gradually destroyed as the strength of the external field is increased.

A microscopic theory for superconductivity was thought to have been solved in 1957 by J. Bardeen, L. N. Cooper and J. R. Schrieffer (BCS) [94], who proposed that electrons could overcome their mutual electrostatic repulsion and form pairs of

opposite spin and momentum, called Cooper pairs, via electron-phonon interactions. Crucially, this pairing leads to the formation of an energy gap with the electrons condensing to a single coherent ground state that is capable of carrying current without loss of energy.

BCS was widely accepted as the general theory of superconductivity until another major breakthrough in 1986 by J. G. Bednorz and K. A. Müller, who discovered a novel superconductor in $La_{2-x}Ba_xCuO_4$ [95]. This triggered a renewed surge of interest in the field and led to the discovery of an entirely new class of unconventional high-T_c superconductors known as the 'cuprates'. They were unconventional in that their behaviour could not be described by the BCS model, with many of them having impressively high transition temperatures in excess of that predicted by conventional BCS theory (up to $\approx 30\,K$), such as in the case of a Hg-based ceramic with $T_c \approx 133\,K$ [96]. Although the superconducting mechanism was not fully understood, it was assumed that the presence of copper was essential to high-T_c superconductivity since the current was mediated by Cu-O planes in all of the recently identified compounds. However, another discovery by Takahashi *et al.* in 2008 dismissed this idea when he observed superconductivity in fluorine doped LaFeAsO with a T_c of $26\,K$ [3]. The presence of iron was surprising since ferromagnetism was considered destructive to superconductivity, and this ignited huge interest in a new series of Fe-based superconductors with critical temperatures of up to $55\,K$ [97]. These compounds show unique features that are leading to the development of new theories of superconductivity in close proximity to magnetism.

In this chapter, I shall first introduce a brief overview of Fe-based superconductors, including their general structure, properties and phase diagram. I shall then present a study of the superconducting properties of a recently discovered Fe-based superconductor $Sr_{0.3}(NH_2)_y(NH_3)_{1-y}Fe_2Se_2$, before moving on to describe the role of ammonia intercalation in the related compound $Li_x[(NH_2)_y(NH_3)_{1-y}]_zFe_2Se_2$ ($z = 1, 2$). Lastly,

I present a short μSR study on the properties of the '111' superconductor LiFeP.

5.2 Overview: Fe-based superconductors

The Fe-based superconductors consist of a layered structure, similar to that of the cuprates, in which superconductivity is mediated by layers of edge-sharing Fe-X tetrahedra, where X maybe be a pnictogen such as As, P, or chalcogen such as Se, Te (see Fig. 5.1). A key challenge has been to find ways of modifying the iron-containing layers to enhance superconductivity, with one way of achieving this being via intercalation. For example, the tetragonal phase of FeSe with layered structure is a superconductor with a relatively modest T_c of 9 K. However, intercalation can be used to enhance the transition temperature by a considerable degree. As a result, several families of Fe-based superconductors have been identified and are categorised based on their structural types. These include; the simple '111' systems, which contain no spacer layer (AFeX, A =Li, Na), the '122' family (AFe$_2X_2$, A =Ca, Sr, Ba, Eu, K) and the '111' family (AOFeX, A =La, Ce, Pr, Nd) [98], as well as other complex compounds such as $Sr_3Sc_2O_5Fe_2As_2$ [99].

A comparison of the generic phase diagrams for cuprates and Fe-based superconductors is shown in Fig. 5.2. In both cases, there is a transition to an antiferromagnetic (AF) phase below a temperature T_N at zero-doping, and superconductivity emerges only upon doping with holes or electrons. Other methods of inducing superconductivity include applying mechanical pressure [101] or, as described above, by modifying the crystal structure via isovalent chemical substitution (i.e. applying a chemical pressure) [102]. There are also some clear differences between the two types of compounds. Firstly, in their underdoped form, cuprates are Mott insulators whereas the Fe-based systems show poor-metallic behaviour. Both families undergo a magnetic transition at low temperature, although in the cuprates, the magnetic order

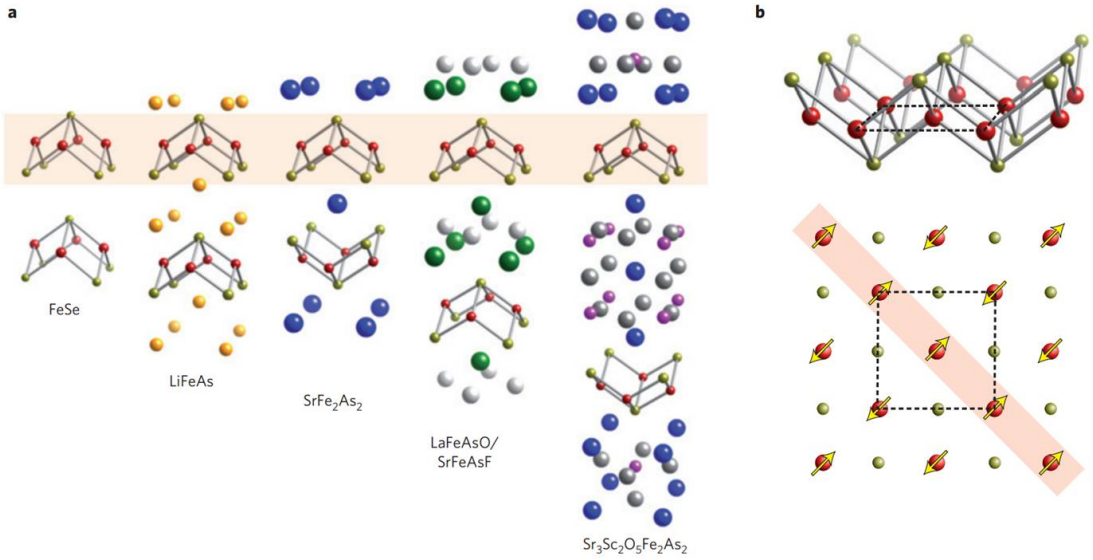

Figure 5.1: a) Crystallographic structures of the Fe-based superconductors. The universal iron layer responsible for superconductivity is shown in b) viewed in-plane (red speres are iron ions; gold spheres are pnictogen/chalcogen anions). An alternative view is also shown from above with the ordered antiferromegntic structure indicated by arrows. From Ref. [100].

is conventional AF, whereas the Fe-based compounds feature a stripe-like ordering [103] with alternating ferromagnetic and AF arrangements in adjacent layers (see Fig. 5.1b). In addition, the magnetic transition in the Fe-based compounds is often accompanied by a tetragonal to orthorhombic structural transition, although these transitions do not always occur simultaneously.

One important area of investigation is the pairing symmetry of the bound electron pairs. This refers to the symmetry of the superconducting gap, a measure of the energy required to break Cooper pairs, whose properties could offer insight into the underlying pairing mechanism. Although once thought to be incompatible, the close proximity of the AF and superconducting phases observed in all uncoventional systems has long suggested that magnetism could play a key role in high-T_c superconductivity. Current studies identify magnetic spin fluctuations as the driving mechanism, with d-wave pairing in the cuprates and primarily s-wave pairing in Fe-based materials [105, 106].

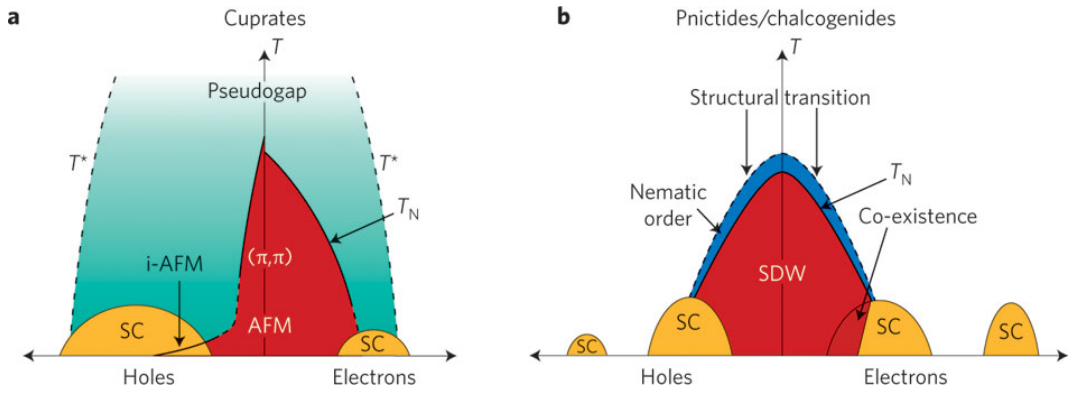

Figure 5.2: Generic phase diagrams for a) the cuprates and b) the Fe pnictides as a function of electron or hole doping (exact details/phases vary depending on compound). There is magnetic ordering in the parent compounds with superconductivity emerging via doping, and in the case of the pnictides also by applying pressure. Whilst most cuprates display conventional antiferromagnetism, many of the Fe pnictides show a stripe-like magnetic ordering [103] that is accompanied by a tetragonal to orthorhombic structural transition. Another noticeable difference is the presence of a pseudogap in the cuprates that is not common in the pnictides. Ref. [104].

Much of this research is driven by the desire to further increase critical temperatures and ultimately synthesise materials with room-temperature superconductivity. To this end, it is essential to identify the limiting factors in these systems. One fundamental measure of superconducting strength is the upper critical field H_{c2}, whose temperature dependence can provide a valuable insight into the origin of field–induced pair breaking, as well as a means to extract other significant parameters such as coherence length and penetration depth. In the rest of this chapter I shall present high-field and μSR studies on a range of recently discovered Fe-based superconductors and demonstrate how key parameters are affected via modifications of the crystal structure and intercalation species.

5.3 Superconductivity and structural disorder in $Sr_{0.3}(NH_2)_y(NH_3)_{1-y}Fe_2Se_2$

5.3.1 Introduction

Increasing the inter-layer separation in FeSe has been found to give rise to a dramatic effect on the superconducting transition temperature T_c. Studies show that pure FeSe ($T_c = 8.5\,K$ [107]) can be intercalated with alkali metal ions and ammonia [108, 109, 110] or other organic molecules [111, 108] to produce new superconductors with transition temperatures of up to around 45 K. Similar high–T_c behaviour can be induced using metal hydroxides as the spacer layer [112, 113, 114, 115]. This trend of increase in T_c with increasing layer separation does not continue indefinitely [111], and this effect can be rationalised through first-principle calculations [116]. However, one factor that has not been so closely examined is the effect of controlled structural disorder on T_c.

This section is based on work published in Ref. [117] as part of a collaborative effort. We have identified an intercalated FeSe compound $Sr_x(NH_2)_y(NH_3)_{1-y}Fe_2Se_2$ ($x = 0.3$, $0.2 \leq y \leq 0.6$) in which random stacking of well-defined layers results in a paracrystalline structure. Paracrystalline materials are defined as having short and medium range structural ordering in their lattice, but lacking long-range ordering in at least one direction. This compound belongs to a family of layered intercalates $A_x(NH_2)_y(NH_2)_{1-y}Fe_2Se_2$ (A = Li, Na, K, Rb, Cs, Ca, Sr, Ba, Eu and Yb), in which bulk superconductivity occurs in anti-PbO-type FeSe layers composed of edge-sharing $FeSe_4$ tetrahedra that are separated by metal ions, amide ions and ammonia molecules [109, 118, 110, 119]. Figure 5.3 shows the various structures and the conventional unit cell with $a = b \approx 3.8\,Å$ and $c = 16.5$–$17.4\,Å$. These compounds remain tetragonal down to low temperatures and do not exhibit orthorhombic dis-

tortion. Neutron scattering and X-ray diffraction measurements have revealed some structural differences related to the size of the cation used; when it is small ($A = \mathrm{Li}$), Fe ions in adjacent layers occupy the same primitive tetragonal sublattice [109], as shown in Fig.5.3(a). For larger cations ($A = \mathrm{K}, \mathrm{Rb}$), the arrangement of Fe and Se ions is unchanged, but the larger electropositive cations share the same sites as the amide and ammonia moieties in the body-centred position of the primitive Fe sublattice (see Fig. 5.3b). As I will describe in more detail in the following sections, the Sr case presents a scenario in which there is a random stacking of adjacent FeSe layers along the c-axis, which may be described as paracrystalline. In this case, there is long-range ordering within individual layers that occupy the a-b plane, and the structural disorder exists along the c-axis due to the random stacking arrangements of these layers. I shall demonstrate through SQUID magnetometry, pulsed magnetic fields and muon spin rotation (μSR) measurements that, despite this unusual structural disorder, superconductivity remains robust with a $T_c \approx 36\,\mathrm{K}$ that is significantly higher than that of the parent compound.

5.3.2 Experimental methods

Sample synthesis and characterisation, including powder x-ray diffraction and bulk susceptibility measurements, were performed by S. J. Cassidy, S. J. Sedlmaier, J. D. Wright and S. J. Clarke. In an argon filled glovebox, finely ground FeSe powder (1.970 g, 14.611 mmol) synthesised from the elements as described elsewhere [109] and pieces of strontium metal (0.640 g, 7.304 mmol, ALFA) were placed in a thick-walled glass Schlenk tube capable of withstanding an internal pressure of over 15 bar. The tube was evacuated and cooled to -78 °C with an isopropanol/dry ice cooling bath. Around 50 ml of liquid ammonia was condensed into the Schlenk tube and the Sr metal was dissolved in the liquid ammonia to produce a blue solution. The valve on the Schlenk tube was closed, isolating it from the line and the reaction mixture

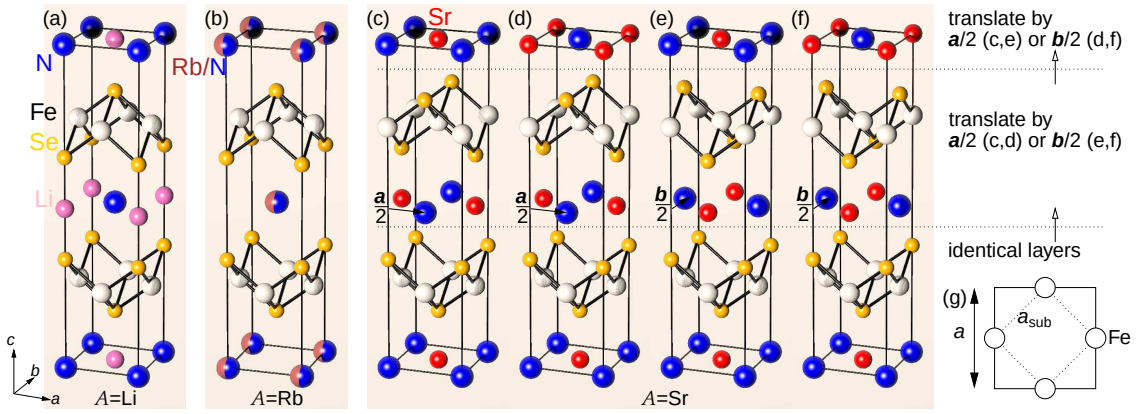

Figure 5.3: Crystal structure of the FeSe intercalates family in which the spacer layer consists of ammonia with (a) Li, (b) Rb, or (c)–(f) Sr atoms (hydrogen omitted for clarity). In the Li and Rb intercalates the Fe atoms (grey spheres) in adjacent layers occupy a primitive $a_{\rm sub} \times a_{\rm sub} \times c_{\rm sub}$ sublattice, where $c_{\rm sub} = c/2$ is the distance between adjacent Fe layers (~ 8.3 Å for the Li intercalate). In the Rb case, the metal ions and ammonia molecules share the same site with 50% occupancy (split pink/blue spheres). In the Sr case, the Fe sublattice is a body-centered tetragonal unit cell that is elongated by a factor of two in the c direction and the structure contains random stacking faults. The stacking faults are illustrated in Figures (c)–(f) as follows. The dotted lines indicate where the stacking faults occur, with the section below the lower dotted line being identical in all four diagrams. Above the lower dotted line, the Fe-Se units are translated relative to those in the lower layer by half a unit cell along either the a or b direction. At the upper dotted line, the same translation along a or b occurs again, so that with n dotted lines there would be 2^n possible configurations. With the two dotted lines shown, Figures (c)–(f) demonstrate the four possible stacking combinations when starting from an identical base layer. The position of the Fe sublattice relative to the unit cell in a single layer, as viewed along the c-axis is shown in (g).

was allowed to warm to room temperature and stirred for 24 h. After the reaction, it was recooled to −78 °C, allowing the valve to the line to be opened. The ammonia was evaporated off via a mercury-filled bubbler while letting the Schlenk tube slowly warm to room temperature. At the end of this process the Schlenk tube was placed under dynamic vacuum for 2 min and brought into the glovebox. The product was isolated as a very fine black powder. Samples were prepared using both normal and deuterated ammonia. The following measurements focus on the former, and involve two different samples from separate syntheses (note that the samples were synthesised under the same conditions and are therefore expected to exhibit the same physical properties). For clarity, I shall refer to them individually as sample *A* and sample *B*. Due to their air-sensitive nature, all samples were handled under an inert gas atmosphere at all times.

ZF, LF and TF μSR measurements were carried out by myself using the GPS spectrometer at PSI, and the MuSR spectromter at ISIS, RAL, with the assistance of S. J. Blundell J. D. Wright and T. Lancaster. The powdered samples were placed inside a Ag-foil packet ($\sim 12.5\,\mu$m foil thickness) under argon, crimped closed and mounted a silver backing plate. For the TF experiments, heamatite was placed on the backing plate to ensure any muons missing the sample did not contribute to the measured relaxation.

Pulsed magnetic field measurements, and relevant analysis, were carried out at the NKMFL by myself with the assistance of S. Ghannadzadeh and P. A. Goddard. Initially, the sample was prepared as a pressed pellet under argon atmosphere to maximise packing efficiency and hence improve the signal. To prevent oxidation, the sample was covered in degassed Apiezon grease before being transferred to a pre-wound sensor coil consisting 8 turns of 75 μm thick copper wire (~ 1 mm diameter) and quickly mounted inside the He^3 jacket. However, no superconducting transitions were observed upon cooling in fields of up to 35 T, suggesting that the powder may

have been exposed to air during/after the pressing process, or reacted with the grease itself. The measurements were repeated with the powder mounted in an ampoule of 1 mm diameter (0.15 mm walls), again under argon, which was sealed with a layer of degassed Apiezon grease, teflon tape and GE varnish. A pick-up coil (10 turns, 25μm copper wire) was wound directly onto the ampoule.

5.3.3 Structural characterisation

The crystal structures of the products were analysed using synchrotron X-ray powder diffraction on beamline I11 at the Diamond Light Source, or beamline ID31 at the ESRF. Samples were sealed under an argon atmosphere within 0.5 mm diameter borosilicate glass capillaries. The diffractograms revealed a series of extremely sharp reflections that could all be indexed on a body centred tetragonal unit cell with lattice parameters $a_{\mathrm{sub}} = 2.7$ Å and $c = 17.4$ Å (see Fig. 5.4a). The intensities of these reflections were accounted for by the model shown in Fig. 5.4(b)–(c) in which the familiar square planar Fe nets found in all the iron selenide superconductors with Fe–Fe $= a_{\mathrm{sub}} \sim 2.7$ Å are related by the body centering translation. This model was also obtained using a charge flipping algorithm implemented within *Topas Academic* [120], and was consistent for all the samples investigated. However, it failed to account for regions of weak structured diffuse scattering as evident in Fig. 5.4(c).

An improved fit was found with a $a = b = \sqrt{2}a_{\mathrm{sub}}$ basal expansion of the tetragonal unit cell. In order to satisfy the coordination requirements of the ions (shown in Fig. 5.4f-g), the FeSe layers formed a random stacking arrangement along the c-axis in which adjacent layers were constrained to be translated relative to one another by $\boldsymbol{a}/2$ or $\boldsymbol{b}/2$. This captured the key features of the diffuse scattering seen in Fig. 5.4(d)–(e). The resultant interatomic distances and the coordination environments were chemically realistic with N–H...Se distances (3.7 Å) similar to those found in the analogous

Li/NH_3 intercalates. Note that some discrepancies remain in quantitatively modelling the intensity distribution in these parts of the diffraction pattern (decomposition of the samples in the electron bean ruled out transmission electron microscopy as a means to further explore the diffuse scattering). This description of the structure in which well-defined layers are stacked in a disordered manner may be described as paracrystalline [121].

The refinements produced a Sr:Fe ratio of 0.15:1 and an N:Fe ratio of 0.5:1, however the measurements conducted so far did not allow the N:H ratio to be determined with certainty. Thus we use the formula $Sr_{0.3}(NH_2)_y(NH_3)_{1-y}Fe_2Se_2$. Since the Sr/ammonia solution is reducing, the upper bound on y is 0.6 yielding an Fe oxidiation state of +2. An Fe oxidation state of +1.8 which is found for other iron selenide systems would require $y = 0.2$. In what follows we refer to the mixture of amide and ammonia moieties as NH_z ($2.4 < z < 2.8$).

5.3.4 Disorder in Se

From the foregoing work we arrive at one key difference between this intercalate and the previously described intercalates containing alkali or alkaline earth metal ions and ammonia molecules/amide ions. That is, the square arrangement of iron atoms in one layer is related to that in the neighbouring layers by a basal plane translation of half a unit cell in either the a or b direction, resulting in the $2.7 \times 2.7 \times 17.4\,\text{Å}^3$ body centered tetragonal arrangement of Fe atoms (see Fig. 5.3c–f). In contrast, the arrangement of adjacent Fe layers in all other iron-based superconductors are related by the $c/2$ lattice vector and thus describe a primitive $2.7 \times 2.7 \times c_{\text{sub}}$ sublattice. Figure 5.3(c)–(f) demonstrates how the nature of these translations, represented by dotted lines, result in a paracrystalline structure as follows: Consider starting from an identical base layer (the region below the first dotted line), in which the Fe, Se

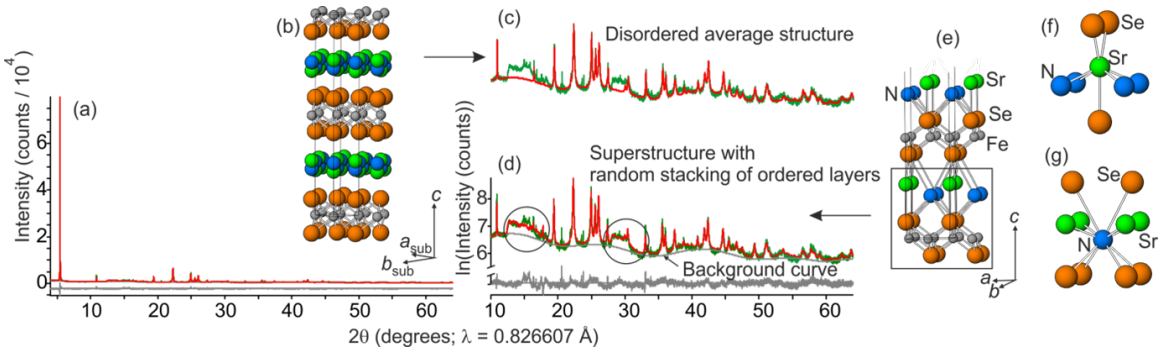

Figure 5.4: Refinements against I11 powder diffraction data showing experimental (green) and calculated (red line) patterns as well as the difference (gray line). The full pattern is shown in (a) with magnifications of the diffractogram showing calculations from two different models in (c) and (d) (magnifications are shown with the same horizontal scale as (a) but with a logarithmic intensity scale to emphasise the weak features in the data). The full pattern is dominated by sharp Bragg reflections which can be accounted for by the disordered average structure shown in (b) with space group *I4/mmm* with unit cell $a_{\mathrm{sub}} \times a_{\mathrm{sub}} \times c$. This model assumes full occupancy of the Fe sites that describe a body centered tetragonal unit lattice, but 50% occupancy of the selenide sites and also partial occupancy of the N and Sr sites. However it fails to account for regions of diffuse scattering, as shown in (c). (d) shows an improved fit to the diffuse scattering (ringed) when using a model in which chemically realistic layers (boxed region in diagram (e)) with basal lattice parameters $a = b = \sqrt{2} \times a_{\mathrm{sub}}$ are translated by either $\boldsymbol{a}/2$ or $\boldsymbol{b}/2$ relative to their neighbours, as described in the text and Figure 5.3. Both fits employed the same background function. Hydrogen atoms attached to the nitrogen atoms were not modelled, but assumed to be directed towards the selenide ions as described in related systems [109]. (f) and (g) show the local coordination environments around the Sr and N, respectively.

and intercalated species occupy the same crystallographic sites as those found in the Li case. To construct the next layer, each atom must be translated by either $\boldsymbol{a}/2$ or $\boldsymbol{b}/2$. In each case the Fe sites are the same but the positions of the Se, ammonia and metal species change depending on the chosen direction. As the translation occurs along a randomly chosen direction with the addition of each layer, it follows that for n layers there would be 2^n possible configurations. Our interpretation of the structural data is that despite the random stacking, the well-separated FeSe layers themselves remain well ordered, which helps to explain our findings, described below, that robust superconductivity is preserved in these systems.

5.3.5 SQUID magnetometry

Magnetic susceptibility measurements were recorded using a Quantum Design MPMS-XL SQUID magnetometer. Samples of the Sr/NH_z intercalate (sample A, 30.2 and 29.8 mg) and the Sr/ND_z intercalate (34.0 and 30.2 mg) were filled and immobilized in gelatin capsules. Measurements were conducted in D.C fields of 5 mT in the temperature range 2–150 K after cooling in zero applied field (ZFC) and in the measuring field (FC).

The magnetometry measurements performed directly after the synthesis (Fig. 5.5) indicate bulk superconductivity with a noticeable sharp drop to negative susceptibility values at $T_c = 36(1)$ K for sample A ($\sim 35\,K$ for the second sample). There is no effect of H/D substitution on T_c. Although the superconducting volume fraction is larger in the case of D, the difference is consistent with the natural variability of volume fractions achieved in different syntheses. Even after nine months, the superconducting volume fractions and the sharp drop at T_c were found to be unchanged. A small reduction in T_c (of 2–3 K) was detected, although this was not found to be correlated with any significant change in structure. In the remainder of this Chapter, I shall present magnetometry and μSR data on the Sr/NH_z intercalate.

5.3.6 The upper critical field

The upper critical field H_{c2} of sample A was measured using the PDO dynamic susceptometer. As described in Chapter 2, the sensor coil is inductively coupled to the PDO circuit, which is essentially an LCR circuit with resonance frequency f that is measured as a function of field and temperature. For normal metals/superconductors, f is highly dependent on changes in the skin/penetration depth, thus when sweeping in field or temperature the onset of superconductivity is observed as a large change of f, at H_{c2} or T_c, due to the difference in skin and penetration depth of the two states.

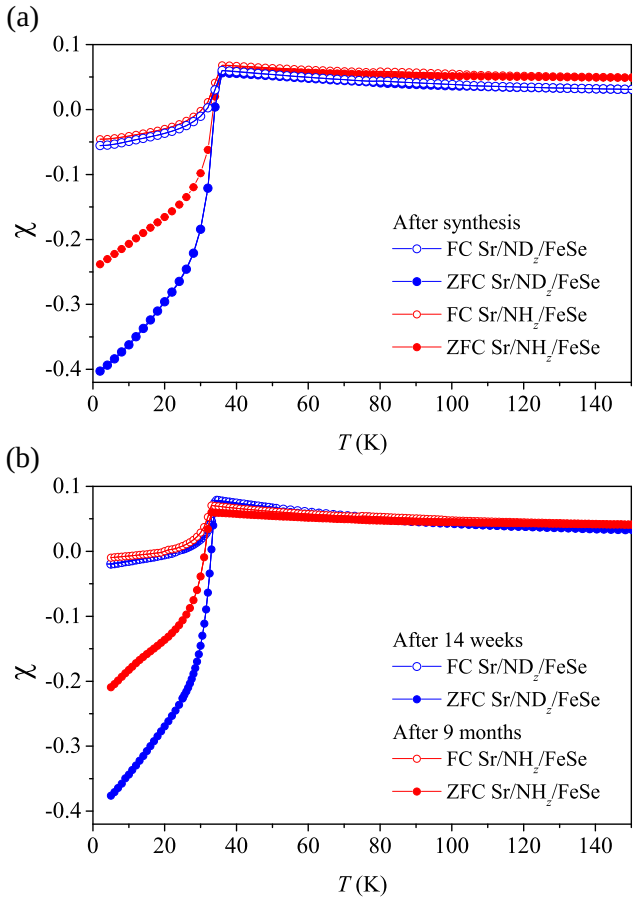

Figure 5.5: (a) Volume susceptibility χ of Sr/ND_z and Sr/NH_z (sample A) intercalated iron selenide after synthesis. (b) Measurements showing a slight decrease of T_c after 14 weeks and 9 months for the Sr/ND_z and the Sr/NH_z intercalate, respectively.

Data were taken for temperatures in the range $4.2-40\,\mathrm{K}$ in fields of up to 38 T with a measurement at 40 K serving as a normal-state reference. The data measured at each T is then offset such that the frequency in the normal state matches that measured at 40 K. Below T_c the onset of superconductivity is marked by a sudden rise in frequency and a deviation from the normal-state signal (see Fig. 5.6).

Additional heating can occur due to eddy currents that are generated in the mixed or normal state by the applied field. In some cases this produces hysteresis in the data and a shift in H_{c2}, with the effect being more pronounced with a larger $\mathrm{d}B/\mathrm{d}t$ (a shorter pulse length for the same maximum field). In this case, the samples were

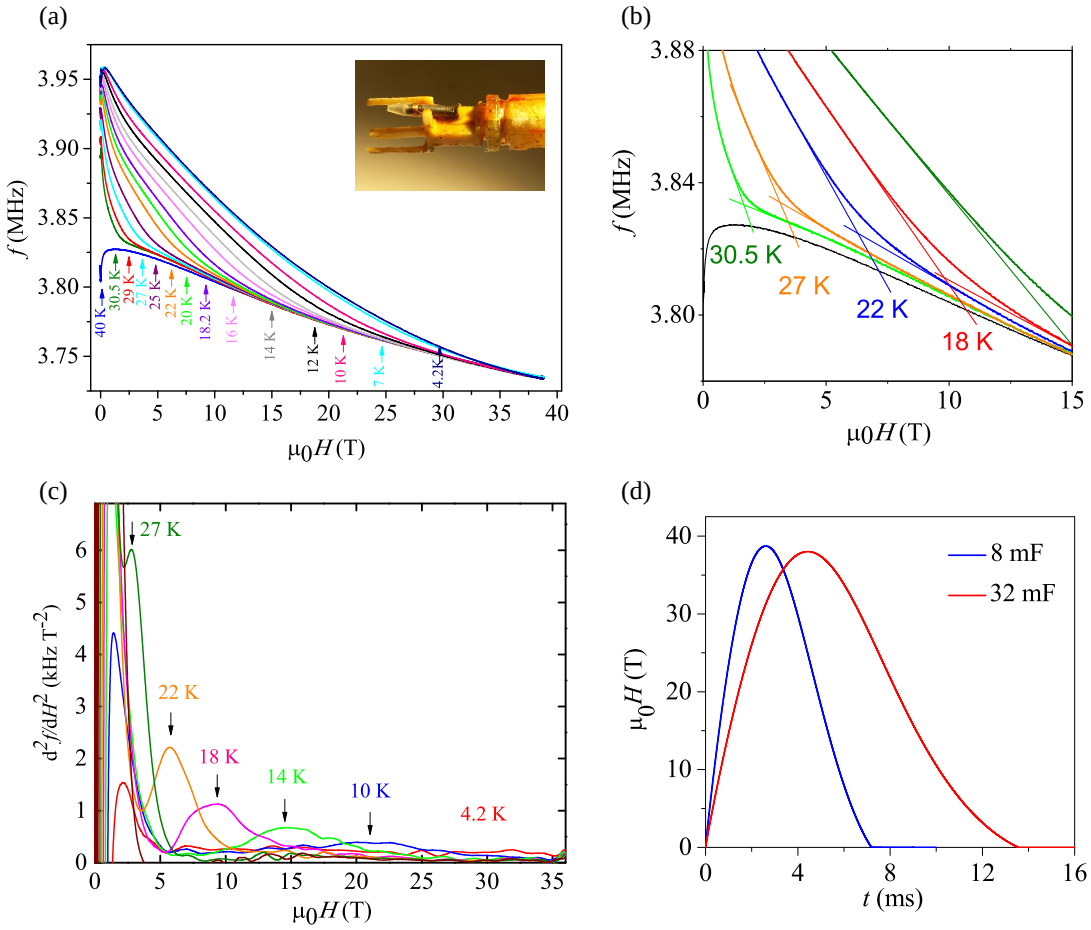

Figure 5.6: (a) Down-sweep portion of pulsed magnetic field data for $Sr_{0.3}(NH_2)_y(NH_3)_{1-y}Fe_2Se_2$ (sample A) at various temperatures $T \leq 40$ K. Data are offset so that the frequency in the normal state matches that measured at 40 K (blue line). Inset: sample mounted on the end of the PDO probe before lowering into cryostat. (b) Close-up showing the intersection of two slopes used to determine H_{c2}. (c) Second method for calculating H_{c2} as the peak position in $\mathrm{d}^2f/\mathrm{d}H^2$. (d) Typical 38 T field pulses demonstrate how $\mathrm{d}B/\mathrm{d}t$ varies with pulse length when using one or four banks of charging capacitors, each providing an energy of up to 0.2 MJ.

found to be insensitive to these effects as no difference in f was observed between varying pulse lengths between 7 ms and 14 ms (see Fig. 5.6(d) for field profiles of the pulses).

Note that due to the broadness of the phase transition, the value of H_{c2} is particularly difficult to determine at low T. This may be due to the critical field anisotropy between the in-plane and out-of-plane directions increasing as the system is cooled

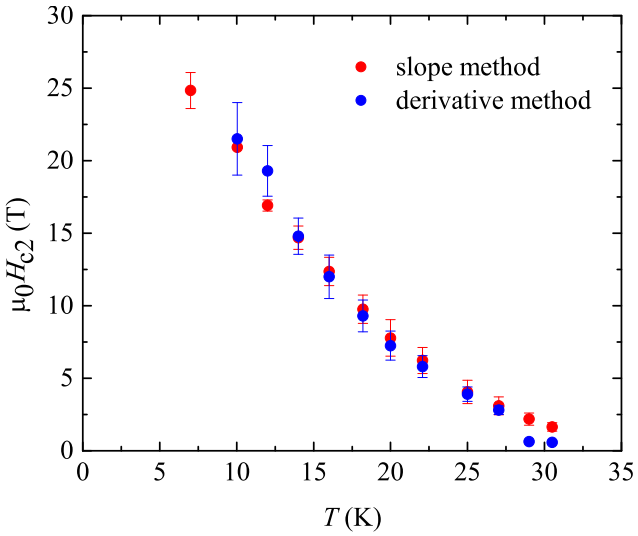

Figure 5.7: Phase diagram for $Sr_{0.3}(NH_2)_y(NH_3)_{1-y}Fe_2Se_2$ using the slope and derivative methods as described in the text. The transition is too broad for a reliable estimate of H_{c2} at 4.2 K.

and so for a powdered sample there is a more gradual change in frequency. To ensure H_{c2} is correctly measured, I define two different methods for extracting its value. Firstly, I take H_{c2} as the peak in $\mathrm{d}^2 f/\mathrm{d}H^2$ and its uncertainty as the half-width at half-maximum (see Fig. 5.6c). Secondly, one may perform a linear extrapolation of the curve on either side of the transition and define H_{c2} as the point of intersection of these two slopes. In this case, another criterion is the point at which the line extrapolated from the curve below the critical field crosses the normal-state signal. I take the uncertainty as the difference between these two points of intersection (see Fig. 5.6b). Both methods give similar results with H_{c2} increasing steadily as the sample is cooled, with the curve exhibiting a concave form (see Fig. 5.7) that has been observed in multi-band high T_c superconductors [122].

5.3.7 TF μSR

TF μSR was used to probe the internal field distribution in the vortex state. In this configuration, the measured asymmetry is proportional to the spin polarisation as

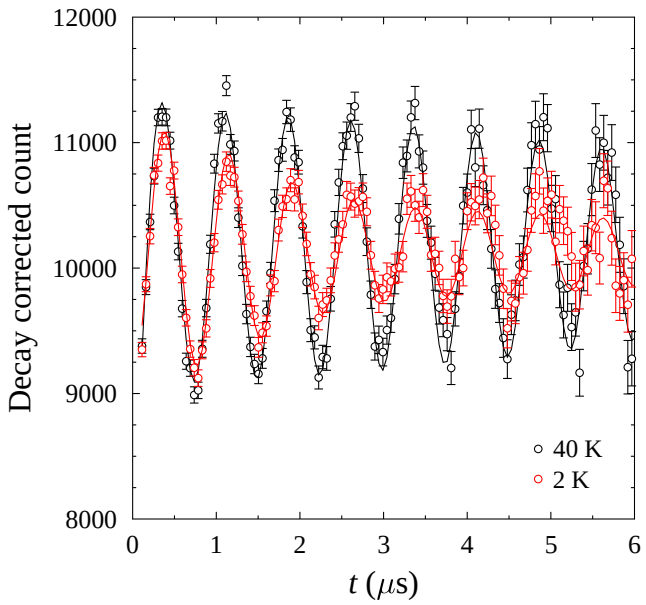

Figure 5.8: Example raw spectra (sample B) measured by a single bank of detectors on the MuSR spectrometer in a transverse field of 10 mT at 40 K (black points) and 2 K (red points). The increase in broadening below T_c signals the development of the vortex lattice.

measured by individual detector banks (see Fig. 5.8). This experimental situation can be modelled using a fit function;

$$\begin{aligned} A(t) = A_{\mathrm{bg}} \cos(\gamma_\mu B_{\mathrm{app}} t + \phi) \exp(-(\sigma_{\mathrm{bg}} t)^2/2) \\ + A_{\mathrm{VL}} \cos(\gamma_\mu B_{\mathrm{pk}} t + \phi) \exp(-(\sigma_{\mathrm{VL}} t)^2/2), \end{aligned} \tag{5.1}$$

where the phase ϕ results from the detector geometry, and A_{VL} and A_{bg} are the relaxing asymmetry due to vortex lattice and background contributions, respectively (the latter originates from muons stopping in the non-superconducting fraction of the sample or silver sample holder). This model assumes a symmetric Gaussian distribution of local fields with a peak value B_{pk} (B_{app}) and standard deviation, or damping factor, σ_{VL} (σ_{bg}) corresponding to the vortex lattice (background) contributions. Initially, data in the range $T \geq T_c$ were fitted with the background component only, with all parameters kept free. The average values of the temperature-independent

parameters (B_{bg}, σ_{bg} and ϕ) were calculated and the whole data range was refitted using Eq. 5.1 with these variables fixed. The output values of A_{VL} and A_{bg} from this second fitting routine were also found to be temperature independent in the range $T < T_c$. Their calculated averages were $A_{VL} = 6.46(6)\%$ and $A_{bg} = 19.8(9)\%$ for sample A, and $A_{VL} = 6.2(1)\%$ and $A_{bg} = 4.6(5)\%$ for sample B. This allowed for a further, final refinement of the fit using these fixed values of A_{bg} and A_{VL}. The width of the field distribution is given by $B_{rms} = \sigma_{VL}/\gamma_\mu$ and its temperature dependence is shown in Fig. 5.9.

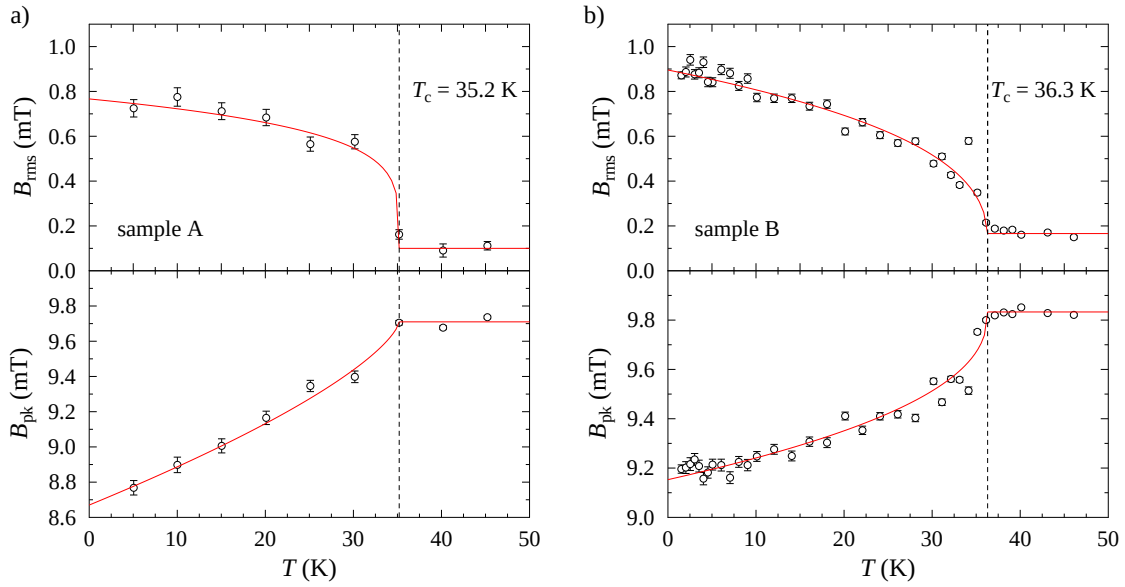

Figure 5.9: Temperature dependences of field width B_{rms} and peak field B_{pk} from TF μSR measurements of a) sample A (GPS data) and b) sample B (MuSR data). Fits (red lines) are to the Eq. 5.4 and Eq. 5.5, with the former used to extract absolute values of $B_{rms}(T = 0)$ and $\lambda_{ab}(T = 0)$.

We observe a broadening of the field distribution (increase in B_{rms}) when the samples are cooled through T_c in an applied field of 10 mT that can be attributed to the formation of the vortex lattice with superconductivity setting in at around 36.3(2) K and 35.2(2) K for sample A and B, respectively. These slight differences are to be expected from sample variation, particularly as sample A was measured in considerably less detail in the vicinity of the superconducting transition (the TF

measurements were performed primarily to confirm the sample quality prior to the LF and ZF measurements, which are discussed in the following sections).

As the material enters the superconducting state, the applied field is partially screened resulting in a diamagnetic shift in $B_{\rm pk}$ for $T<T_c$. For powdered samples, the effective penetration depth $\lambda_{\rm eff}$ is related to the field width via

$$B_0 = \frac{\sqrt{0.00371}\Phi_0}{\lambda_{\rm eff}^2}, \tag{5.2}$$

where Φ_0 is a magnetic flux quantum and B_0 is the vortex lattice contribution to $B_{\rm rms}$ [123]. Note that $\lambda_{\rm eff}$ is a powder average over all orientations, therefore it contains contributions from both the in-plane and out-of-plane components denoted by $\lambda_{\rm ab}$ and $\lambda_{\rm c}$, respectively. However, for strongly anisotropic superconductors such as these (in the limit $\lambda_{\rm c}/\lambda_{\rm ab} \geq 5$), $\lambda_{\rm eff}$ is known to be dominated by $\lambda_{\rm ab}$ and approximated by $\lambda_{\rm eff} = 3^{\frac{1}{4}}\lambda_{\rm ab}$ [123]. Thus Eq. 5.2 becomes

$$B_0 = \frac{\sqrt{0.00371}\Phi_0}{(3^{\frac{1}{4}}\lambda_{\rm ab})^2}. \tag{5.3}$$

For these data, it is assumed that the only other contribution to $B_{\rm rms}$ is from nuclear dipole fields, which are temperature independent and add inquadrature. We fit our data to the phenomenological functions:

$$B_{\rm rms}(T) = \left\{ B_0^2 \left[1 - \left(\frac{T}{T_{\rm c}} \right)^{\alpha} \right]^{2\beta} + B_{\rm dip}^2 \right\}^{\frac{1}{2}} \tag{5.4}$$

$$B_{\rm pk}(T) = B_{\rm app} - B_{\rm dia} \left[1 - \left(\frac{T}{T_{\rm c}} \right)^{\alpha'} \right]^{\beta'}, \tag{5.5}$$

where $B_{\rm dia}$ is the maximum diamagnetic shift of the peak field, and B_0 and $B_{\rm dip}$ are the widths corresponding to the vortex lattice (at $T = 0$) and nuclear dipole contributions, respectively. For the fits shown in Fig. 5.9 the fitted parameters are $\beta = 0.18(4)$ and

$\beta' = 0.7(1)$ for sample A, and $\beta = 0.33(3)$ and $\beta' = 0.43(3)$ for sample B, both with fixed $\alpha = \alpha' = 1$. Using a weighted average of the extracted values of B_0 (considering the measurements of sample A were less detailed) we calculate a penetration depth of $\lambda_{ab}(T = 0) = 292(3)$ nm.

5.3.8 ZF and LF μSR

ZF μSR was used to further probe the intrinsic magnetism of the system. These measurements were performed on sample A only. No spontaneous oscillations were observed in the forward-backward asymmetry across the whole temperature range, nor was there any discontinuous change in amplitudes or recovery of the baseline asymmetry at low temperatures (see Fig. 5.10a). Together these make the presence of any long-range magnetic order unlikely. Given that the spectra do not follow a Kubo-Toyabe relaxation, it is also unlikely that the relaxation is caused solely by nuclear moments. The lack of recovery of the baseline asymmetry at late times suggests dynamic fluctuations and we therefore attribute the ZF signal to relaxation caused by disordered, fluctuating electronic moments. The data were fitted to the function

$$A(t) = A_{\text{rel}} \exp(-\lambda t) + A_{\text{base}}, \tag{5.6}$$

where A_{rel} is the relaxing asymmetry with relaxation rate λ and A_{base} is a non-relaxing background. A_{rel} can be considered as the lower bound for the superconducting volume fraction, which for this sample was around 1/3. As previously mentioned, exponential relaxation is often used to model dense spin systems that are dynamically fluctuating, where the relaxation rate λ is proportional to the variance of the local magnetic field distribution and also to the fluctuation time, or a dilute spin system in the presence of dynamic fluctuations. Upon cooling, the relaxation rate λ (Fig. 5.10b) begins to increase gradually with decreasing temperature. Once cooled below T_c it

increases far more rapidly, suggesting that the relaxation rate is in some way coupled to the superconducting order parameter.

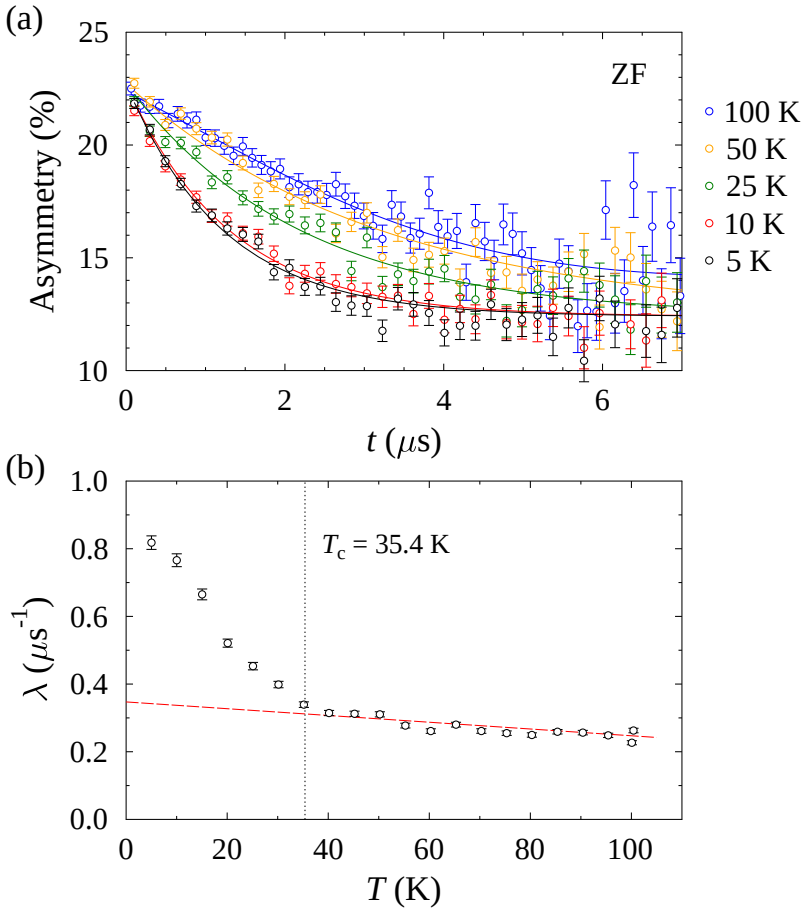

Figure 5.10: (a) Example asymmetry spectra from ZF μSR measurements taken on sample A (GPS data). Fits are to Eq. 5.6. (b) Temperature dependence of relaxation rate λ measured in zero-field. Below T_c the data points deviate sharply from the linear trend (red line).

LF measurements were made at 5 K and 100 K in fields of up to 200 mT (see Fig. 5.11). For data measured at 5 K (Fig. 5.11a) the sample was cooled below T_c in zero applied field. At both temperatures the relaxation is decoupled at relatively low fields ($\approx$ 5 mT at 100 K and $\approx$ 20 mT at 5 K), suggesting that the relaxation is due to fairly dilute and/or static spins with residual dynamic fluctuations. One scenario is that there is a sizeable contribution to the ZF relaxation from static nuclear moments,

with dilute, fluctuating electronic moments providing additional relaxation. The lack of any peak in λ suggests the absence of any freezing of the dynamics of the moments (as one would expect in a spin glass due to magnetic interactions), supporting the interpretation that these are dilute and not strongly interacting with each other. The fact that the relaxation rate is coupled to the superconducting order parameter implies that the moments are embedded in the superconductor, rather than in phase-separated pockets. At high temperatures compared to T_c, the moment size and/or fluctuation rate increase slowly upon cooling. Upon cooling below T_c, the muon spins likely experience a combination of slower fluctuation times, larger moments and an increased width of the field distribution. The latter could arise in a manner analogous to the increase in B_{rms} in the TF measurements. Specifically, if the moments are locally in a normal (rather than superconducting) region and sufficiently numerous that there is a degree of overlap of their magnetic fields in the superconducting regions, then the decreasing penetration depth upon cooling would lead muons, which decorate all of the sample, to experience a broader distribution of local fields. Taken together, the ZF measurements therefore suggest the presence of a small concentration of dilute magnetic moments dispersed in the superconducting volume, but whose presence does not seem to adversely affect the presence of superconductivity.

5.3.9 Discussion

Pulsed-field measurements indicate an upwards curvature in H_{c2} vs temperature (see Fig. 5.7), which may be indicative of a multiband nature. This type of behaviour has been observed in other layered two-band superconductors such as the FeAs-based systems [124, 125], and the parent compound FeSe using resistivity measurements [60]. Fits of the Werthamer-Helfand-Hohenberg (WHH) model [126] for a one-band superconductor in the dirty limit did not converge. Instead we use a model developed by Gurevich that is based on a weakly-coupled two-band BCS superconductor [127,

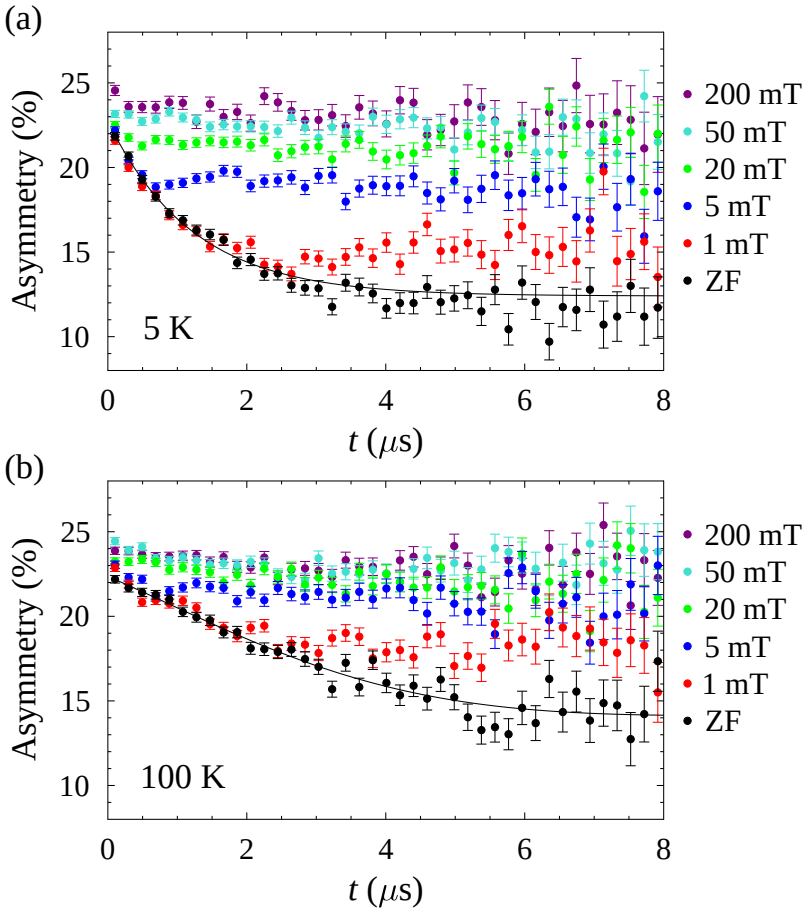

Figure 5.11: Example LF μSR spectra at (a) 5 K and (b) 100 K (sample A). Above T_c the spins are decoupled at relatively low fields (≈ 5 mT).

128]. This includes scattering from non-magnetic impurities, orbital pair breaking, strong electron-phonon coupling, and spin paramagnetism (note that unlike the WHH model, it does not account for spin-orbit effects). The model parameters are the band diffusivities D_1 and D_2, and the intraband (λ_{11} and λ_{22}) and interband (λ_{12} and λ_{21}) coupling constants. Assuming that the non-magnetic impurity scattering does not affect T_c the upper critical field is given in reduced natural units $h = H_{c2}D_1/2\phi_0 T$

and $t = T/T_c$ by

$$\begin{aligned} &a_0[\ln t + U(h)][\ln t + U(\eta h)] \\ &\quad + a_2[\ln t + U(\eta h)] + a_1[\ln t + U(h)] = 0, \end{aligned} \tag{5.7}$$

where

$$U(x) = \psi\left(\frac{1}{2} + x + i\frac{\mu_B H}{2\pi T}\right) - \psi(x), \tag{5.8}$$

in which $\psi(x)$ is the digamma function, $\eta = D_2/D_1$ is the ratio of band diffusivities, and the constants a_0, a_1 and a_2 are functions of the coupling constants.

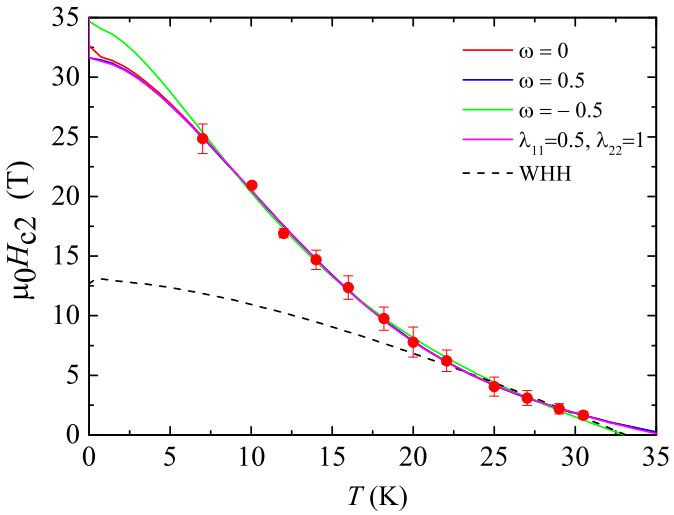

Figure 5.12: Fits of H_{c2} using the two-band Gurevich model (Eq. 5.7) with either a fixed ω or fixed intraband coupling constants λ_{11} and λ_{22} (H_{c2} determined by the slope method). Dotted line shows a fit to the single-band WHH model.

In any case, the model is difficult to fit due to overparameterisation; at high temperatures, H_{c2} is strongly dependent on D_2/D_1 and weakly dependent on the coupling constants, which contribute significantly only in the mK temperature range. Consequently, fits to the data converge only when one set of coupling constants (either interband or intraband) are fixed. Fits are shown in Fig. 5.12 for various values of $\lambda_{11}, \lambda_{22}$ and $w = \lambda_{11}\lambda_{22} - \lambda_{12}\lambda_{21}$. The Gurevich model was successful in modelling the upwards curvature of H_{c2} which stems from the difference in diffusivities of the two

bands i.e. $\frac{D_2}{D_1} < 1$ [128]. However, we found that it was possible to fit for both a strong (when $w < 0$) and weak ($w > 0$) interband coupling and fitted parameters varied considerably depending on the values of the chosen coupling constants and the method for finding H_{c2}. This is particularly noticeable when extrapolating $H_{c2}(T)$ to absolute zero. When using H_{c2} values extracted by the slope method as described earlier, we find $\mu_0 H_{c2}(0) \approx 33(2)$ T to be fairly consistent across various different scenarios (see Fig. 5.12). The derivative method for calculating H_{c2} could not be extended to the lowest temperature datum and hence produced a poorly constrained estimate, thus this method was deemed less reliable.

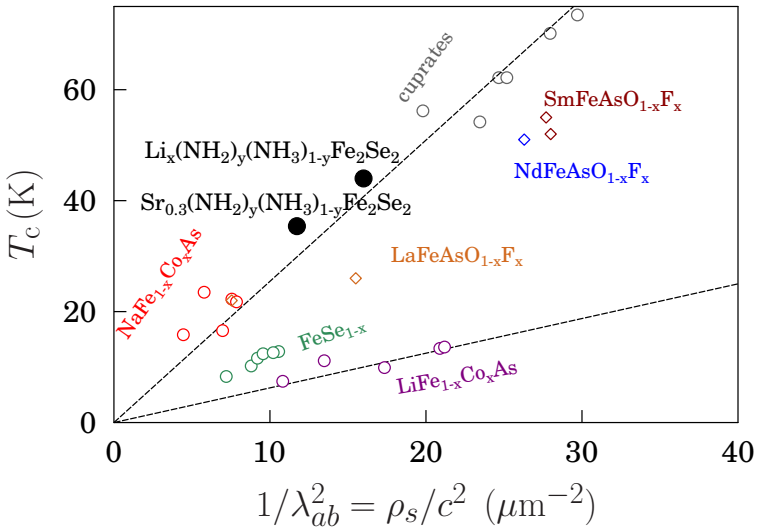

Figure 5.13: The Uemura plot of T_c against superfluid stiffness $\rho_s = \frac{c^2}{\lambda_{ab}^2}$ shows that the intercalates $A_x(NH_2)_y(NH_3)_{1-y}Fe_2Se_2$ ($A = Sr, Li$) fall close to the main scaling line.

The Uemura relation [129] is a scaling relation between T_c and the superfluid stiffness ρ_s which seems to hold well for many exotic superconductors [130]. It is known to break down for overdoped cuprates [131] and may be an over simplification [132], and other scaling relation behaviours have been explored [133, 134, 135, 136]. Nevertheless, the Uemura plot of T_c against ρ_s provides a convenient means of exploring the energy scale to break up pairs as a function of the strength of the order parameter,

and our TF μSR data allow us to extract an estimate of $\rho_s = c^2/\lambda_{ab}^2$, where c is the speed of light [137]. As shown in Fig. 5.13, we find that the Sr intercalated compound is close to the main scaling line on the Uemura plot, as is the Li intercalated material [109], and this behavior correlates with underdoped cuprates and many other iron-based superconductors. Note that there is also another, lower line in this plot, which is common to electron-doped cuprates [138, 139] and $LiFe_{1-x}Co_xAs$ [140, 141]. For those materials, it is found that although the superconducting state is reasonably robust (the superfluid is stiff) the strength of the pairing is significantly suppressed, but these considerations do not seem to apply to our intercalated compounds.

5.3.10 Conclusion

In this section I have presented a study on superconducting properties of a recently discovered superconductor $Sr_{0.3}(NH_2)_y(NH_3)_{1-y}Fe_2Se_2$ using pulsed-field magnetometry and μSR techniques. The upper critical field was shown to increase upon cooling and exhibited a concave form that is reminiscent of other multigap high-temperature superconductors, which when extrapolated to absolute zero gives a maximum upper critical field of $\mu_0 H_{c2}(0) \approx 33(2)$ T. TF μSR measurements show a clear diamagnetic shift and a broadening of the field width that is highly reproducible between different batches of sample, with the onset of superconductivity at ≈ 36 K. ZF μSR did not reveal any long-range magnetic order but indicated dilute electronic moments with some residual dynamics and whose behaviour is coupled to the superconducting order parameter. We find that intercalation of Sr atoms together with amide and ammonia introduces intrinsic stacking disorder that results in a paracrystalline state. The system nevertheless retains complete structural order of the Fe sublattice, and thus these results demonstrate that robust superconductivity does not rely on perfect structural coherence along the c-axis.

5.4 The role of ammonia in $\mathbf{Li}_x[(\mathbf{NH_2})_y(\mathbf{NH_3})_{1-y}]_z\mathbf{Fe_2Se_2}$ $(z = 1, 2)$

5.4.1 Introduction

I now turn to the case where Li and ammonia are used as the intercalated species. This compound was initially characterised by Burrard-Lucas and co-workers who reported a T_c of 43(1) K [109]. I will henceforth refer to this compound, $Li_x[(NH_2)_y(NH_3)_{1-y}]$-$Fe_2Se_2$, as the 'ammonia-poor' intercalate (or NH_3-poor, $z = 1$). A later study which monitored the intercalation reaction *in situ* on a synchrotron beamline indicated an intermediate intercalated superconducting phase that is much richer in ammonia [97] (see Fig. 5.14), with a slightly lower critical temperature of 39 K ($z = 2$). Following these findings, this 'ammonia-rich' (or NH_3-rich) phase $Li_x[(NH_2)_y(NH_3)_{1-y}]_2Fe_2Se_2$ has been synthesised in bulk by co-workers S. J. Clarke *et al.* and its structure refined [97]. In this section I report on an experiment to measure the penetration depth and volume fraction of the two phases and confirm whether these reactions result in superconductors that track the Uemura scaling line or show anti-correlating behaviour. The previous study in [109] has shown a means to probe these reactions *in situ* using powder x-ray diffraction in which the measured product is obtained by reaction of iron selenide with liquid ammonia solution of Li and subsequently exposed to 1 bar of ammonia at 250 K. Here, I now combine this technique with μSR in order to measure the internal field distribution *in situ* as one phase is converted to the other.

5.4.2 Experimental methods

This work forms part of a collaboration with S. J. Clarke and co-workers [142]. Synthesis and characterisation were carried out by D. N. Woodruff and S. J. Cassidy.

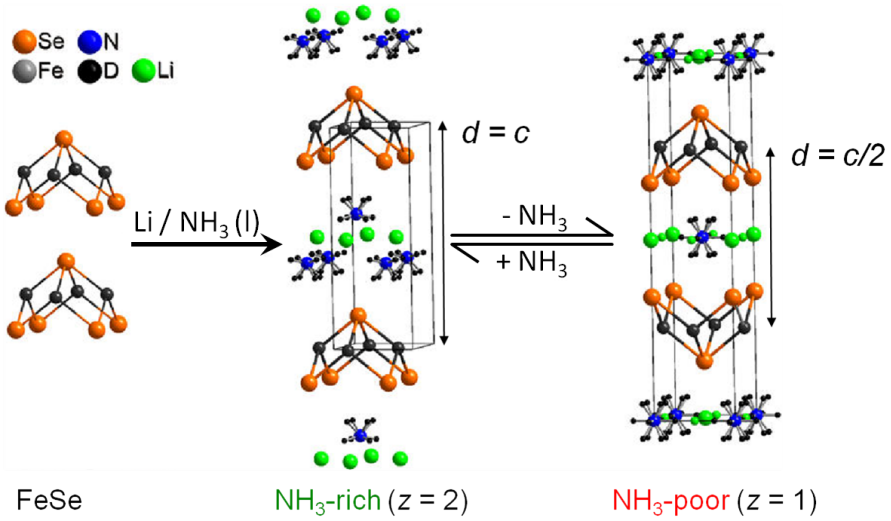

Figure 5.14: The reaction of NH_3 with FeSe (left) to produce the NH_3-poor phase (right) via an NH_3-rich phase (middle). The interlayer spacing d is indicated. Adapted from Ref.[119].

μSR experiments were performed on the MuSR spectrometer by myself and D. N. Woodruff with the assistance of F. L. Pratt, P. J. Baker, T. Lancaster and S. J. Blundell. Time-domain fitting of the data was performed by myself. Fourier transform spectra were also generated by myself and analysed by S. J. Blundell to provide an independent estimate of the superfluid stiffness.

For the experiment, the ammonia-poor sample was initially prepared via the procedure previously reported in [109]. Due to its air-sensitivity the sample was isolated and transferred to a He filled glovebox where it was loaded into a muon TiZr sample holder with TiZr foil windows which was mounted in a ^{4}He bath cryostat. To 'charge' the sample with ammonia a modified procedure similar to that previously reported in Ref.[119] was used; the sample holder was attached to an in-house built gas handling set-up and placed under dynamic vacuum before being cooled to 250 K. Once the temperature had equilibrated, the dynamic vacuum was removed and the sample was exposed to a buffer volume of ammonia gas, which was at a pressure of 1 bar. The amount of ammonia absorbed by the sample was monitored by monitoring the pressure of the ammonia inside the buffer volume; once the pressure had stabilised, the

holder was sealed and the sample measured. Discharging ammonia from the sample was done by evacuating the buffer volume and warming the sample to 250 K. It was then exposed to the 'static' vacuum of the buffer volume and slowly warmed to room temperature. Finally the sample was placed under a dynamic vacuum for 2 hours to produce the 'ammonia-poor' phase, which was then released and remeasured. The sample was cooled in a transverse magnetic field of $B_{\rm app} = 10\,{\rm mT}$ and data were collected in the temperature range 1.5 K to 50 K using the MuSR spectrometer at the ISIS muon facility, RAL. Note that $B_{\rm app}$ is estimated to be well above the lower critical field B_{c1} given that it is of the order $\sim 3\,{\rm mT}$ [143] in the parent compound and that values of 3–8 mT have been reported in other intercalated FeSe compounds [118, 144]. We shall see in the next section that due to the pressurised cell, the data are contaminated by an unavoidable larger background signal from muons stopped within the apparatus but outside the sample. Nevertheless, this technique of performing the chemical transformations *in situ* ensured that both phases were accessible to study while all details of the background from the sample holder and cryostat remained unchanged.

5.4.3 Results

Two independent methods were used to analyse the data and extract a value of the superfluid stiffness $\rho_{\rm s}$. Firstly, the data were fitted in the time-domain assuming a Gaussian distribution of local fields with mean value $B_{\rm pk}$ in the applied field $B_{\rm app}$, described by Eq. 5.1. As in the previous case, the normal state was initially fitted with the background component only to calculate the average values of $B_{\rm bg}$, $\sigma_{\rm bg}$ and ϕ, which are temperature independent, and then the whole data range refitted with the complete function using these fixed values. Further refinement was achieved by a final fit using averaged values of $A_{\rm bg}$ and $A_{\rm VL}$. The width of the field distribution $B_{\rm rms} = \sigma_{\rm VL}/\gamma_\mu$ is shown in Fig. 5.16. As the sample is cooled below $T_{\rm c}$ an increase

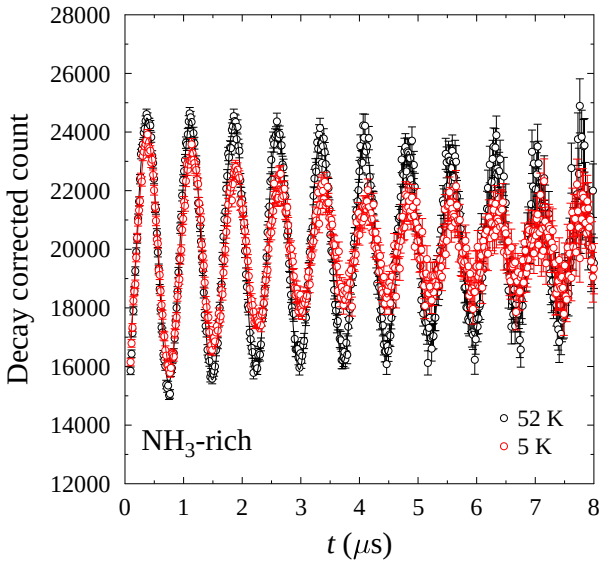

Figure 5.15: Example raw spectra of NH_3-rich sample measured by a single bank of detectors on the MuSR spectrometer in a transverse field of 10 mT at 52 K (black points) and 5 K (red points).

in broadening and a diamagnetic shift are observed in both phases, which signals the development of the vortex lattice. The lower bound for the superconducting fraction A_{VL} is found to be virtually unchanged following de-absorption (≈ 0.53 for the NH_3-rich phase and ≈ 0.48 for the NH_3-poor phase). A small peak is visible at $38 < T < 42$ K in the NH_3-rich phase, however these data were found to be contaminated by dynamic stray fields from a nearby spectrometer and hence were not included in the subsequent fits (none of the remaining data were affected). Again, assuming the only other contribution to to B_{rms} is from nuclear dipole fields, the field width and diamagnetic shift are fit to the usual phenomenological functions described by Eq. 5.4 and Eq. 5.5, the results of which are shown in Table 5.1 and Table 5.2. The field distribution widths were found to be similar in both cases ($B_0 \approx 0.54$ mT, $B_{\mathrm{dip}} \approx 0.19$ mT for NH_3-poor and $B_0 \approx 0.58$ mT, $B_{\mathrm{dip}} \approx 0.19$ mT for NH_3-rich) but the fitted values for T_c varied slightly at 42.8(9) K and 38.5(3) K for the NH_3-

poor and NH_3-rich phases, respectively. These extracted values of T_c are in excellent agreement with the previous study, demonstrating that the charging and discharging of ammonia acts exactly as found previously [109, 119] and that there are two distinct superconducting phases with different bulk responses, although we note that the transition in the NH_3-poor phase appears some-what broader.

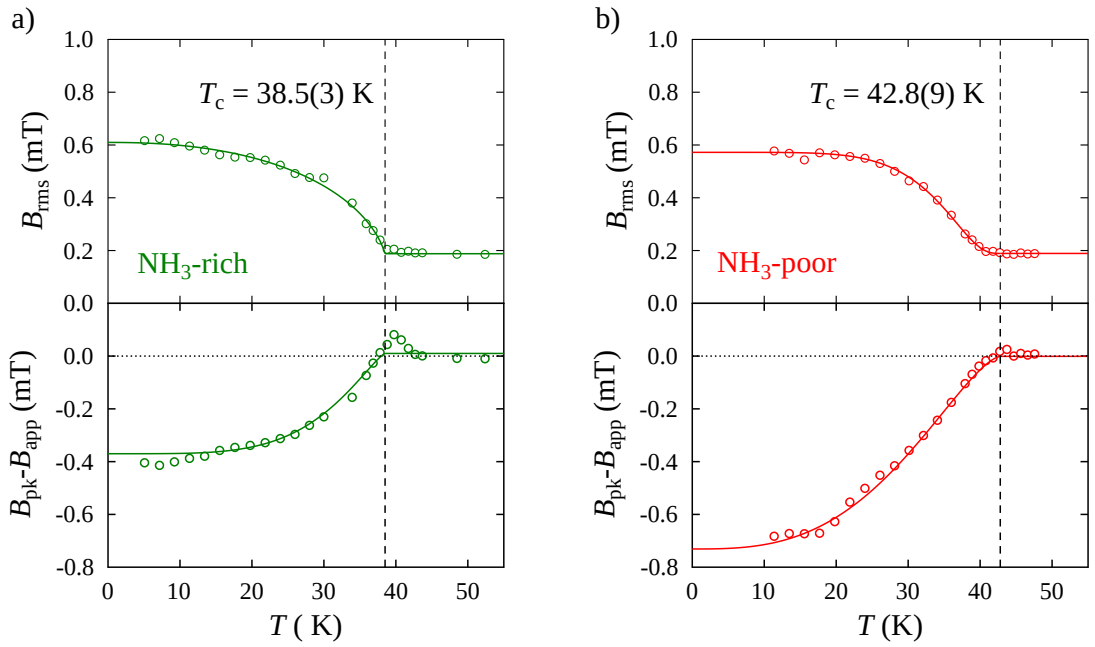

Figure 5.16: The mean field width B_{rms} and diamagnetic shift $B_{pk} - B_{app}$ of the a) ammonia-rich sample and b) the ammonia-poor sample, as measured in a transverse field of 10 mT. Fits are to the usual phenomenological functions Eq. 5.4 and Eq. 5.5.

.

Using Eq. 5.3, the values of the in-plane penetration depth at 0 K extracted from these data are $\lambda_{ab}(0) = 0.364(3)\,\mu$m and $\lambda_{ab}(0) = 0.354(3)\,\mu$m for the NH_3-poor and NH_3-rich phases respectively, where the quoted errors are statistical. Note that Eq. 5.3 is valid in the range $0.13/\kappa^2 \ll b \ll 1$, where $b = B_{app}/B_{c2}$ and $\kappa = \lambda_{ab}/\xi_{ab}$ is the Ginzburg-Landau parameter [145]. In this case, we expect the upper critical field B_{c2} to be extremely high given that it is $\approx$ 18 T in the parent compound FeSe [146, 147], and reported to be $\approx$17 T [148] in some intercalated FeSe compounds or, as we have seen in the previous section, as high as 33 T for the Li/NH_3 intercalate [117].

Phase	T_c (K)	$\lambda_{ab}(0)$ (μm)	B_0 (mT)	B_{dip} (mT)	α	β
NH_3-poor	42.8(9)	0.364(3)	0.54(1)	0.73(2)	6.0(5)	1.6(4)
NH_3-rich	38.5(3)	0.354(3)	0.58(1)	0.38(1)	2.3(4)	0.44(6)

Table 5.1: The critical temperature, in-plane penetration depth and fitted parameters with statistical errors extracted from time-domain data using Eq. 5.4 to model B_{rms}.

Phase	T_c (K)	B_{dia} (mT)	α‘	β‘
NH_3-poor	42.8(9)	0.73(2)	2.9(2)	1.54(9)
NH_3-rich	38.5(3)	0.38(1)	4.5(7)	1.3(2)

Table 5.2: The critical temperature and fitted parameters with statistical errors extracted from time-domain data using Eq. 5.5 to model B_{dia} (with T_c fixed from fits of $B_{rms}(T)$).

Thus with $B_{app} = 10\,\text{mT}$ the limit $b \ll 1$ is satisfied. Furthermore, the coherence length is given by $\xi_{ab} = \sqrt{\phi_0/2\pi B_{c2}}$, which for these values of B_{c2} gives ∼3–6 nm and hence we expect $\kappa \approx 100$, which satisfies $b \gg 0.13/\kappa^2$.

Previous studies show an increase in B_{rms} below ≈10 K [109] that has been linked to two-gap behaviour. However, data for the NH_3-poor phase below 10 K were omitted due to a reduction in amount of ammonia exchange gas in this configuration, which made it difficult to establish thermal equilibrium at low T. Thus we cannot confirm or rule out any multiband behaviour with the current data, although we note that the NH_3-rich phase appears to show single band superconductivity with the average field levelling off down to 5 K. Nevertheless, it is interesting to observe a difference in sample response, particularly as the sample was obtained from the same batch of synthesis as previously measured by Burrard-Lucas *et al.* One possibility is that the low T feature is of magnetic origin, although no extra features have been observed in susceptibility measurements to confirm this [109]. As tetragonal FeSe is a superconductor of $T_c = 8.5\,K$ [107], the increase in B_{rms} may have indicated some traces of the non-intercalated parent compound. However, this seems unlikely as neutron scatter-

ing data in the same study [109] reported a minority phase of only 1.4%. Furthermore, whilst B_{rms} is roughly the same between the two phases, the total diamagnetic shift for the NH_3-poor case ($\approx 0.73\,\mathrm{mT}$) is considerably larger than that of the NH_3-rich phase ($\approx 0.38\,\mathrm{mT}$). For a perfect vortex lattice, theory predicts that there is a precise numerical relationship between B_0, the rms field width due to superconductivity, and $B_{\mathrm{app}} - B_{\mathrm{pk}}$, the separation between the applied field and the field at which the field distribution peaks. This relationship is given by $(B_{\mathrm{app}} - B_{\mathrm{pk}})/B_0 \approx 0.6$ [149], but our experiment shows that this holds approximately only for the NH_3-rich phase. These discrepancies are most likely an artefact due to the difficulty in reliably separating the superconducting signal from the unavoidable large background in the time domain fitting using Eq. 5.1. Thus, the analysis was repeated using an alternative method in the frequency (i.e. field) domain, which is described in the following.

5.4.4 Field domain fitting

Fourier spectra for the NH_3-poor and NH_3-rich samples in the superconducting phase are shown in Fig. 5.17(a), both at $T = 11\,\mathrm{K}$. This temperature was chosen as it was the lowest common value between the two phases. The main maximum centred at 10 mT is the background signal, dominated by muons in the sample holder and cryostat, while the shoulder on the left-hand side of this central maximum represents the superconducting signal from the sample. The data are fitted using a function comprising a sum of a Gaussian (i.e. the background component, shown by the blue-dashed line in Fig. 5.17), and a field distribution calculated for a triangular flux lattice [150] which was broadened by a Gaussian to model the effect from nuclear dipole fields. The fitting parameters used for the flux lattice were the peak field, field width (B_0) and width of the Gaussian broadening function; and for the background component, the field width and applied field. The value of the in-plane penetration depth (related to B_0 via Eq. 5.3) was adjusted and the rest of the parameters refitted to minimise χ^2 (see

Fig. 5.18). The best-fit flux lattice distribution is shown in the inset in Fig. 5.17(a).

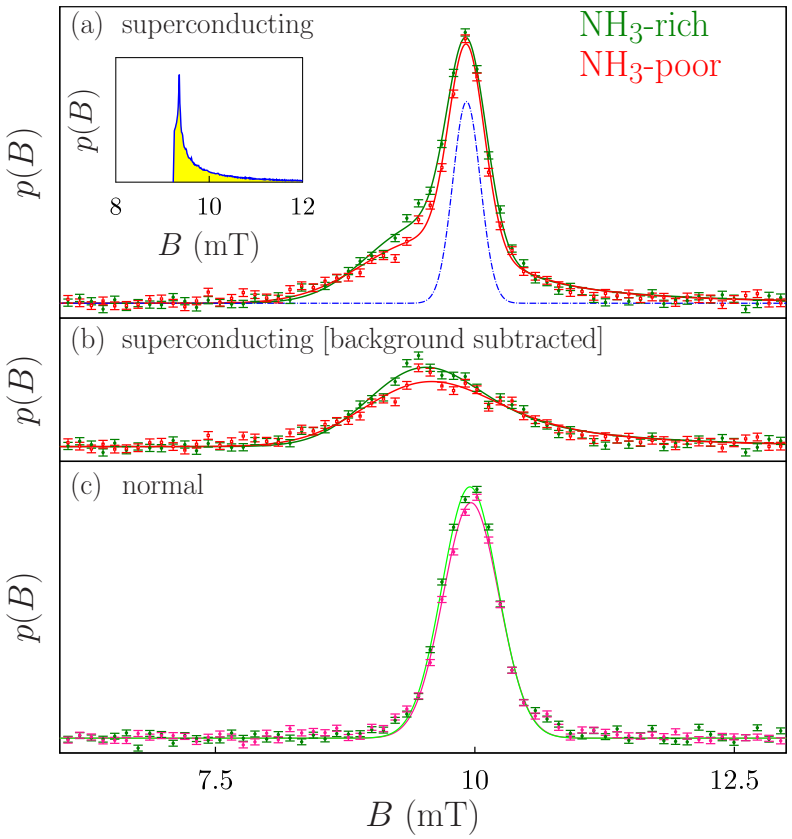

Figure 5.17: (a) The Fourier spectra at 11 K for the NH_3-poor and NH_3-rich phases. The largest peak is the background, the fit to which is shown as the narrow blue Gaussian curve. The remaining data are fitted using a broadened superconducting lineshape (unbroadened lineshape shown in the inset). (b) Spectra with the fitted backrgound subtracted for both of the low temperature data (11 K). (c) The unsubtracted data in the normal state (at around 48 K).

The spectra corresponding to the superconducting sample (data points) and best best fits (solid lines) are shown again in Fig. 5.17(b), but with the background signal subtracted. The corresponding spectra for the normal state (taken at around 48 K) are shown in Fig. 5.17(c) without background subtraction for comparison. This method gave a value of $\lambda_{ab}(11\,\mathrm{K}) = 0.34(1)\,\mu$m for both compounds.

For a direct comparison with the time-domain fitting method, the penetration depth was recalculated for $T = 11$ K. Using Eq. 5.4, we take the flux lattice contribu-

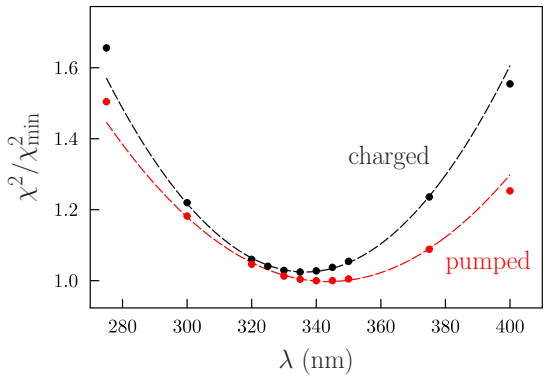

Figure 5.18: Reduced χ^2 values for the NH_3-rich (black points) and NH_3-poor (red points) data fitted in the field-domain using various penetration depths.

tion to the field width as $B(T) = B_0\left[1 - \left(\frac{T}{T_c}\right)^{\alpha}\right]^{\beta}$, with fitting parameters as listed in Table 5.1. and Table 5.2., and substitute this as 'B_0' in Eq. 5.3. This gave a value of $\lambda_{ab}(11\,\mathrm{K}) = 0.36(1)\,\mu$m for the NH_3-rich phase and $\lambda_{ab}(11\,\mathrm{K}) = 0.37(5)\,\mu$m for the NH_3-poor phase. Calculating the superfluid stiffness using $\rho_s(11\,\mathrm{K}) = c^2/\lambda^2_{ab}(11\,\mathrm{K})$, we see that the field-domain analysis yields a value of $\rho_s(11\,\mathrm{K})$ for the NH_3-rich phase that is $\approx 12\%$ larger (or $\approx 18\%$ for NH_3-poor) than that obtained by the time-domain method. This demonstrates that the two approaches give results that are broadly consistent. However, the field-domain method does separate the contributions of the sample and background more accurately and hence we calculate the superfluid stiffness at 0 K, using $\rho_s(T)$ obtained using the first method, but scaled up by a factor of 1.15. This gives values of $\rho_s(0) = 9.2(2)\,\mu\mathrm{m}^{-2}$ for NH_3-rich and $\rho_s(0) = 8.7(1)\,\mu\mathrm{m}^{-2}$ for NH_3-poor. A plot of the temperature dependence of $\rho_s(T)$ (See Fig. 5.19a) shows a clear difference in T_c between the two phases and an apparent small difference in the fitted $\rho_s(0)$, although this may be due to the dataset in the NH_3-poor sample extending down to 11 K only. Given the current data, it is reasonable to assume an average value of $\rho_s(0) = 8.9(2)\,\mu\mathrm{m}^{-2}$, which corresponds to a penetration depth of $\lambda_{ab}(0) = 0.335(3)\,\mu$m. This is slightly longer than that measured by Burrard-Lucas

et al. at 0.25(1) μm for the NH_3-poor phase [109].

The results of these measurements are shown on the Uemura plot of ρ_s against T_c in Fig. 5.19(b). We observe that both phases fall close to the main scaling line, similar to that observed for the Sr-intercalate described earlier, and many other iron-based superconductors [117, 151, 152, 153, 154, 155], as well as the cuprates and heavy fermion compounds [129, 130], although note that the $LiFe_{1-x}Co_xAs$ compounds have enhanced fluid stiffness and fall on a different line [140]. However, both phases display a reduced superfluid stiffness than what would be expected for their high values of T_c. This may indicate some degree of 'dirtiness' as strictly speaking, ρ_s is multiplied by a factor $(1+\xi/l)^{-1}$ where l is the mean-free path. Usually $l \gg \xi$ (clean limit), but in this case if $l \sim \xi$, which is likely a few nanometres, it could lead to the observed reduction. By comparison, we see that the Sr-containing NH_3 intercalate described in section 5.3 falls closer to the main scaling line.

Studies have shown that if superconductivity is controlled by the two-dimensional superfluid stiffness within the superconducting layers, in this case FeSe, one would expect $T_c \propto d/\lambda_{ab}^2$ [156] where d is the interlayer spacing. Fig. 5.19(c) demonstrates that this relationship is only approximately held for the FeSe-containing compounds, indicating that there are clearly other factors at play. Also shown is the behaviour of T_c as a function of d (Fig. 5.19d). We observe an initial increase in T_c as d increases, although this saturates at higher interlayer spacings, as found in previous FeSe-containing superconductors [111, 157]. Furthermore, the NH_3-rich phase is observed to have the lower T_c, but larger d-spacing (1.06 nm compared to 0.83 nm for the NH_2-poor phase) which is contrary to the general trend. This demonstrates that changes in the electron doping level of the FeSe layers are also very important [116].

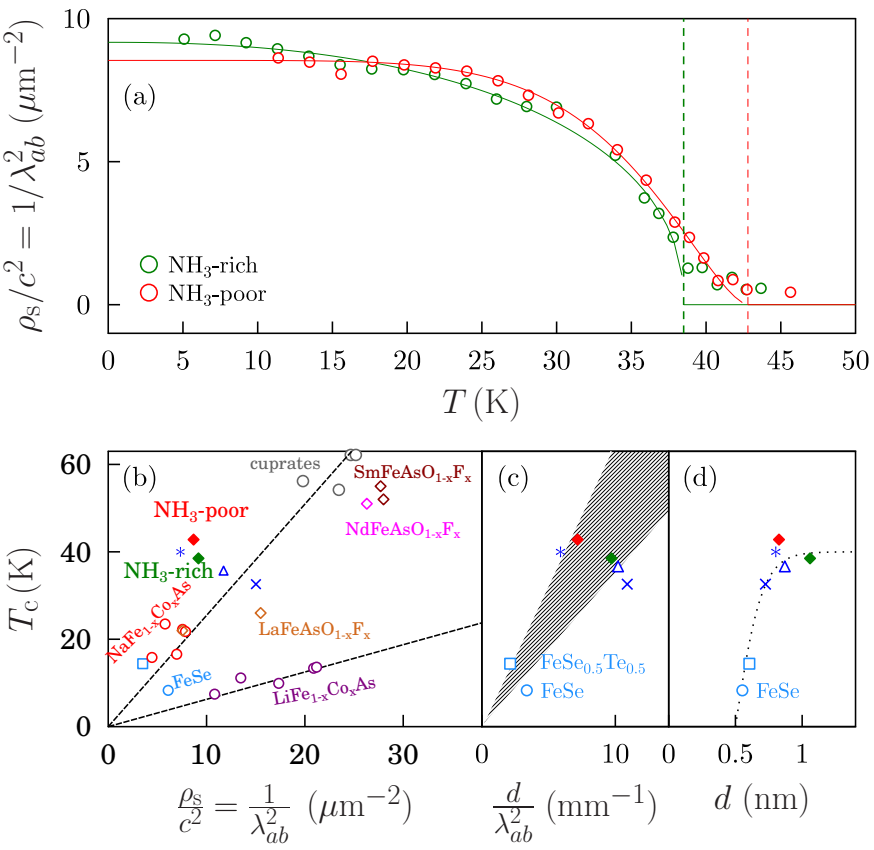

Figure 5.19: (a) The temperature dependence of the superfluid stiffness $\rho_s = c^2/\lambda_{ab}^2$. (b) The Uemura plot correlates T_c with ρ_s for a variety of superconductors [117, 151, 152, 153, 154, 155, 158, 159, 160]. Compounds with FeSe layers (including $\times$=$Rb_{0.77}Fe_{1.61}Se_2$ [159], $*$=$Sr_{0.3}(NH_2)_y(NH_3)_{1-y}Fe_2Se_2$ [117], $\triangle$=$Li(C_5H_5N)_{0.2}Fe_2Se_2$ [160]) are also plotted as a function of (c) d/λ_{ab}^2 (shaded area indicates region of approximate correlation) and (d) layer spacing d (dotted curve is a guide to the eye).

5.4.5 Conclusion

In this section I have presented a study on the superconducting properties in ammonia-poor and ammonia-rich intercalated $Li_x[(NH_2)_y(NH_3)_{1-y}]_zFe_2Se_2$ ($z = 1, 2$). The reactions were carried out *in situ* on the muon beamline so that the superfluid stiffness could be measured using TF μSR on a single sample. The charging and discharging of ammonia was found to produce two distinct superconducting phases with different bulk responses, but a similar superconducting fraction of ≈ 0.5. In agreement with previous measurements by Burrard-Lucas *et al.*, the critical temperatures were found

to be 42.8(9) K and 38.5(3) K for the NH_3-poor and NH_3-rich phases, respectively. The temperature dependence of $B_{\mathrm{rms}}(T)$ as measured by μSR can give some indication of the type of band structure in these materials. Unlike previous compounds, neither phase exhibit a further increase of B_{rms} at low T, although this could not be ruled out completely in the case of the NH_3-poor phase as data at $T < 10\,\mathrm{K}$ were omitted due to poor thermal stabilisation. This suggests single-band rather than multiband behaviour, as previously measured, although a definitive conclusion about the band structure must await a detailed study of the temperature dependence of H_{c2} in these materials. The data indicate similar penetration depths between the two phases, and a combination of analysis techniques in both the time and field domains has allowed a more accurate approximation of the superfluid stiffness ($\rho_{\mathrm{s}}(0) = 9.2(2)\,\mu\mathrm{m}^{-2}$ for NH_3-rich and $\rho_{\mathrm{s}}(0) = 8.7(1)\,\mu\mathrm{m}^{-2}$ for NH_3-poor phases, respectively). Whilst these values do generally agree with the Uemura trend line, the superfluid stiffness is slightly lower than expected, which may indicate some degree of 'dirtiness'. It is clear that repeat measurements at low T are necessary to gain a better understanding of these superconducting properties and in particular to further investigate the possibility of two-gap behaviour.

5.5 Superconductivity in LiFeP

5.5.1 Background

LiFeP is another Fe-based layered material in which superconductivity is mediated by FeP layers with a T_{c} of up to 6 K [161]. It was the first '111' type iron pnictide found to contain no arsenic and shares the same crystal structure, as well as similar Fermi surface shapes as its higher transition temperature analogue LiFeAs [162, 163] ($T_{\mathrm{c}} \approx 18\,\mathrm{K}$). However, in addition to the significantly lower T_{c}, LiFeP is found to

exhibit several important properties that are different from other materials in the '111'-type family of superconductors. For example, magnetotransport measurements indicate weaker electronic correlations than that of LiFeAs [164], which although consistent with the observed smaller H_{c2} (LiFeP has a factor of 70 smaller H_{c2} than its arsenic counterpart), its behaviour is inconsistent with the general consensus that stronger correlations favour unconventional superconductivity. One of the most significant findings is the difference in the superconducting gap structure. For LiFeAs, penetration depth measurements indicate a T^3 temperature dependence [165], which is characteristic of fully gapped behaviour. On the other hand, studies indicate a linear temperature dependence in LiFeP down to $T/T_c = 0.03$ which is evidence for a nodal superconducting gap [166, 167]. The diversity across the pnictides is in contrast to the cuprates, which are all found to have the same type of nodal pairing state. It is believed that understanding the non-universality of these superconducting gap structures is key to unearthing the mechanism of this unconventional superconductivity.

μSR has been successfully applied to LiFeAs and its derivative compounds to measure their superconducting properties [140, 141, 168]. Studies indicate enhanced superfluid stiffnesses over that which would be expected on the basis of transition temperatures, which on the Uemura plot places them away from the general scaling relation (unlike that observed in the FeSe derivatives described previously). Furthermore, ZF μSR has also proven useful in ruling out or confirming candidate theories for the superconducting mechanism, such as triplet pairing. This phenomenon may be associated with spontaneous time-reversal symmetry breaking which can induce small magnetic fields that are detectable in ZF μSR. Whilst this has been observed in some materials such as Sr_2RuO_4 [169] and $LaNiC_2$ [170], a recent study on LiFeAs [168] shows no signatures of triplet pairing. In this section I shall present a μSR experiment to measure the penetration depth and hence superfluid stiffness of LiFeP to confirm the superconducting behaviour in relation to the Uemura scaling line.

5.5.2 Experimental Method

Sample synthesis and characterisation were carried out by S. J. Clarke and co workers. μSR measurements were performed on the MuSR spectrometer by myself with the assistance of S. J. Blundell, F. Lang and P. J. Baker. The powdered sample was placed inside a Ag-foil packet of $\sim 12.5\,\mu$m foil thickness and mounted onto a silver backing plate surrounded by a heamatite mask. The sample was cooled in a transverse field of 10 mT and the data were collected in the temperature range 0.3–13 K. Preliminary TF measurements were also carried out on the GPS spectrometer at PSI.

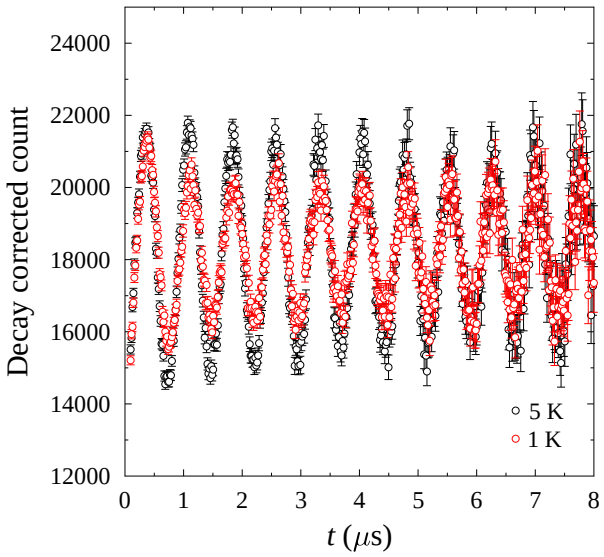

Figure 5.20: Example raw spectra of LiFeP measured by a single bank of detectors on the MuSR spectrometer in a transverse field of 10 mT at 5 K (black points) and 1 K (red points).

5.5.3 Results

The data were fitted in the time-domain assuming the usual Gaussian distribution of local fields described by Eq. 5.1. As in the previous case, temperature-independent

values of B_{bg}, σ_{bg} and ϕ were extracted first by fitting the normal phase with the background component only, before a final fit was performed using averaged values of A_{bg} and A_{VL}. The lower bound for the superconducting fraction is found to be $A_{\mathrm{VL}}/(A_{\mathrm{VL}} + A_{\mathrm{bg}}) \approx 0.4$. The results of these fits are shown in Fig. 5.21 and we observe a clear diamagnetic shift below a critical temperature of $T_{\mathrm{c}} = 3.9(1)\,\mathrm{K}$. This is slightly lower than that reported by other studies, although this is likely due to sample variation. The field width and diamagnetic shift are fitted by the usual phenomenological functions given by Eq. 5.4 and Eq. 5.5 and these results are shown in Table 5.3 and Table 5.4.

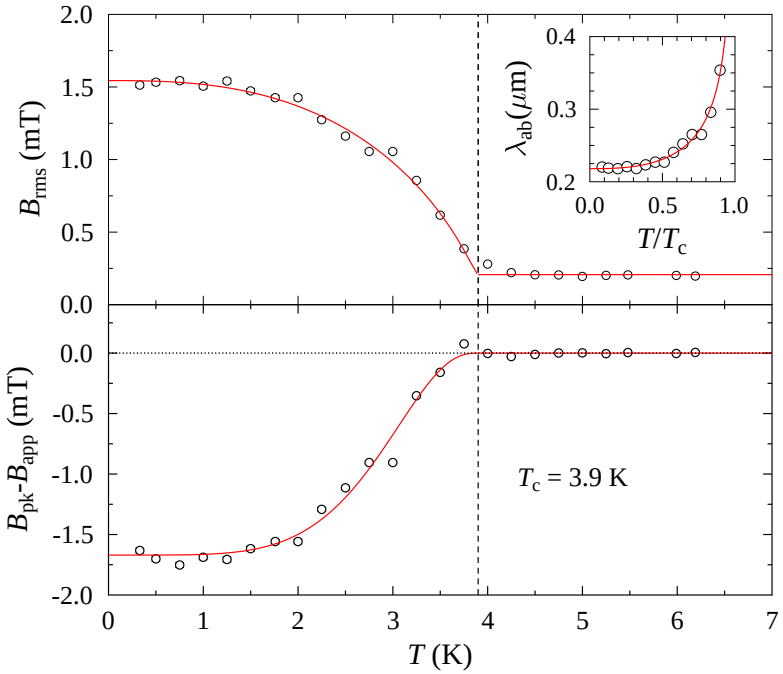

Figure 5.21: The mean field width B_{rms} and diamagnetic shift $B_{\mathrm{pk}} - B_{\mathrm{app}}$ of LiFeP measured in a transverse field of 10 mT. Fits are to the usual phenomenological functions Eq. 5.4 and Eq. 5.5. Inset shows the temperature dependence of the in-plane penetration depth λ_{ab}

Interestingly, the in-plane penetration depth $\lambda_{\mathrm{ab}}(0) = 0.218(3)\,\mathrm{nm}$ is significantly higher than that reported by Hashimoto *et al.* ($\approx 150\,\mu\mathrm{m}$) [167]. Additionally, this same study suggests a T-linear dependence of the superfluid stiffness, whereas these

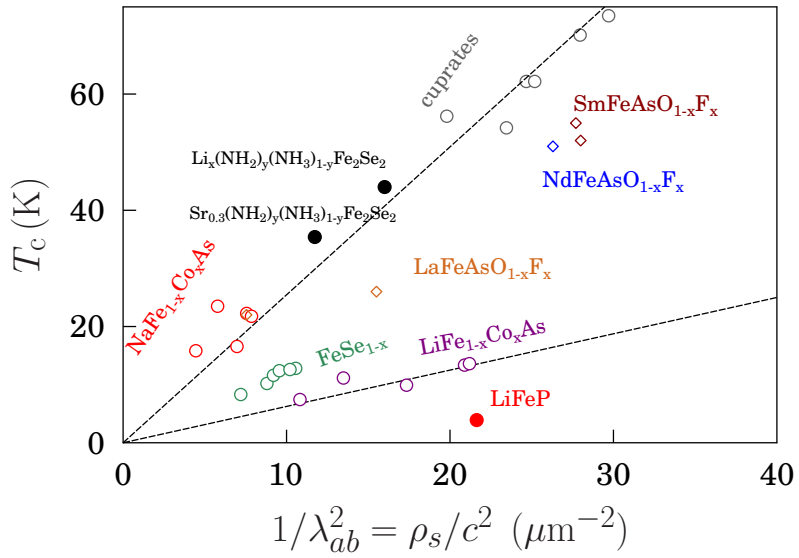

Figure 5.22: The Uemura plot; LiFeP (red circle) exhibits an enhanced superfluid stiffness in relation to its transition temperature, similar to that of the arsenic conaining pnictides (purple circles).

Sample	T_c (K)	$\lambda_{ab}(0)$ (μm)	B_0 (mT)	B_{dip} (mT)	α	β
LiFeP	3.9(1)	0.218(3)	1.53(5)	0.207(6)	2.7(8)	0.69(23)

Table 5.3: The critical temperature, in-plane penetration depth and fitted parameters of LiFeP with statistical errors. Values are extracted from TF data using Eq. 5.4 to model B_{rms}.

measurements suggest a non-linear T behaviour. These differences may simply be due to sample variation, for example due to these compounds being polycrystalline and not single crystals, as in the study by Hashimoto *et al.*. Furthermore, for our data we find that the relationship $(B_{app} - B_{pk})/B_0 \approx 0.6$ [149] does not hold, and instead we observe a ratio closer to ≈ 1, although the reason for this is not yet clear. Discrepancies could also arise due to difference in measurement technique. In this case, μSR is a bulk measurement, whereas the tunnel diode oscillator (TDO) technique used in Ref. [167] utilises microwave penetration and hence is potentially more sensitive to surface effects. Note that the TDO technique cannot directly measure $\lambda(0)$ and so

Sample	T_c (K)	B_{dia} (mT)	α‘	β‘
LiFeP	3.9(1)	1.67(1)	4.9(7)	2.8(6)

Table 5.4: The critical temperature and fitted parameters of LiFeP with statistical errors extracted using Eq. 5.5 to model B_{dia} (T_c is fixed from fits of $B_{rms}(T)$).

the value reported in [167] is estimated from the known value for LiFeAs (measured using small angle neutron scattering) which is scaled according to the difference between the effective mass of the two superconductors. Therefore, one could argue that these μSR measurements could provide a more accurate estimate of $\lambda(0)$ and hence the superfluid stiffness. A Uemura plot of ρ_s against T_c in Fig. 5.22, indicates an enhanced superfluid stiffness, as in the case of the $LiFe_{1-x}Co_xAs$ compounds [140], with a significantly lower T_c.

Chapter 6

Conclusion

Condensed matter physics is a highly diverse area of research that is often driven by the search for new materials with unexpected properties. In this thesis I concentrate on two of its most active areas of interest in recent years, namely, high-T superconductivity and unconventional magnetism. In particular, I have investigated a range of novel materials using a combination of μSR and pulsed-field magnetometry techniques. These experiments have been motivated by the desire for improving our fundamental understanding of these materials, as well as the prospect of advancing a range of technological applications. The key results are summarised in the following.

Chapter 2 describes the main measurement techniques used in this thesis. I have demonstrated the use of the proximity detector oscillator as a susceptometer in high magnetic fields for probing the H-T phase diagram of the dimer material $[Cu(pyz)(gly)]ClO_4$. This work formed part of a study published in Ref. [23] which showed how the system undergoes a field-induced phase transition to an XY antiferromagnetic phase that is reminiscent of the Bose-Einstein condensation of magnons. These findings demonstrate the potential of using coordination polymers as a means of probing exotic magnetic phenomena of quantum mechanical systems that are rarely observed in more conventional materials.

Chapter 3 presents a μSR study of a family of insulating candidate quantum spin ices $Pr_2B_2O_7$ (B = Sn, Zr and Hf), whose Pr^{3+} ion contains a non-Kramers doublet ground state. This work has been published in Ref. [52]. Instead of dynamic electronic behaviour, our measurements indicate a relaxation that is typical of static nuclear spins, albeit with a strong temperature dependence. Furthermore, the measured moment at low temperatures appears to be much larger than expected for ^{141}Pr nuclear moments. We attribute this to a hyperfine enhancement of the Pr nuclear moments, as in the case of the metallic spin liquid $Pr_2Ir_2O_7$ [50, 51], which requires a singlet ground-state. Using DFT and CF calculations, we have identified the muon implantation sites in these pyrochlores and demonstrate how the non-Kramers doublet of nearby Pr ions is split by a highly anisotropic distortion field of the implanted muon, and provide a quantitative relationship between this effect and the measured temperature dependence of the muon relaxation.

Although there has been previous evidence for a muon-induced effect in Pr-containing systems with a non-Kramers doublet, this is the first time the nature of these effects has been explored in a detailed, quantitative way. Thus, this work presents a definite contribution towards the advancement of the μSR technique in the context of pyrochlore oxides, which will enable future work in the area to be carried out with a better understanding of the physical processes involved in these experiments. Here, we have identified a worst-case scenario in which the measure response is dominated by the muon-induced distortion of the local structure and its effect on the crystal field levels of nearby magnetic ions. Our work implies that in any oxide there will always be an anisotropic distortion field around the implanted muon and its effect should always be considered, particularly in the case of high-symmetry non-Kramers ground states, which are most susceptible to these perturbations.

In Chapter 4 I present a μSR study on the classical spin ice $Ho_2Ti_2O_7$. These results show that unlike in the case of $Dy_2Ti_2O_7$, there is no recovery of the $t = 0$ muon

asymmetry when cooling down to 20 mK. This rules out any quasi-static electronic fluctuations in the frozen regime within the time frame of μSR. I also demonstrate a first attempt to systematically relate the ZF relaxation rate in both compounds to the calculated crystal field levels after taking in account the effect of a muon-induced perturbation in the nearest-neighbour Ho^{3+}/Dy^{3+} ions. DFT calculations show these levels to be altered in a similar way to that observed in the Pr-based pyrochlore oxides. The effective activation energy which is extracted from ZF μSR measurements shows that the muon relaxation is dominated by ions that are situated further away from the implantation site, and whose crystal environments are largely unaffected by the muon electric field. This is facilitated by the large moments of Ho^{3+}/Dy^{3+} which allow muons to couple more strongly with distant ions. Although more work is needed to obtain full quantitative agreement between the CF energy levels and observed muon relaxation rates, this study does highlight a key result; namely that the muon-induced distortion in these compounds has minimal effect on the measured response, even for the non-Kramers ion Ho^{3+}.

Finally, in Chapter 5, I present a series of studies on three Fe-based superconductors. μSR measurements on LiFeP indicate a $T_c = 3.9$ K and an in-plane penetration depth $\lambda_{ab}(0) = 0.218(3)$ nm that is significantly higher than that reported by previous work [167]. This places LiFeP on the Uemura plot with an enhanced superfluid stiffness similar to that observed in the $LiFe_{1-x}Co_xAs$ family. I also discuss the superconducting properties of recently discovered $Sr_{0.3}(NH_2)_y$-$(NH_3)_{1-y}Fe_2Se_2$ measured using pulsed-field magnetometry and μSR. This work formed part of a collaborative effort that is published in Ref. [117]. We show how intercalation of Sr atoms together with amide and ammonia introduces intrinsic stacking disorder in this compound due to a random stacking of the FeSe layers along the c-axis, which is not present in other intercalates of the same family. Our interpretation of the structural data is that despite the random stacking, the well-separated FeSe layers themselves remain

well ordered, which preserves the superconducting state in these systems. In pulsed magnetic fields, the upper critical field was found to increase upon cooling with an upwards curvature that is commonly seen in other type-II superconductors of a multi-band nature. Fitting the data to a two-band model, we extract a maximum upper critical field of $\mu_0 H_{c2}(0) \approx 33(2)\,\mathrm{T}$. TF μSR measurements indicate a clear superconducting transition with diamagnetic shift at $T_\mathrm{c} \approx 36\,\mathrm{K}$. This work demonstrates that robust superconductivity does not rely on perfect structural coherence along the c-axis.

Lastly, μSR measurements were also performed on $\mathrm{Li}_x[(\mathrm{NH}_2)_y(\mathrm{NH}_3)_{1-y}]_z\mathrm{Fe}_2\mathrm{Se}_2$ ($z = 1, 2$) to study the effect on the superconducting properties of intercalating additional ammonia, via reversible adsorption and desorption. The charging and discharging of ammonia was found to produce two distinct superconducting phases with different bulk responses, but a similar superconducting fraction of ≈ 0.5. These reactions were carried out *in situ* on the muon beamline such that the superfluid stiffness could be measured using TF μSR on a single sample. We extract transition temperatures of 38.5(3) K and 43(1) K for the ammonia-rich and ammonia-poor phases, respectively, which agree well with previous magnetic measurements. However, unlike previous compounds neither phase show evidence of multiband behaviour at low T, although this could not be ruled out completely in the case of the NH_3-poor phase, and repeat experiments of low T behaviour are needed to further investigate this. A subject for further study includes a detailed measurement of the upper critical field H_c using the pulsed magnetic field technique described in this thesis, which will allow a more definitive conclusion about the band structure in these materials. Overall, this *in situ* technique provides a valuable contribution to the field of μSR and it is hoped that it will be applied more widely to study other *in situ* solid-state reactions, intercalation processes or even spin crossover phenomena.

Bibliography

[1] M. J. Harris, S. T. Bramwell, D. F. McMorrow, T. Zeiske and K. W. Godfrey. *Phys. Rev. Lett.* **79**, 2554–2557 (1997). 1, 38, 63

[2] S. T. Bramwell and M. J. P. Gingras. *Science* **294**, 1495–1501 (2001). 1, 38

[3] H. Takahashi, K. Igawa, K. Arii, Y. Kamihara, M. Hirano and H. Hosono. *Nature* **453**, 376–378 (2008). 1, 78

[4] S. J. Blundell. *Contemp. Phys.* **40**, 175–192 (1999). 4, 7, 8, 13, 14, 15

[5] S. F. J. Cox. *J. Phys. C: Solid State Phys.* **20**, 3187 (1987). 4, 7

[6] S. Blundell. *Magnetism in condensed matter* (Oxford Univ. Press, 2001). 6, 8

[7] R. L. Garwin, L. M. Lederman and M. Weinrich. *Phys. Rev.* **105**, 1415–1417 (1957). 9

[8] F. Pratt. *Physica B: Cond. Mat.* **289290**, 710 – 714 (2000). 11

[9] Triumf. http://cmms.triumf.ca/intro/musr/muSRBrochure.pdf. Accessed: 27/10/2015. 11

[10] R. Kubo, T. Toyabe and R. Blinc. *North-Holland, Amsterdam, 1967) p* **810** (1967). 12

[11] R. S. Hayano, Y. J. Uemura, J. Imazato, N. Nishida, T. Yamazaki and R. Kubo. *Phys. Rev. B* **20**, 850–859 (1979). 12

[12] R. E. Walstedt and L. R. Walker. *Phys. Rev. B* **9**, 4857–4867 (1974). 12

[13] S. J. Möller. *Muon-spin relaxation and its application in the study of molecular quantum magnets* (D. Phil, University of Oxford, 2013). 13

[14] Isis facility, musr user manual. http://www.isis.stfc.ac.uk/instruments/musr/documents/musr_manual6543.pdf (2011). Accessed: 06/04/2016. 18

[15] P. More, G. Aeppli, M. Aronson *et al. Opportunities in high magnetic field science* (The National Academies Press, 2004). 19

[16] H. Witte and H. Jones. *Physica B: Cond. Mat.* **346347**, 663 – 667 (2004). Proceedings of the 7th International Symposium on Research in High Magnetic Fields. 19

[17] A. Mari and L. Brossard. *Rev. Sci. Instrum.* **64** (1993). 21

[18] P. A. Goddard, J. Singleton, P. Sengupta, R. D. McDonald, T. Lancaster, S. J. Blundell, F. L. Pratt, S. Cox, N. Harrison, J. L. Manson, H. I. Southerland and J. A. Schlueter. *New Journal of Physics* **10**, 083025 (2008). 21

[19] E. Ohmichi, E. Komatsu and T. Osada. *Rev. Sci. Instrum.* **75** (2004). 22

[20] S. Ghannadzadeh, M. Coak, I. Franke, P. A. Goddard, J. Singleton and J. L. Manson. *Rev. Sci. Instrum.* **82** (2011). 22, 23, 24, 25, 26

[21] M. M. Altarawneh, C. H. Mielke and J. S. Brooks. *Rev. Sci. Instrum.* **80**, – (2009). 23, 24, 25

[22] S. Ghannadzadeh. *Investigating magnetism and superconductivity using high magnetic fields* (D. Phil, University of Oxford, 2014). 24

[23] T. Lancaster, P. A. Goddard, S. J. Blundell, F. R. Foronda, S. Ghannadzadeh *et al. Phys. Rev. Lett.* **112**, 207201 (2014). 27, 28, 31, 120

[24] P. A. Goddard, J. L. Manson, J. Singleton, I. Franke, T. Lancaster, A. J. Steele, S. J. Blundell, C. Baines, F. L. Pratt, R. D. McDonald, O. E. Ayala-Valenzuela, J. F. Corbey, H. I. Southerland, P. Sengupta and J. A. Schlueter. *Phys. Rev. Lett.* **108**, 077208 (2012). 27

[25] T. Giamarchi, C. Rüegg and O. Tchernyshyov. *Nature Physics* **4**, 198–204 (2008). 27, 29, 33

[26] V. Zapf, M. Jaime and C. D. Batista. *Rev. Mod. Phys.* **86**, 563–614 (2014). 27, 33

[27] B. Bleaney and K. D. Bowers. *Proc. R. Soc. London Ser. A* **214**, 451–465 (1952). 28

[28] A. J. Steele, T. Lancaster, S. J. Blundell, P. J. Baker, F. L. Pratt, C. Baines, M. M. Conner, H. I. Southerland, J. L. Manson and J. A. Schlueter. *Phys. Rev. B* **84**, 064412 (2011). 31

[29] M. Tachiki and T. Yamada. *J. Phys. Soc. Jpn.* **28**, 1413–1425 (1970). 31

[30] T. Giamarchi and A. M. Tsvelik. *Phys. Rev. B* **59**, 11398–11407 (1999). 31, 33

[31] T. Nikuni, M. Oshikawa, A. Oosawa and H. Tanaka. *Phys. Rev. Lett.* **84**, 5868–5871 (2000). 33

[32] Quantum Design USA. www.qdusa.com. 34

[33] L. H. Lewis and K. M. Bussmann. *Rev. Sci. Instrum.* **67** (1996). 35

[34] A. Ramirez. *Annual Review of Materials Science* **24**, 453–480 (1994). 36

[35] W. F. Giauque and M. F. Ashley. *Phys. Rev.* **43**, 81–82 (1933). 37

[36] W. F. Giauque and J. W. Stout. *Journal of the American Chemical Society* **58**, 1144–1150 (1936). 37

[37] L. Pauling. *Journal of the American Chemical Society* **57**, 2680–2684 (1935). 37

[38] J. D. Bernal and R. H. Fowler. *The Journal of Chemical Physics* **1** (1933). 37

[39] C. Castelnovo, R. Moessner and S. L. Sondhi. *Nature* **451**, 42–45 (2008). 38

[40] J. S. Gardner, M. J. P. Gingras and J. E. Greedan. *Rev. Mod. Phys.* **82**, 53–107 (2010). 38

[41] J. S. Gardner, S. R. Dunsiger, B. D. Gaulin, M. J. P. Gingras, J. E. Greedan, R. F. Kiefl, M. D. Lumsden, W. A. MacFarlane, N. P. Raju, J. E. Sonier, I. Swainson and Z. Tun. *Phys. Rev. Lett.* **82**, 1012–1015 (1999). 39

[42] K. A. Ross, L. Savary, B. D. Gaulin and L. Balents. *Phys. Rev. X* **1**, 021002 (2011). 39

[43] M. J. P. Gingras and P. A. McClarty. *Rep. Prog. Phys.* **77**, 056501 (2014). 39

[44] S. Onoda and Y. Tanaka. *Phys. Rev. Lett.* **105**, 047201 (2010). 39

[45] H. D. Zhou, C. R. Wiebe, J. A. Janik, L. Balicas, Y. J. Yo, Y. Qiu, J. R. D. Copley and J. S. Gardner. *Phys. Rev. Lett.* **101**, 227204 (2008). 39

[46] O. Benton, O. Sikora and N. Shannon. *Phys. Rev. B* **86**, 075154 (2012). 39

[47] S. Lee, S. Onoda and L. Balents. *Phys. Rev. B* **86**, 104412 (2012). 39

[48] S. Nakatsuji, Y. Machida, Y. Maeno, T. Tayama, T. Sakakibara, J. v. Duijn, L. Balicas, J. N. Millican, R. Macaluso and J. Y. Chan. *Phys. Rev. Lett.* **96**, 087204 (2006). 39, 45, 46

[49] Y. Tokiwa, J. Ishikawa, S. Nakatsuji and P. Gegenwart. *Nature Materials* **13**, 356–359 (2014). 39

[50] D. MacLaughlin, Y. Ohta, Y. Machida, S. Nakatsuji, G. Luke, K. Ishida, R. Heffner, L. Shu and O. Bernal. *Physica B: Cond. Mat.* **404**, 667 – 670 (2009). 39, 43, 44, 46, 121

[51] D. E. MacLaughlin, Y. Nambu, Y. Ohta, Y. Machida, S. Nakatsuji and O. O. Bernal. *J. Phys.: Conf. Ser.* **225**, 012031 (2010). 39, 43, 44, 121

[52] F. R. Foronda, F. Lang, J. S. Möller, T. Lancaster, A. T. Boothroyd, F. L. Pratt, S. R. Giblin, D. Prabhakaran and S. J. Blundell. *Phys. Rev. Lett.* **114**, 017602 (2015). 40, 121

[53] A. J. Princep and Prabh. *Phys. Rev. B* **88**, 104421 (2013). 44, 49

[54] K. Kimura, S. Nakatsuji, J. Wen, C. Broholm, M. Stone, E. Nishibori and H. Sawa. *Nature communications* **4** (2013). 44

[55] R. Feyerherm, A. Amato, A. Grayevsky, F. Gygax, N. Kaplan and A. Schenck. *Z. Phys. B* **99**, 3–13 (1995). 44

[56] T. Tashma, A. Amato, A. Grayevsky, F. N. Gygax, M. Pinkpank, A. Schenck and N. Kaplan. *Phys. Rev. B* **56**, 9397–9405 (1997). 44

[57] L. Savary, E.-G. Moon and L. Balents. *Phys. Rev. X* **4**, 041027 (2014). 45

[58] R. M. Martin. *Electronic Structure* (Cambridge University Press, 2004). 46

[59] P. Giannozzi, S. Baroni, N. Bonini, M. Calandra, R. Car *et al. J. Phys.: Condens. Matter* **21**, 395502 (2009). 46

[60] M. L. Amig, V. A. Crivillero, D. G. Franco and G. Nieva. *J. Phys.: Conference Series* **568**, 022005 (2014). 46, 98

[61] J. S. Möller, D. Ceresoli, T. Lancaster, N. Marzari and S. J. Blundell. *Phys. Rev. B* **87**, 121108 (2013). 46

[62] F. Bernardini, P. Bonfà, S. Massidda and R. De Renzi. *Phys. Rev. B* **87**, 115148 (2013). 46

[63] S. J. Blundell, J. S. Möller, T. Lancaster, P. J. Baker, F. L. Pratt, G. Seber and P. M. Lahti. *Phys. Rev. B* **88**, 064423 (2013). 46

[64] B. J. Kennedy, B. A. Hunter and C. J. Howard. *J. Solid State Chem.* **130**, 58–65 (1997). 47

[65] F. Lang. *DPhil Thesis* (University of Oxford, 2016). 47

[66] B. Bleaney. *Physica* **69**, 317 – 329 (1973). 49, 51

[67] V. Vrankovic, A. Gabard, I. Meier, R. Stutz, R. Deckardt, S. Sanfilippo, R. Scheuermann, K. Sedlak, D. Reggiani, K. Deiters, T. Rauber, P. Kaufmann and H. Walther. *IEEE Transactions on Applied Superconductivity* **22**, 4101204–4101204 (2012). 53

[68] A. Stoykov, R. Scheuermann, K. Sedlak, J. Rodriguez, U. Greuter and A. Amato. *Physics Procedia* **30**, 7 – 11 (2012). 12th International Conference on Muon Spin Rotation, Relaxation and Resonance. 53

[69] K. Matsuhira, Y. Hinatsu, K. Tenya, H. Amitsuka and T. Sakakibara. *J. Phys. Soc. Jpn.* **71**, 1576–1582 (2002). 63

[70] B. C. den Hertog and M. J. P. Gingras. *Phys. Rev. Lett.* **84**, 3430–3433 (2000). 63

[71] M. Kanada, Y. Yasui, Y. Kondo, S. Iikubo, M. Ito, H. Harashina, M. Sato, H. Okumura, K. Kakurai and H. Kadowaki. *J. Phys. Soc. Jpn.* **71**, 313–318 (2002). 63, 64

[72] S. T. Bramwell, M. J. Harris, B. C. den Hertog, M. J. P. Gingras, J. S. Gardner, D. F. McMorrow, A. R. Wildes, A. L. Cornelius, J. D. M. Champion, R. G. Melko and T. Fennell. *Phys. Rev. Lett.* **87**, 047205 (2001). 64

[73] T. Fennell, O. Petrenko, G. Balakrishnan, S. Bramwell, J. Champion, B. Fåk, M. Harris and D. M. Paul. *Appl. Phys. A* **74**, s889–s891 (2002). 64

[74] H. Fukazawa, R. G. Melko, R. Higashinaka, Y. Maeno and M. J. P. Gingras. *Phys. Rev. B* **65**, 054410 (2002). 64

[75] A. L. Cornelius and J. S. Gardner. *Phys. Rev. B* **64**, 060406 (2001). 64

[76] O. A. Petrenko, M. R. Lees and G. Balakrishnan. *Phys. Rev. B* **68**, 012406 (2003). 64

[77] J. Snyder, J. Slusky, R. Cava and P. Schiffer. *Nature* **413**, 48–51 (2001). 64

[78] K. Matsuhira, Y. Hinatsu and T. Sakakibara. *J. Phys.: Condens. Matter* **13**, L737 (2001). 64

[79] J. Lago, S. J. Blundell and C. Baines. *J. Phys.: Condens. Matter* **19**, 326210 (2007). 64, 65, 68, 74, 75

[80] S. Rosenkranz, A. P. Ramirez, A. Hayashi, R. J. Cava, R. Siddharthan and B. S. Shastry. *J. Appl. Phys.* **87** (2000). 64

[81] K. Matsuhira, C. Paulsen, E. Lhotel, C. Sekine, Z. Hiroi and S. Takagi. *J. Phys. Soc. Jpn.* **80**, 123711 (2011). 64

[82] G. Ehlers, A. L. Cornelius, M. Orendc, M. Kajnakov, T. Fennell, S. T. Bramwell and J. S. Gardner. *J. Phys.: Condens. Matter* **15**, L9 (2003). 64

[83] K. Matsuhira, Y. Hinatsu, K. Tenya and T. Sakakibara. *J. Phys.: Condens. Matter* **12**, L649 (2000). 65

[84] J. Snyder, B. G. Ueland, J. S. Slusky, H. Karunadasa, R. J. Cava and P. Schiffer. *Phys. Rev. B* **69**, 064414 (2004). 65

[85] M. Harris, S. Bramwell, T. Zeiske, D. McMorrow and P. King. *J. Magn. Magn. Mater.* **177181, Part 2**, 757 – 762 (1998). International Conference on Magnetism (Part II). 65

[86] S. R. Dunsiger, R. F. Kiefl and J. S. Gardner. *TRIUMF Annual Report* (2000). 65, 68

[87] S. Bramwell, S. Giblin, S. Calder, R. Aldus, D. Prabhakaran and T. Fennell. *Nature* **461**, 956–959 (2009). 69

[88] R. Orbach. *Proceedings of the Physical Society* **77**, 821 (1961). 72

[89] C. Castelnovo, R. Moessner and S. L. Sondhi. *Phys. Rev. B* **84**, 144435 (2011). 75

[90] W. Meissner and R. Ochsenfeld. *Naturwissenschaften* **21**, 787–788 (1933). 77

[91] F. London and H. London. *Proc. R. Soc. London Ser. A* **149**, 71–88 (1935). 77

[92] L. Shubnikov, V. Khotkevich, D. Shepelev Yu and N. Riabinin Yu. *Zh. Eksp. Teor. Fiz* **7**, 221–237 (1937). 77

[93] G. Shepelev. *Magnetic properties of superconducting alloys*. Ph.D. thesis, PhD Thesis (Kharkov State Univ.) (1938). 77

[94] J. Bardeen, L. N. Cooper and J. R. Schrieffer. *Phys. Rev.* **108**, 1175–1204 (1957). 77

[95] J. G. Bednorz and K. A. Müller. *Zeitschrift für Physik B Condensed Matter* **64**, 189–193 (1986). 78

[96] A. Schilling, M. Cantoni, J. Guo and H. Ott. *Nature* **363**, 56–58 (1993). 78

[97] Y. Kamihara, T. Watanabe, M. Hirano and H. Hosono. *J. Am. Chem. Soc.* **130**, 3296–3297 (2008). 78, 103

[98] J. D. Wright. *Magnetism and superconductivity in iron pnictides and iron chalco- genides* (D. Phil, University of Oxford, 2013). 79

[99] X. Zhu, F. Han, G. Mu, B. Zeng, P. Cheng, B. Shen and H.-H. Wen. *Phys. Rev. B* **79**, 024516 (2009). 79

[100] J. Paglione and R. L. Greene. *Nature Physics* **6**, 645–658 (2010). 80

[101] T. Park, E. Park, H. Lee, T. Klimczuk, E. D. Bauer, F. Ronning and J. D. Thompson. *J. Phys.: Condens. Matter* **20**, 322204 (2008). 79

[102] C.-H. Lee, A. Iyo, H. Eisaki, H. Kito, M. T. Fernandez-Diaz, T. Ito, K. Kihou, H. Matsuhata, M. Braden and K. Yamada. *J. Phys. Soc. Jpn.* **77**, 083704 (2008). 79

[103] D. C. Johnston. *Advances in Physics* **59**, 803–1061 (2010). 80, 81

[104] D. Basov and A. V. Chubukov. *Nature Physics* **7**, 272–276 (2011). 81

[105] P. J. Hirschfeld, M. M. Korshunov and I. I. Mazin. *Rep. Prog. Phys.* **74**, 124508 (2011). 80

[106] I. I. Mazin, D. J. Singh, M. D. Johannes and M. H. Du. *Phys. Rev. Lett.* **101**, 057003 (2008). 80

[107] T. M. McQueen, Q. Huang, V. Ksenofontov, C. Felser, Q. Xu, H. Zandbergen, Y. S. Hor, J. Allred, A. J. Williams, D. Qu, J. Checkelsky, N. P. Ong and R. J. Cava. *Phys. Rev. B* **79**, 014522 (2009). 82, 108

[108] A. Krzton-Maziopa, E. V. Pomjakushina, V. Y. Pomjakushin, F. von Rohr, A. Schilling and K. Conder. *J. Phys.: Condens. Matt.* **24**, 382202 (2012). 82

[109] M. Burrard-Lucas, D. G. Free, S. J. Sedlmaier, J. D. Wright, S. J. Cassidy, Y. Hara, A. J. Corkett, T. Lancaster, P. J. Baker, S. J. Blundell *et al. Nature Materials* **12**, 15–19 (2013). 82, 83, 88, 102, 103, 104, 107, 108, 109, 112

[110] T. Ying, X. Chen, G. Wang, S. Jin, T. Zhou, X. Lai, H. Zhang and W. Wang. *Sci. Rep.* **2** (2012). 82

[111] T. Noji, T. Hatakeda, S. Hosono, T. Kawamata, M. Kato and Y. Koike. *Physica C: Superconductivity* **504**, 8 – 11 (2014). Proceedings of the 26th International Symposium on Superconductivity. 82, 112

[112] H. Sun, D. N. Woodruff, S. J. Cassidy, G. M. Allcroft, S. J. Sedlmaier *et al. Inorg. Chem.* **54**, 1958–1964 (2015). 82

[113] U. Pachmayr, F. Nitsche, H. Luetkens, S. Kamusella, F. Brckner, R. Sarkar, H.-H. Klauss and D. Johrendt. *Angew. Chem. Inter. Ed.* **54**, 293–297 (2015). 82

[114] X. Lu, N. Wang, H. Wu, Y. Wu, D. Zhao, X. Zeng, X. Luo, T. Wu, W. Bao, G. Zhang *et al. Nature Materials* **14** (2014). 82

[115] T. Hatakeda, T. Noji, T. Kawamata, M. Kato and Y. Koike. *J. Phys. Soc. Jpn.* **82**, 123705 (2013). 82

[116] D. Guterding, H. O. Jeschke, P. J. Hirschfeld and R. Valentí. *Phys. Rev. B* **91**, 041112 (2015). 82, 112

[117] F. R. Foronda, S. Ghannadzadeh, S. J. Sedlmaier, J. D. Wright, K. Burns, S. J. Cassidy, P. A. Goddard, T. Lancaster, S. J. Clarke and S. J. Blundell. *Phys. Rev. B* **92**, 134517 (2015). 82, 107, 112, 113, 122

[118] E.-W. Scheidt, V. Hathwar, D. Schmitz, A. Dunbar, W. Scherer, F. Mayr, V. Tsurkan, J. Deisenhofer and A. Loidl. *Eur. Phys. J. B* **85** (2012). 82, 105

[119] S. J. Sedlmaier, S. J. Cassidy, R. G. Morris, M. Drakopoulos, C. Reinhard, S. J. Moorhouse, D. OHare, P. Manuel, D. Khalyavin and S. J. Clarke. *J. Am. Chem. Soc.* **136**, 630–633 (2014). 82, 104, 107

[120] A. A. Coelho. *TOPAS Academic: General Profile and Structure Analysis Software for Powder Diffraction Data, V5* (2010). 86

[121] J. C. Burley, P. D. Battle, D. J. Gallon, J. Sloan, C. P. Grey and M. J. Rosseinsky. *J. Am. Chem. Soc.* **124**, 620–628 (2002). 87

[122] S. Ghannadzadeh, J. D. Wright, F. R. Foronda, S. J. Blundell, S. J. Clarke and P. A. Goddard. *Phys. Rev. B* **89**, 054502 (2014). 92

[123] V. Fesenko, V. Gorbunov and V. Smilga. *Physica C: Superconductivity* **176**, 551 – 558 (1991). 95

[124] F. Hunte, J. Jaroszynski, A. Gurevich, D. Larbalestier, R. Jin, A. Sefat, M. A. McGuire, B. C. Sales, D. K. Christen and D. Mandrus. *Nature* **453**, 903–905 (2008). 98

[125] M. Kano, Y. Kohama, D. Graf, F. Balakirev, A. S. Sefat, M. A. Mcguire, B. C. Sales, D. Mandrus and S. W. Tozer. *J. Phys. Soc. Jpn* **78**, 084719 (2009). 98

[126] N. R. Werthamer, E. Helfand and P. C. Hohenberg. *Phys. Rev.* **147**, 295–302 (1966). 98

[127] A. Gurevich. *Physica C: Superconductivity* **456**, 160 – 169 (2007). 99

[128] A. Gurevich. *Phys. Rev. B* **67**, 184515 (2003). 99, 101

[129] Y. J. Uemura, G. M. Luke, B. J. Sternlieb, J. H. Brewer, J. F. Carolan *et al.* *Phys. Rev. Lett.* **62**, 2317–2320 (1989). 101, 112

[130] Y. J. Uemura, L. P. Le, G. M. Luke, B. J. Sternlieb, W. D. Wu, J. H. Brewer, T. M. Riseman, C. L. Seaman, M. B. Maple, M. Ishikawa, D. G. Hinks, J. D. Jorgensen, G. Saito and H. Yamochi. *Phys. Rev. Lett.* **66**, 2665–2668 (1991). 101, 112

[131] C. Niedermayer, C. Bernhard, U. Binninger, H. Glückler, J. L. Tallon, E. J. Ansaldo and J. I. Budnick. *Phys. Rev. Lett.* **71**, 1764–1767 (1993). 101

[132] J. L. Tallon, J. W. Loram, J. R. Cooper, C. Panagopoulos and C. Bernhard. *Phys. Rev. B* **68**, 180501 (2003). 101

[133] C. Homes, S. Dordevic, M. Strongin, D. Bonn, R. Liang, W. Hardy, S. Komiya, Y. Ando, G. Yu, N. Kaneko *et al.* *Nature* **430**, 539–541 (2004). 101

[134] F. L. Pratt and S. J. Blundell. *Phys. Rev. Lett.* **94**, 097006 (2005). 101

[135] J. L. Tallon, J. R. Cooper, S. H. Naqib and J. W. Loram. *Phys. Rev. B* **73**, 180504 (2006). 101

[136] B. J. Taylor and M. B. Maple. *Phys. Rev. B* **76**, 184512 (2007). 101

[137] E. H. Brandt. *Phys. Rev. B* **37**, 2349–2352 (1988). 102

[138] C. C. Homes, B. P. Clayman, J. L. Peng and R. L. Greene. *Phys. Rev. B* **56**, 5525–5534 (1997). 102

[139] A. Shengelaya, R. Khasanov, D. G. Eshchenko, D. Di Castro, I. M. Savić, M. S. Park, K. H. Kim, S.-I. Lee, K. A. Müller and H. Keller. *Phys. Rev. Lett.* **94**, 127001 (2005). 102

[140] F. L. Pratt, P. J. Baker, S. J. Blundell, T. Lancaster, H. J. Lewtas, P. Adamson, M. J. Pitcher, D. R. Parker and S. J. Clarke. *Phys. Rev. B* **79**, 052508 (2009). 102, 112, 115, 119

[141] M. J. Pitcher, T. Lancaster, J. D. Wright, I. Franke, A. J. Steele, P. J. Baker, F. L. Pratt, W. T. Thomas, D. R. Parker, S. J. Blundell and S. J. Clarke. *J. Am. Chem. Soc.* **132**, 10467–10476 (2010). 102, 115

[142] F. F. Foronda, D. N. Woodruff, F. Lang, S. J. Cassidy, T. Lancaster, P. J. Baker, F. L. Pratt, S. J. Clarke and S. J. Blundell Submited to Phys. Rev. B. 103

[143] M. Abdel-Hafiez, J. Ge, A. N. Vasiliev, D. A. Chareev, J. Van de Vondel, V. V. Moshchalkov and A. V. Silhanek. *Phys. Rev. B* **88**, 174512 (2013). 105

[144] Y.-Y. Hsu, Y.-B. Li, S.-T. Jian, G.-K. Li and M.-C. Yang. *Superconductor Science and Technology* **29**, 035005 (2016). 105

[145] E. H. Brandt. *Phys. Rev. B* **68**, 054506 (2003). 107

[146] H. Lei, D. Graf, R. Hu, H. Ryu, E. S. Choi, S. W. Tozer and C. Petrovic. *Phys. Rev. B* **85**, 094515 (2012). 107

[147] H. Lei, R. Hu and C. Petrovic. *Phys. Rev. B* **84**, 014520 (2011). 107

[148] Y. Sakai, L. Zheng, M. Izumi, K. Teranishi, R. Eguchi, H. Goto, T. Onji, S. Araki, T. C. Kobayashi and Y. Kubozono. *Phys. Rev. B* **89**, 144509 (2014). 107

[149] A. Sidorenko, V. Smilga and V. Fesenko. *Physica C: Superconductivity* **166**, 167 – 176 (1990). 109, 118

[150] S. L. Thiemann, Z. Radović and V. G. Kogan. *Phys. Rev. B* **39**, 11406–11412 (1989). 109

[151] H. Luetkens, H.-H. Klauss, R. Khasanov, A. Amato, R. Klingeler, I. Hellmann, N. Leps, A. Kondrat, C. Hess, A. Köhler, G. Behr, J. Werner and B. Büchner. *Phys. Rev. Lett.* **101**, 097009 (2008). 112, 113

[152] A. J. Drew, F. L. Pratt, T. Lancaster, S. J. Blundell, P. J. Baker, R. H. Liu, G. Wu, X. H. Chen, I. Watanabe, V. K. Malik, A. Dubroka, K. W. Kim, M. Rössle and C. Bernhard. *Phys. Rev. Lett.* **101**, 097010 (2008). 112, 113

[153] R. Khasanov, H. Luetkens, A. Amato, H.-H. Klauss, Z.-A. Ren, J. Yang, W. Lu and Z.-X. Zhao. *Phys. Rev. B* **78**, 092506 (2008). 112, 113

[154] J. P. Carlo, Y. J. Uemura, T. Goko, G. J. MacDougall, J. A. Rodriguez *et al.* *Phys. Rev. Lett.* **102**, 087001 (2009). 112, 113

[155] D. R. Parker, M. J. P. Smith, T. Lancaster, A. J. Steele, I. Franke, P. J. Baker, F. L. Pratt, M. J. Pitcher, S. J. Blundell and S. J. Clarke. *Phys. Rev. Lett.* **104**, 057007 (2010). 112, 113

[156] P. J. Baker, T. Lancaster, S. J. Blundell, F. L. Pratt, M. L. Brooks and S.-J. Kwon. *Phys. Rev. Lett.* **102**, 087002 (2009). 112

[157] F. Hayashi, H. Lei, J. Guo and H. Hosono. *Inorganic Chemistry* **54**, 3346–3351 (2015). 112

[158] A. Amato, R. Khasanov, H. Luetkens and H.-H. Klauss. *Physica C: Superconductivity* **469**, 606 – 613 (2009). Superconductivity in Iron-Pnictides. 113

[159] Z. Shermadini, H. Luetkens, R. Khasanov, A. Krzton-Maziopa, K. Conder, E. Pomjakushina, H.-H. Klauss and A. Amato. *Phys. Rev. B* **85**, 100501 (2012). 113

[160] P. K. Biswas, A. Krzton-Maziopa, R. Khasanov, H. Luetkens, E. Pomjakushina, K. Conder and A. Amato. *Phys. Rev. Lett.* **110**, 137003 (2013). 113

[161] Z. Deng, X. C. Wang, Q. Q. Liu, S. J. Zhang, Y. X. Lv, J. L. Zhu, R. C. Yu and C. Q. Jin. *EPL (Europhysics Letters)* **87**, 37004 (2009). 114

[162] D. R. Parker, M. J. Pitcher, P. J. Baker, I. Franke, T. Lancaster, S. J. Blundell and S. J. Clarke. *Chem. Commun.* 2189–2191 (2009). 114

[163] J. H. Tapp, Z. Tang, B. Lv, K. Sasmal, B. Lorenz, P. C. W. Chu and A. M. Guloy. *Phys. Rev. B* **78**, 060505 (2008). 114

[164] S. Kasahara, K. Hashimoto, H. Ikeda, T. Terashima, Y. Matsuda and T. Shibauchi. *Phys. Rev. B* **85**, 060503 (2012). 115

[165] H. Kim, M. A. Tanatar, Y. J. Song, Y. S. Kwon and R. Prozorov. *Phys. Rev. B* **83**, 100502 (2011). 115

[166] J. S. Kim, L. Y. Xing, X. C. Wang, C. Q. Jin and G. R. Stewart. *Phys. Rev. B* **87**, 054504 (2013). 115

[167] K. Hashimoto, S. Kasahara, R. Katsumata, Y. Mizukami, M. Yamashita, H. Ikeda, T. Terashima, A. Carrington, Y. Matsuda and T. Shibauchi. *Phys. Rev. Lett.* **108**, 047003 (2012). 115, 117, 118, 119, 122

[168] J. D. Wright, M. J. Pitcher, W. Trevelyan-Thomas, T. Lancaster, P. J. Baker, F. L. Pratt, S. J. Clarke and S. J. Blundell. *Phys. Rev. B* **88**, 060401 (2013). 115

[169] G. Luke, Y. Fudamoto, K. Kojima, M. Larkin, J. Merrin, B. Nachumi, Y. Uemura, Y. Maeno, Z. Mao, Y. Mori *et al. Nature* **394**, 558–561 (1998). 115

[170] A. D. Hillier, J. Quintanilla and R. Cywinski. *Phys. Rev. Lett.* **102**, 117007 (2009). 115